This thesis is lovely dedicated to my wife, Rosa Elisa, for her love and unconditional support during the past 10 years, and especially during the time of this Ph.D. For remind me over and over again that I should follow my dreams.

Acknowledgments

The time that I spend during the Ph.D has been, without a doubt, the most amazing time so far. This manuscript is the result of more than three and a half years of hard work, but the people that I met during this time did it very gratifying. I would like to take this opportunity to thank all of the people who helped me to make this thesis possible.

First I would like to thank to Dr. Jean-Yves Raty for his great supervision. By give me the opportunity to join to his research group, for his patience and great effort to explain things in a clear and simple way. I also want to thank you for encouraging and support my travels to show my work to the scientific community. Overall, thank you for show me, with your example, the values and ethic that a researcher should always have.

I would also like to thank Prof. Matthieu Verstraete for all his help on the computational resources and the interesting and intense discussions on a wide variety of subjects. Thank you also for your the scientific collaboration during my master and my Ph.D, and also thanks for allow me to join the scientific group of the University of Liege in first place five years ago. Without a doubt, I will be always in debt with you.

Especial thanks also for Dra. Zeila Zanolli and Dr. Baris Malcioglu that always make me feel welcome in their homes (Baris even opened us the door of his apartment, to me and mi wife, the first week we meet). I must say that I enjoyed all the times that we share a dinner or a beer, and I cannot thank enough for all your advice that not always were related to science.

Thanks to all my colleagues that are, or were, at the department of physics at the university of Liege, for their friendship and to make the all those intense working days more enjoyable: Julien, Hania, Henu, Begum, Denis, Safari, Srijan, Gabrielle, Felipe, Naihua, Momar, Marco, Theodoros, Nicholas, Jordan, Can, Andres Camilo, Eric, Philippe, Fozi, Jinzhu, Micael, Hanen,

Bin, Misha, Henrique, Sebastian, Alain, Antoine, Brahim, Fabio.

I would like to thank my parents, Wilfredo and Dolores, for teach me that anything is reachable with consistency and hard work. Thanks to my brother and sister, Carlos Eduardo and Andrea Alejandra, that even being thousands of kilometers away they are always there for me. I thank my friends in Mexico (US and Colombia) by keeping in touch (some of them even took the opportunity and they came to visit us) and by sending us their best wishes: Irais, Christian, Jael, Andres Camilo, Camilo Andres, Livier, Yafid, Iris, Miguel, Arely, Dirceu, Daniela, Alma, Karla, Paty.

Contents

List of Figures

List of Tables

Résumé

Dans cette thèse, nous explorons les propriétés électroniques, dynamiques et thermoélectriques de différents composés à base de tellure. Nous utilisons pour ce faire une méthode ab initio telle quimplémentée dans le code Vienne Ab-initio Simulation Package (VASP) qui fonctionne dans le cadre de la théorie de la fonctionnelle de la densité (DFT). Pour les propriétés thermoélectriques, nous utilisons le code Boltztrap qui résout les équations de transport de Boltzmann (BTE) pour les électrons dans l'approximation du temps de relaxation constant (CRTA). Ce package nous permet d'obtenir des valeurs précises du coefficient Seebeck en fonction de la température et de la concentration des porteurs de charge. Enfin, pour calculer la contribution du réseau à la conductivité thermique, nous utilisons le code ShengBTE qui résout le contour l'équation de transport de Boltzmann pour les phonons de manière itérative.

Le premier composé à base de tellure que nous étudions est le meilleur matériau thermoélectrique à température ambiante connu à l'heure actuelle, le $Bi_2 Te_3$. Nous obtenons des résultats comparables avec les données expérimentales pour le coefficient de Seebeck à température et pression ambiantes. Par la suite, nous décrivons les propriétés électroniques et la performance thermoélectrique du composé jusqu'à une pression de 5 GPa. Nous reproduisons la tendance globale du coefficient de Seebeck en fonction de la pression pour deux valeurs différentes du dopage, cependant nos résultats ne reproduisent pas la petite amélioration constatée dans les expériences à 1 GPa. Néanmoins, nous confirmons la découverte expérimentale d'une transition électronique topologique (ETT) aux environs de 2 GPa et en expliquons le mécanisme.

Nous présentons ensuite des calculs sur les matériaux à changement de phase à base de tellure de composition $(GeTe)_x(Sb_2Te_3)_1$ (avec x = 1, 2, 3). Nous décrivons en détail les propriétés de différents types d'empilements de plans d'atomes étant donné que la position exacte des atomes dans la maille est toujours incertaine à l'heure actuelle. Nous établissons que ces matériaux

peuvent être semiconducteurs ou métalliques selon le type d'empilement. Les structures semiconductrices surestiment systématiquement le coefficient de Seebeck alors que les empilements métalliques reproduisent les données expérimentales pour le coefficient de Seebeck et la contribution des phonons à la conductivité thermique. Dans ces composés, le facteur de mérite thermoélectrique ZT peut atteindre un maximum de 0.5 à 600K lorsque le dopage est optimisé. Dans le cas de $(GeTe)_3(Sb_2Te_3)_1$, le type d'empilement proposé dans la littérature est instable et nous proposons une structure alternative. Enfin, nous discutons la différence entre nos calculs et les travaux théoriques publiés par ailleurs et qui mentionnent l'existence d'un cone de Dirac dans la structure électronique de $(GeTe)_2(Sb_2Te_3)_1$. Nous expliquons pourquoi ceci n'est en réalité vérifié que sous certaines conditions de contrainte et avec certaines approximations de l'échange-corrélation.

Abstract

In this thesis, we explore the electronic, dynamic and thermoelectric properties of different tellurium-based compounds. We perform ab-initio calculations within the Vienna Ab-initio Simulation Package (VASP) that works in the framework of Density Functional Theory (DFT). For the thermoelectric properties, we use the Boltztrap code that solves the Boltzmann Transport Equations (BTE) for electrons within the Constant Relaxation Time Approximation (CRTA). This computational package allows us to obtain accurate values of the Seebeck coefficient as a function of temperature and carrier concentration (this last with the help of the rigid band approximation). While for the calculation of the lattice contribution to the thermal conductivity, we use the ShengBTE code that solves the BTE for phonons iteratively.

The first tellurium-based compound that we study is the best room temperature thermoelectric material, Bi_2Te_3. We obtain results comparable with experimental data for the Seebeck coefficient at room temperature and pressure. Afterwards, we proceed to explore the evolution of the electronic properties and the thermoelectric performance under pressures up to 5 GPa. We reproduce the overall trend of the Seebeck coefficient as a function of pressure for two different values of doping, however, our results do not reproduce the small improvement found in experiments close to 1 GPa. Nevertheless, we support the experimental evidence of an Electronic Topological Transition (ETT) around 2 GPa and we explain this particular behavior.

We also perform calculations on the tellurium-based phase-change materials $(GeTe)_x(Sb_2Te_3)_1$ (with x = 1, 2, 3). We show results for different stacking configurations since for some compositions, the stacking arrangement of the atoms in the primitive cell is still unsettled. We find that the change of the atomic arrangement leads to the systems to go from semiconductors to metals. We find that the semiconductor arrangements systematically overestimate the experimental values for the Seebeck coefficient, whereas the metallic stacking sequences are in very good agreement with the

experimental data for the Seebeck coefficient and for the lattice contribution to the thermal conductivity. We show that $(GeTe)_x(Sb_2Te_3)_1$ materials could reach values of ZT=0.5 around 600 K with a proper optimization of S with respect to the carrier concentration. We also report that in the case of x=3, the most accepted stacking configuration is dynamically unstable, therefore we proposed another sequence. Finally, we discuss the discrepancies between our work and recent theoretical reports that claim the existence of a Dirac-cone like band structure for $(GeTe)_2(Sb_2Te_3)_1$. We explain the conditions necessary to obtain such electronic topology.

Introduction

In a world with an increasing demand of electricity and with serious environmental problems caused by the combustion of fossil fuels, it is really important to find new green sources to produce electricity. Indeed, many research activities have been devoted to this quest. On the other hand, it is striking to note that, according to the International Energy Agency (IEA), about one third of the total electricity produced worldwide is actually wasted during transportation, as well as in devices, due to the Joule effect. This resistive heating of the electrical wires can only be suppressed by using superconductor materials, which are presently limited to very low temperatures and specific niche applications, such as giant electromagnets.

Another approach is to try to recover the wasted electricity by converting the produced heat back in electricity. This is achievable and the effect is called thermoelectricity, the phenomenon of direct transformation of a gradient of temperature into electricity and vice versa. It is not limited to Joule heat recovery, but can be used to convert any temperature gradient in electricity.

Despite the potential of the thermoelectric effect, one can notice that the research in this direction has been totally overshadowed by the research for new energy sources. For over 30 years tremendous effort was made to increase the efficiency of thermoelectric devices. However, only small improvement has been achieved since bismuth telluride, first studied for thermoelectric applications in 1986 [1], and remains as state-of-art bulk material at room temperature.

Nevertheless, the efficiency for energy conversion of this compound is limited to 12 % in its bulk form, which is still insufficient for a wide industrial application. It is usually accepted that 25 % efficiency is the lower limit for a thermoelectric material [2]. At present, thermoelectric materials (Bi_2Te_3, Sb_2Te_3) are often limited to low temperature operation. For instance these

are commonly used in satellite's components [3, 4]. Another industry that is investing in thermoelectrics as a source to recover wasted heat is the automotive industry. A typical gasoline-fueled engine has efficiencies of around 25 %, while the remained is lost in form of waste heat. The average temperature differences in the vehicle exhaust are around 300 K, with the hot side at temperatures as high as 700 K. Therefore, a different kind of materials is needed for this application with a decent thermoelectric performance at high T.

The research for efficient thermoelectric materials has undergone some regain in activity since the beginning of the 21st century [5]. In particular, groups have been improving the materials performance by changing the overall geometry, rather than trying to find better chemical composition. Multilayers, nanoscale inclusions, skutterudites, clathrates and ceramic oxides, domain engineering are some of the new directions that have been investigated.

In this thesis, we will address the problem from a different viewpoint, starting from the observation that the outstanding thermoelectric properties of bismuth (but also antimony) telluride are thought to be originating from its layered structure and from strong spin-orbit interaction. Independently, tellurium-based compounds have been extensively studied in the last decades as some of them (mostly in the ternary Ge-Sb-Te diagram) exhibit the so called phase change properties [6]. These phase-change materials (PCMs) could be good thermoelectric alternatives since, as well as bismuth telluride (and Sb_2Te_3), PCMs are based on tellurium, possess a layered nature and have strong spin-orbit interaction with a larger bandgap than Bi_2Te_3.

Therefore, this thesis is devoted to the investigation of the thermoelectric properties of these materials. We will quantify the effect of layering (constructing various $(GeTe)_x(Sb_2Te_3)_1$ structures) on the electronic and phonon transport properties, but first we will describe in details the effect of modifying the interlayer separation - and bonding - in the prototype Bi_2Te_3 material. An easy way to do this is by applying high pressure.

The method of choice to study the electronic properties of solids, in general, is Density Functional Theory. In the present work, we use the Vienna Ab-initio Simulation Package (VASP) [7, 8, 9]. With the help of other codes that solve the Boltzmann transport equation for electrons within the constant relaxation time approximation, such the BOLTZTRAP code [10], it is possible to obtain a very important thermoelectric property, the Seebeck

coefficient. We then use the finite differences together with the real-space supercell approach to obtain the phonon dynamics of the system. Finally, we perform calculations that allow us to compute another key property for thermoelectric applications, namely the lattice contribution to the thermal conductivity, by using the ShengBTE code [11].

This manuscript is organized as follows:

In Chapter 1, we will describe the concept of thermoelectricity. We will explain the theory behind the thermoelectric phenomena and introduce the various quantities that will be useful for the following chapters: the Seebeck coefficient, the thermal and electrical conductivity and their implications in the thermoelectric performance.

In Chapter 2, we will give a brief account for Density Functional Theory (DFT). We will discuss the Born-Oppenheimer approximation, the concept of the exchange and correlation energy as well as pseudopotentials.

In Chapter 3 we will introduce the Boltzmann transport equations and the constant relaxation time approximation, as well as its implementation in the computation package. We will briefly discuss the Boltzmann transport equation for phonon and its implementation in the ShengBTE code.

In Chapter 4 we will start with the computational details for our calculations in Bi_2Te_3 as well as for $(GeTe)_x(Sb_2Te_3)_1$ compounds. Then, we will present our results concerning the evolution of the Seebeck coefficient, and the electronic properties in bismuth telluride as a function of the hydrostatic pressure. We will discuss in details the relation with the experimental data, and give a special focus on the reported Electronic Topology Transition.

Finally, Chapter 5 will contain our results for quasi-binary phase-change materials $(GeTe)_x(Sb_2Te_3)_1$. We will describe the structure, electronic and phonon properties and explore the thermoelectric behavior of materials with x=1, 2 and 3.

Chapter 1

Thermoelectricity

Our modern lifestyle depends on electricity. Nowadays we carry devices that never should be turned off. In our houses the WiFi modem, as the refrigerator, is always on. In the office, we work with computers than remain working even when we are not there. Factories use machines to create more machines or electronic equipment. Modern society could not be described without electricity. On the other side, the energy production to fulfill the growing demand due to the increase of the global population, comes with a high economic and environmental cost. According to the International Energy Agency (IEA), two-thirds of the total greenhouse emission gases come from the energy generation. The environmental impact of the combustion of fossil fuels is reaching alarming levels. Even though, in 2013 the oil market as global energy source fell; it is still the dominant source of energy in the world. The oil and coal represent 63 % of the total energy source, while renewable energies represent just 2 % [12]. Strikingly, more than two-thirds of the energy generated by burning fossil fuels are lost as waste heat. One immediately realizes that recovering some of that waste heat to regenerate electricity could, eventually, reduce the dependency on fossil fuels. This can be achieved using a thermoelectric device, which works with a gradient of temperature and captures the transported heat to convert it into electricity. The opposite effect is also possible, a current that passes through a thermoelectric refrigerator will produce a temperature difference.

Nowadays, the low efficiency is the biggest drawback of thermoelectric devices, which only reach 30 % of the Carnot efficiency when these are working between reservoirs of 300 K and 900 K. It is usually accepted that in order to compete with modern refrigerators or energy generators, the thermoelectric efficiency should increase by a factor of three. The improvement of ther-

moelectric efficiency could lead to the recovery of lost energy from sources that are, nowadays, neglected. A bonfire could become a cell phone charger. The exhaust of automotive engines, or even the heat generated by friction in the breaks, will be captured and converted into electricity, which would increase the efficiency of hybrid cars. Nevertheless, there is still a lot of work to be done in research to achieve thermoelectric efficiencies that compete with current energy generators or refrigerators. In this chapter, we provide basic concepts of thermoelectrics with a special focus set on the limitation and challenges of thermoelectric devices.

1.1   The Thermoelectric Effect

The thermoelectric phenomenon was first observed by Thomas Johann Seebeck in 1821. He showed that a voltage could be generated by heating a junction of two different metals (thermocouple). By heating the junction, electrons and holes travel in opposite directions creating a voltage difference. The generated voltage is proportional to the temperature difference ($V = S\Delta T$), where the proportionality constant is known as the Seebeck coefficient (S). In 1834, Jean Charles Athanase Peltier showed the reverse effect. He realized that when a current passes through a thermocouple, a certain amount of heat could be generated or removed depending on the direction of the current. A current passing through the junction moves the carriers and also the heat. The direction of the current determines if the junction is cooled or heated. The Peltier coefficient corresponds to the ratio between the extracted or generated heat by the electrical current ($\Pi = Q/I$, where Π is the Peltier coefficient, Q is the heat and I is the current). The fact that the Seebeck and Peltier effects occur just in the thermocouple (the junction of two different metals at that time) suggest that the mentioned effects are, somehow, related to the interface but, in fact, they are related to the bulk properties of the materials involved.

Today we know that electrons are responsible for the electrical current in the materials. By heating a material in a temperature gradient, we provide energy to electrons which allows them to travel from the hot side to the cold side. This constant migration of electrons induces a difference in voltage. When the generated electric field is strong enough, the movement of electrons will cease. It was not until 21 years after Peltier's discovery that William Thomson (the later Lord Kelvin) identified the relation between the Peltier and Seebeck effects. He established that the Peltier and Seebeck effects are connected by thermodynamics. In addition, he determined that the Peltier's
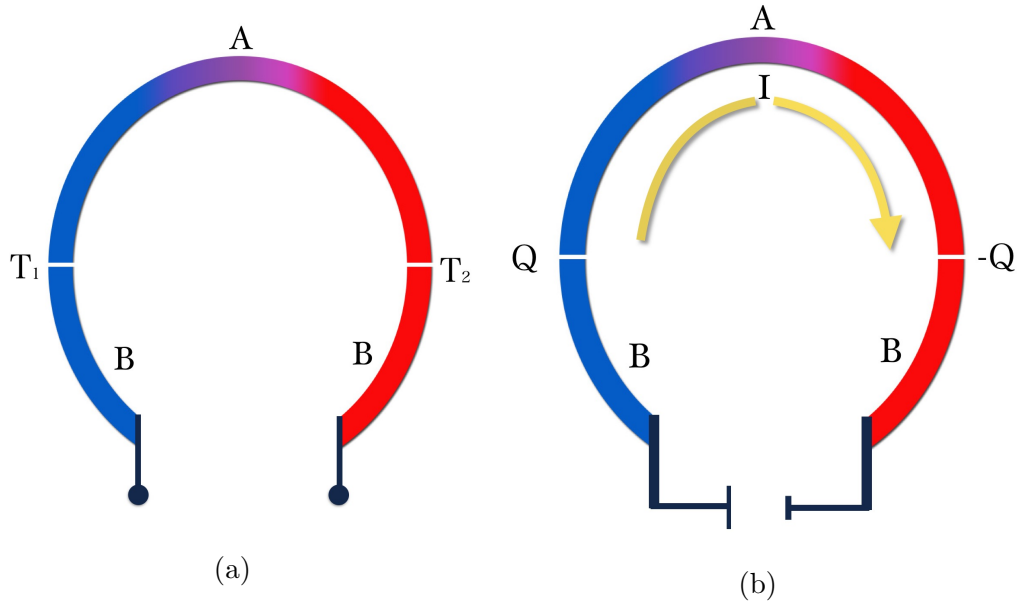
Figure 1.1: **(a)** Schematic representation of a power generator thermocouple. A and B are two different metals, where the junctions are at different temperatures T_1 and T_2. The gradient in temperature produces a voltage difference between the free ends of material B. **(b)** Schematic representation of a thermoelectric refrigerator thermocouple. A current I passes through materials A and B causing the absorption and release of heat Q. (Figure adapted from [13])

coefficient is the Seebeck's coefficient multiplied by the absolute temperature ($\Pi = ST$). He also predicted another thermoelectric effect that must occur in a homogeneous material: the so-called Thomson effect occurs in a single material exposed to a difference in voltage and a gradient of temperature. In the Thomson effect, heat is absorbed or produced in a material when a current flows through it with a gradient of temperature. The heat is proportional to the electrical current and to the gradient in temperature. The proportionality constant is the so-called Thomson coefficient ($dQ/dt = -\xi J \Delta T$, here dQ, dt and ΔT are the gradient of heat, time and temperature, respectively; J is the current density and finally ξ is the Thomson coefficient) [13].

Now, we will focus on the relation between Seebeck and Peltier effects. We will consider the thermocouple in figure 1.1a. The material B is split in two parts, both of which having a free end while the other end joins the material A. A voltmeter can be connected between the two free ends of the material B. By heating the material A, it is possible to create a gradient of temperature between the two junctions. With this, we can calculate the

differential Seebeck coefficient of the thermocouple:

$$S_{AB} = \frac{V}{(T_{hot} - T_{cold})} = \frac{V}{\Delta T}. \tag{1.1}$$

S_{AB} can be either positive or negative depending of the direction of the flow of carriers. In the previous case, if the generated voltage induces the electrical current to travel from the hot side to the cold side, then the Seebeck coefficient will be positive, and negative otherwise. Similarly, we can define the Peltier coefficient (figure 1.1b). Instead of heating the material A, we induce a current between the two free ends of the material B, this will produce an electric current flowing through the thermocouple. Assuming that the direction of the current is clockwise, the Peltier coefficient will be positive if the junction where the current enters the material A heats up, and the junction where the current leave the material A gets cooler. As we mentioned, the emitted or extracted heat is proportional to the current that flow through the junctions, and the proportionality constant is the Peltier coefficient.

According to Goldsmid [13], the Seebeck coefficient can be easily measured and thanks to one of the Kelvin relations, it is possible express the Peltier coefficient as a function of the Seebeck coefficient:

$$\Pi_{AB} = S_{AB}T. \tag{1.2}$$

The coefficients described in equation 1.2 correspond to differential coefficients; this means the coefficient of the thermocouple and not that of a single material. The absolute Seebeck coefficient can be determined if one of the materials in the thermocouple has zero S. According with Prof. David Emin, the Seebeck coefficient measures the entropy transported by a charge while it moves, divided by the carriers charge [14]. With this concept of the Seebeck coefficient, one can understand that the use of superconductors as the second material allows to measure absolute values of S for the first material. It is reasonable to assign zero absolute Seebeck coefficients to superconductors since the differential Seebeck coefficient of any pair of superconductors is zero. Nevertheless, there is not a material that remains in the superconductor state at room temperature or beyond. For this reason, S can be only be measured at low T.

The Seebeck coefficient, as we mentioned, is material dependent property that varies with temperature. The relation between the Seebeck and the Thomson coefficients allows to calculate the Seebeck coefficient at high temperatures. For a single material, the Kelvin relation between the Thomson
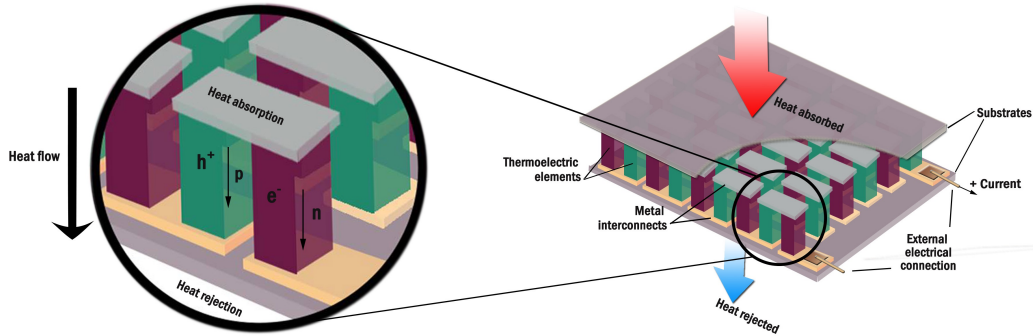
Figure 1.2: Thermoelectric device showing how the thermocouples are wired electrically in series and thermally in parallel. (Figure adapted from [5])

and Seebeck coefficients is:

$$\xi = T\frac{dS}{dT}. \tag{1.3}$$

The absolute Seebeck coefficient of a specific material can be measured at low T by making a thermocouple between this material and a superconductor. Afterwards, it is possible to use the Kelvin relation to determine the values of S at high temperature through the measure of the Thomson coefficient. This method has been used to determine the Seebeck coefficient for different metals such as lead. We mention lead because this material can be used as a reference for the determination of S for other materials. Most metals, like lead, exhibit small values of the Seebeck coefficient ($S_{Pb} = -0.8\mu V/K$) compared with good thermoelectric materials that are, invariably, narrow bandgap semiconductors such as Bi$_2$Te$_3$ ($S_{Bi_2Te_3} = 200\mu V/K$).

1.2 Thermoelectric efficiency

In 1911 Edmund Altenkirch analyzed the low efficiency problem of thermocouples. He realized that the thermoelectric efficiency was directly proportional to the Seebeck coefficient and to the electrical conductivity. On the other hand, he realized that the thermal conductivity was inversely proportional to the improvement of efficiency. According to Altenkirch observations, a high Seebeck coefficient necessitates a moderate gradient of temperature to

obtain a significant difference in voltage (see equation 1.1). Smaller values of thermal conductivity allow to preserve ΔT since the heat is not easily transported through the material and, therefore, the thermoelectric performance increases. Large values of electrical conductivity, prevent the generation of Joule heat, which helps to keep a large temperature difference. The Joules heat is provoked by the collision of moving carriers with the "static" ions [13].

If we test different materials with the same volume, we will find differences in the obtained current if we apply a voltage, and heat if we applied a gradient of temperature. The current (I) that flows through a material with length L and transversal area A when a voltage difference V is applied can be determined by the electrical conductivity (σ) of such material:

$$I = \frac{\sigma V A}{L}, \tag{1.4}$$

similarly, the amount of heat Q that travels through a material depends on the thermal conductivity (κ) and on the temperature gradient (ΔT):

$$Q = -\frac{\kappa A \Delta T}{L}. \tag{1.5}$$

As shown in equations (1.4) and (1.5), both thermal and electrical conductivities are material dependent and, as well as the Seebeck coefficient, are intrinsic properties that vary with temperature. The work of Altenkirch laid the foundation of what we now know as the thermoelectric figure of merit (ZT). The performance of a thermoelectric material is measured by ZT which is defined as:

$$ZT = \frac{S^2 \sigma}{\kappa} T. \tag{1.6}$$

The larger the value of ZT, the larger the efficiency of a thermoelectric material. Although all practical thermoelectric devices consist of many thermocouples connected thermally in parallel and electrically in series (see figure 1.2), it is sufficient to consider the behavior of one thermocouple. For a given thermoelectric device the efficiency (η) is given by the equation:

$$\eta = \frac{\Delta T}{T_H} \frac{\sqrt{1 + ZT} - 1}{\sqrt{1 + ZT} + \frac{T_C}{T_H}}. \tag{1.7}$$

The previous equation is given in the form of the Carnot efficiency multiplied by the figure of merit ($T = (T_H + T_C)/2$ in ZT) [5]. In order to increase the thermoelectric efficiency, the thermoelectric figure of merit of constituting materials should be as large as possible. In equation (1.7), if ZT is large
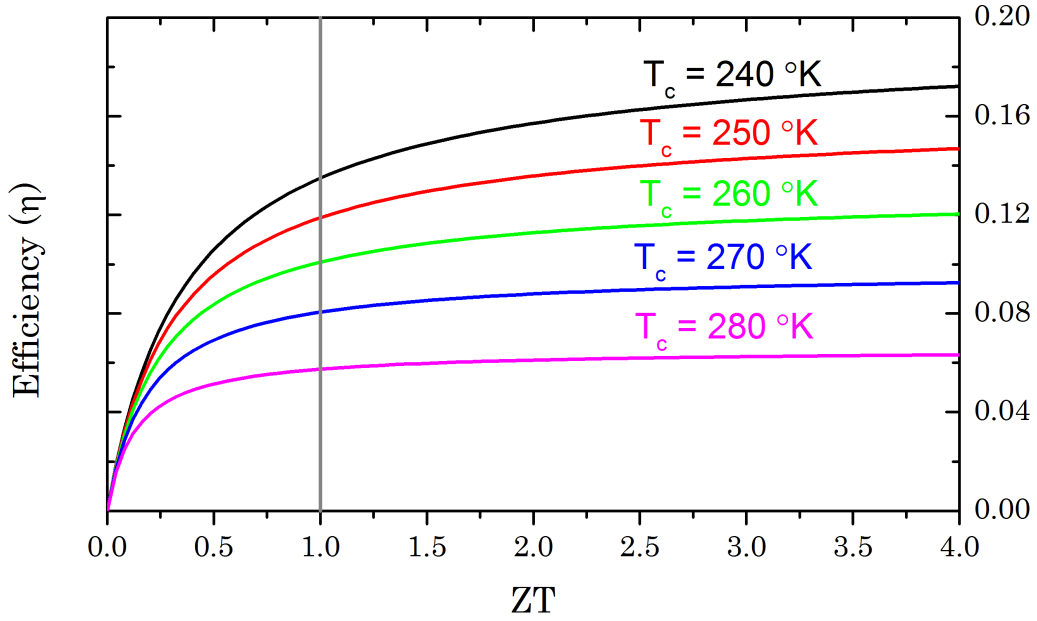
Figure 1.3: Efficiency of a thermoelectric device as function of the thermoelectric figure of merit, at different values of temperature for the cold side of the device. The plot refers to equation (1.7) with $T_H = 300°K$.

enough, $\eta \approx \Delta T/T_H$ which is the efficiency of an ideal thermodynamic machine also called Carnot efficiency. It has been claimed that in order to compete with modern energy generators or conventional refrigerators, ZT values should be as large as 3 or 4. Even though, thermodynamically there is no upper limit of the figure of merit, the values are presently far from optimal [15].

As we mentioned, the Seebeck coefficient of the materials should be large so that the smallest gradient in temperature will lead to a large difference in voltage. The adjective large is relative; due to the small values of S, it is usual to express the Seebeck coefficient in units of $\mu V/K$. The electrical conductivity should be also large to reduce losses due to Joules heating. If the electrical resistance is large ($\rho = 1/\sigma$), larger will be the self-heating of the material. On the contrary, the thermal conductivity should be small to maintain the temperature gradient and reduce the heat leaking. The strong link between the Seebeck coefficient and electrical conductivity illustrates the complex task which is the enhancement of the thermoelectric performance.
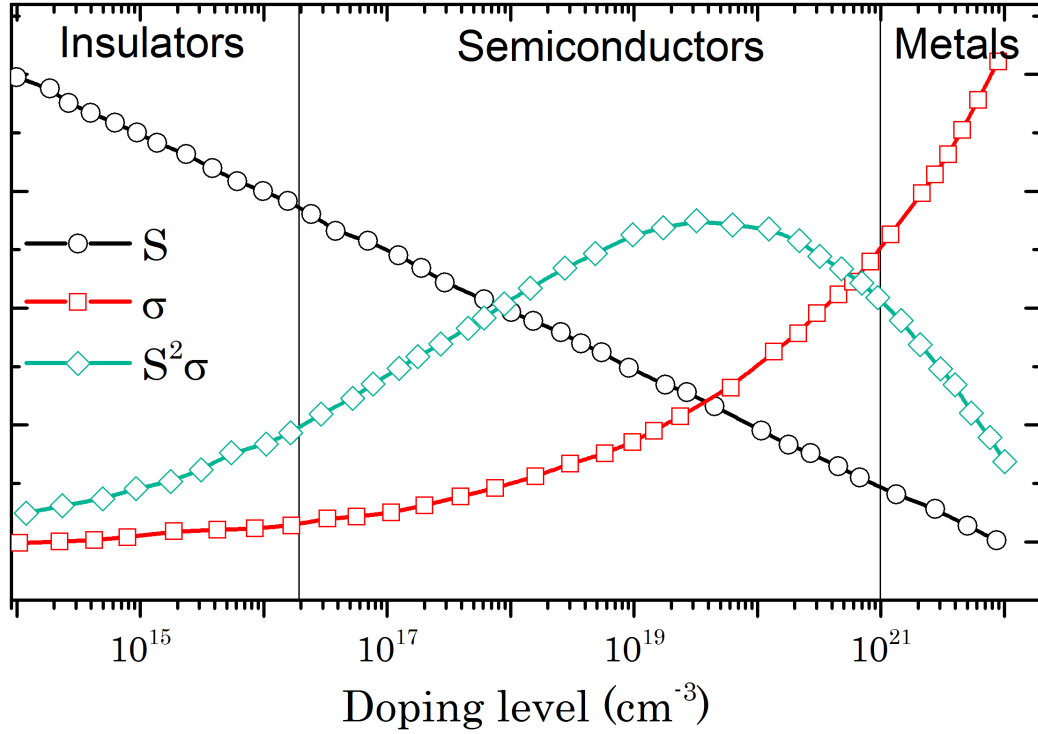
Figure 1.4: Schematic representation of the Seebeck coefficient (S), electrical conductivity (σ) and power factor ($S^2\sigma$) as a function of the carrier concentration. (Figure adapted from [5])

1.3 Thermoelectric materials

Even though the properties in equation (1.7) have been well studied for many existing materials, it is still difficult to improve the thermoelectric efficiency. To choose the best possible thermoelectric material, we can start by classifying the compounds into one of the following groups: metals, insulators and semiconductors. In chapter 3, will explain the theory of transport, but here we just focus on some generalities to understand the selection of thermoelectric materials.

1.3.1 Metals and insulators

As we mentioned, metals were the first choice as possible thermoelectric materials [13]. Metals have high electron mobility (μ) and, therefore, high electrical conductivity ($\sigma = ne\mu$ where e is the electronic charge). Nevertheless, the electric and thermal conductivity ratio in metals is a constant. This means that any increase in the electrical conductivity invariably leads

to an increase of the thermal conductivity. This is given by the Wiedemann-Franz law: $\kappa_e = LT\sigma$. Where κ_e is the electronic contribution to the thermal conductivity ($\kappa = \kappa_e + \kappa_l$, κ_l being the lattice contribution to the total thermal conductivity) and L is the Lorentz number that for metals is: $L \approx \frac{\pi^2}{3}(\frac{k_B}{e})^2 = 2.44 \times 10^{-8}\frac{W\Omega}{K^2}$. The Wiedemann-Franz law works well for both metals and highly doped semiconductors close to room temperatures. As we pointed out, most of the present thermoelectric materials are semiconductors, not metals. Using the equation of the Wiedemann-Franz law with the thermoelectric figure of merit, we have:

$$ZT = \frac{S^2 r}{L}, \tag{1.8}$$

where $r = \frac{\kappa_e}{\kappa_l + \kappa_e}$. In metals, unlike in semiconductors, most of the heat is carried by electrons ($\kappa_e >> \kappa_l$) which means that $r \approx 1$ and $ZT \approx S^2/L$. In this case, ZT could reach a value of 1 if the Seebeck coefficient reaches $160\mu V/K$. For metallic systems, the values of S oscillates around $10\mu V/K$ which is much lower than the required value. Insulators, on the other hand, have an extremely small electrical conductivity. This gives values of ZT as small as for metals (see figure 1.4).

1.3.2 Semiconductors

At the beginning of the 20th century, it was found that some materials could have values of Seebeck coefficient as large as millivolts per Kelvin [2]. Sadly, these materials also show small values for the ratio of electrical to thermal conductivity. The reason for this is the large thermal conductivity due to phonons. However, there are other semiconductors with more modest Seebeck coefficient that possess reasonable thermal conductivities. If the material has an excess of electrons, the semiconductor is n-type and the Seebeck coefficient is negative. On the contrary, when the material is lacking electrons (excess of holes) the semiconductor is p-type and $S > 0$. As shown in figure 1.4, semiconductors with large number of carriers are more desirable for thermoelectric applications.

The so-called power factor ($S^2\sigma$) can be optimized through doping, but the increase of carriers has the drawback that it increases the electrical contribution to the thermal conductivity. On the other hand, in narrow-band gap semiconductors more than the 50 % of the heat is carried by phonons, and reducing this is the real challenge to improve thermoelectric efficiency [2]. From equation (1.8), we can see that the ideal is to have r = 1 since for

semiconductors the values of S are considerably larger than in metals.

In essence, the goal is to find a semiconductor with high power factor, but small lattice thermal conductivity compared with the electronic thermal conductivity. This leads to the concept of Phonon-Glass-Electron-Cristal (PGEC). The paradigm PGEC was proposed by Slack in 1995, and suggests that the best thermoelectric would be such that electrons are weakly scattered while the heat transported by phonons should be strongly scattered like in glasses [16].

Property	Metals	Semiconductors	Insulators
S (μV/K)	≈ 5	≈ 200	≈ 1000
σ (Ω^{-1}**cm**$^{-1}$)	$\approx 10^6$	$\approx 10^3$	$\approx 10^{-12}$
ZT	$\approx 9 \times 10^{-4}$	0.6	$\approx 2 \times 10^{-14}$

Table 1.1: Comparison of thermoelectric properties for the three mentioned groups of materials at 300 K. Table adapted from reference [17].

1.3.3 Thermoelectric compounds

There are many aspects to consider in the election of a thermoelectric material. As we mention, metallic systems have large electrical conductivity (since there are bands crossing the Fermi level) and small lattice contribution to the thermal conductivity (this because $\kappa_e >> \kappa_l$). But they also show very small values of Seebeck coefficient. Insulators, on the other hand, have very small electrical conductivity (this because the Fermi level is in the middle of the band gap). Therefore, the materials of choice are semiconductors for which both, Seebeck coefficient and electrical conductivity, are strongly linked to the carrier concentration. When the semiconductor is highly doped, the electronic thermal conductivity increases due to the large number of free carriers in the system. Also, a high doping means that the chemical potential is shifted into the bands, which increase the electrical conductivity. However, the Seebeck coefficient is reduced when the chemical potential moves away from the band edge (more details will be given in chapter 3). If the semiconductor is slightly doped, the Seebeck coefficient is large due the vicinity of the electronic gap, but the electrical conductivity decreases rapidly. This is the paradox of thermoelectricity.

For over 60 years the most-studied materials for thermoelectric applications have been those alloys with chemical formula X_2Y_3 where X is either

antimony or bismuth and Y is either tellurium or selenium [18]. These kinds of materials show extraordinary thermoelectric performance. It has been claimed that this is due to their layered nature together with the multiple valleys in their electronic band structure. Therefore, we have chosen in this work to explore another kind of materials with similar layered nature, but with tunable electronic properties. Telluride based phase-change materials (PCMs) exhibit changes in the electrical conductivity of 4 orders of magnitude related with the annealing temperature. These abrupt changes in the electrical properties, their layered nature and the expected small thermal conductivity due to the large scattering of phonons, lead us to think that PCMs could be possible good thermoelectric materials.

Chapter 2

Computational Background

In this chapter, we provide a description of the theoretical framework that we used to perform calculations of the electronic properties. We will not go deep into mathematical details, and we will limit ourselves to presenting the main concepts related with density functional theory (DFT), while in the next chapter we will introduce Boltzmann transport equations. We have used these two theories to explore the electronic and dynamical transport under pressure in the binary compound Bi_2Te_3, and the pseudo-binary chalcogenides $(GeTe)_x(Sb_2Te_3)_1$ (x = 1, 2, 3). The main reference for this chapter is the book "Electronic structure: Basic theory and practical methods" from Richard M. Martin.[19]

2.1 Density Functional Theory

Any atom, molecule, glass or crystal is made of electrons and ions. Electrons do not only work as glue in molecules and crystals due to the coulomb interaction between their negative charge and the positive charge of the nucleus. The excitations of these electrons determine electronic and optical properties in such materials. For this reason, the correct description of the interactions between the particles in any material is crucial to understand and predict its properties.

Density functional theory (DFT) is based on the postulate that any property of interacting particles can be view as a functional of its ground state electronic density $n_0(\mathbf{r})$. A functional is a function of a function, which in this case is the electronic density. DFT was developed to calculate, at modest computational cost, electronic states of solids which contain a large number

of electrons. The Hamiltonian that describes any solid is:

$$\hat{H}(\mathbf{R}, \mathbf{r}) = K_I(\mathbf{R}) + K_e(\mathbf{r}) + V_{II}(\mathbf{R}) + V_{ee}(\mathbf{r}) + V_{eI}(\mathbf{r}, \mathbf{R}), \qquad (2.1)$$

where the kinetic energy of nuclei and electrons are:

$$K_I(\mathbf{R}) = -\frac{\hbar^2}{2} \sum_I \frac{1}{M_I} \nabla_I^2, \qquad (2.2)$$

$$K_e(\mathbf{r}) = -\frac{\hbar^2}{2m} \sum_i \nabla_i^2, \qquad (2.3)$$

and the electron-electron, ion-ion and electron-ion interactions are given by:

$$V_{II}(\mathbf{R}, \mathbf{R}) = \frac{e^2}{2} \sum_{I \neq J} \frac{Z_I Z_J}{|\mathbf{R}_I - \mathbf{R}_J|}, \qquad (2.4)$$

$$V_{ee}(\mathbf{r}, \mathbf{r}) = \frac{e^2}{2} \sum_{i \neq j} \frac{1}{|\mathbf{r}_i - \mathbf{r}_j|}, \qquad (2.5)$$

$$V_{eI}(\mathbf{r}, \mathbf{R}) = -e^2 \sum_{i,I} \frac{Z_I}{|\mathbf{r}_i - \mathbf{R}_I|}, \qquad (2.6)$$

where Z_I, M_I and R_I denote the atomic number, mass and position of the ions, respectively; e, m and r_i are the electric charge, mass and position of electrons respectively. Any problem in the electronic structure of matter obeys the Schiödinger equation. Here we will focus on the time-independent Schrödinger equation[1]:

$$\hat{H}\Psi = E\Psi, \qquad (2.7)$$

where $\hat{H}$ is the Hamiltonian that describes the nature of the system while Ψ and E are the wavefunction and energy respectively. For a many-body system as a glass, crystal or molecule, the exact solution of the equation (2.7) is impossible due to the large number of particles that interact with each other. To solve equation (2.7), we need approximations. It is possible to decouple electrons and ions by taking advantage of their large difference in mass. This is the so-called adiabatic or Born-Oppenheimer approximation. In this approximation, we assume that, since electrons move much faster than ions, these will adapt instantly (adiabatically) to any move of the ions. This approximation does not only allow us to neglect the kinetic energy of the ions and solve only the electronic Hamiltonian, but it is also the starting

---

[1]For the ground state properties of the materials, the time-independent Schrödinger equation is sufficient.

point of perturbation theory used to compute electron-phonon interactions. Within the adiabatic approximation, we have:

$$\hat{H}_e \Psi_e = E_e \Psi_e, \tag{2.8}$$

$$\hat{H}_e = K_e + V_{ee} + V_{ext} = K_e + V_{ee} + \sum_i v(\mathbf{r}_i), \tag{2.9}$$

where V_{eI} has been replaced by V_{ext} since we assume that the ions are fixed and therefore the external potential is independent of $\mathbf{R}$, and only depends of the position of the electron denoted by $\mathbf{r}$. Hereafter the electron spin will be denoted by σ, then the many-electronic wavefunction is denoted by $\Psi_e(\mathbf{x}_1, \mathbf{x}_2, \ldots \mathbf{x}_N)$ where $\mathbf{x}_i = (\mathbf{r}_i, \sigma_i)$. This wavefunction must be antisymmetric, which means that:

$$\Psi(\mathbf{x}_1, \mathbf{x}_2, \mathbf{x}_3, \ldots, \mathbf{x}_N) = -\Psi(\mathbf{x}_2, \mathbf{x}_1, \mathbf{x}_3, \ldots, \mathbf{x}_N). \tag{2.10}$$

It must also be normalized:

$$\langle \Psi_e | \Psi_e \rangle = \int \int \int \ldots \int |\Psi_e|^2 d\mathbf{x}_1 d\mathbf{x}_2 d\mathbf{x}_3 \ldots d\mathbf{x}_N = 1. \tag{2.11}$$

According to equation (2.8), the electronic energy can be obtained by the expectation value of the electronic Hamiltonian applied to the electronic wavefunction:

$$E_e = \langle \Psi_e | \hat{H} | \Psi_e \rangle = \langle \Psi_e | K_e + V_{ee} + V_{ext} | \Psi_e \rangle, \tag{2.12}$$

or explicity,

$$E_e = \int \ldots \int \left[\frac{-\hbar}{2m} \sum_i \Psi_e \nabla^2 \Psi_e + \frac{e^2}{2} \sum_{i \neq j} \frac{|\Psi_i|^2}{|\mathbf{r}_i - \mathbf{r}_j|} + \sum_i |\Psi_i|^2 v(\mathbf{r}_i) \right] d\mathbf{x}_1 \ldots d\mathbf{x}_N, \tag{2.13}$$

where the integrals go over all the electrons in the system. We can see in the equation(2.13) that even when the kinetic energy of ions is neglected, and the classical interaction between ions can be easily obtained, the problem remains unsolvable. In any solid crystal there are more than 10^{23} electrons and further approximations are needed.

2.1.1 The electronic density

The electronic density is defined as the number of electrons in a given volume at a specific position in the space denoted by the vector $\mathbf{r}$. In this form the electronic density is a function of the spatial coordinates x, y and z.

$$N = \int n(\mathbf{r}) d\mathbf{r}. \tag{2.14}$$

The relation between the electronic density and the electronic wavefunction is the following:

$$n(\mathbf{r}) = N \int \ldots \int |\Psi(\mathbf{x}_1, \mathbf{x}_2 \ldots \mathbf{x}_N)|^2 d\sigma_1, d\mathbf{x}_2 \ldots d\mathbf{x}_N, \qquad (2.15)$$

which gives the probability to find any of the N electrons within the volume element $d\mathbf{r}$. The normalization condition (eq 2.11) guarantees that the integral of the electronic density is equal to the total number of electrons in the system N. In equation (2.15), one of the spatial coordinates (in this case $\mathbf{r}_1$) corresponds to the point in the space where the electronic density is evaluated.

Equation 2.13 evaluates the energy of a system of interacting electrons moving through an external potential. This external potential can be written in terms of the electronic density as:

$$V_{ext} = \int n(\mathbf{r}) v(\mathbf{r}) d\mathbf{r}. \qquad (2.16)$$

But this is the only term in equation (2.8) than can be written in terms of the density. For the kinetic energy (K_e) term, the derivative of the electronic wavefunctions makes it impossible to write it in terms of $|\Psi|^2$. In the potential energy (V_{ee}), the electronic positions in the denominator make difficult the integration term by term. With these restrictions, it is not possible to have a universal energy functional of the density. Since the two elements that remain in their "original" form are those related to the electrons, it is convenient to group them in a single term that we will be denoted by $F[\Psi_e] = K_e + V_{ee}$, total energy being:

$$E_e = F[\Psi_e] + V_{ext}[v, n]. \qquad (2.17)$$

The objective of the next section is to express the internal electronic energy in terms of the density ($F[\Psi_e] \rightarrow F[n]$). The internal electronic energy is independent of the external potential, and so should be the electronic energy functional of the density.

2.1.2 The Hohenberg and Kohn Theorems

The main idea of DFT is to describe a many-body interacting system with its density, instead of with its many-body wavefunction. This is because regardless the number of electrons in the system, the density is always dependent of 3 dimensions, while many-body wavefunction depends on 3N dimensions where N is the number of electrons in the system. This is the main reason

why DFT has become the most widely used electronic structure approach for extended systems.

Modern DFT is born in 1964 with the publication of the paper "Inhomogeneous Electron Gas" by Hohenberg and Kohn [20]. Two theorems were proposed in this paper. The first Hohenberg-Kohn theorem tells us that the ground state electronic density determines the external potential (and consequently, the Hamiltonian) of the system within a constant which only sets the absolute energy value [21]. For a system with non-degenerate ground state, the fact that the electronic density defines the external potential implies that two different potentials cannot lead to the same ground state electronic density. Moreover, the first Hohenberg-Kohn theorem indicates that the ground state electronic density determines all the ground states properties of a given system. From a physical point of view, we can say that electrons moving in an external potential react to any change in this potential to minimize their energy, and that this reaction is unique.

Since the proof of this theorem is rather simple, here we will show it. This theorem was proven by *reducto ad absurdum* argument. Let us assume that there are two potentials ($v_a(\mathbf{r})$ and $v_b(\mathbf{r})$) that differ by more than a constant and lead to the same ground state electronic density ($n_0(\mathbf{r})$). Therefore, we will have two different Hamiltonians ($\hat{H}_a$ and $\hat{H}_b$) that have the same ground state electronic density, but their normalized wavefunctions will be different (Ψ_a and Ψ_b). Then we have:

$$E_a = \langle \Psi_a | \hat{H}_a | \Psi_b \rangle < \langle \Psi_b | \hat{H}_a | \Psi_b \rangle \tag{2.18}$$

$$\langle \Psi_b | \hat{H}_a | \Psi_b \rangle = \langle \Psi_b | \hat{H}_b | \Psi_b \rangle + \langle \Psi_b | \hat{H}_a - \hat{H}_b | \Psi_b \rangle \tag{2.19}$$

$$E_a = E_b + \int n_0(\mathbf{r})[v_a(\mathbf{r}) - v_b(\mathbf{r})]d\mathbf{r}. \tag{2.20}$$

In the similar way for E_b we have:

$$E_b = E_a + \int n_0(\mathbf{r})[v_b(\mathbf{r}) - v_a(\mathbf{r})]d\mathbf{r}. \tag{2.21}$$

If we add $E_a + E_b$ we will have the inequality $E_a + E_b < E_b + E_a$, which is a clear contradiction. This establishes what we have mentioned before; there cannot exist two external potentials that differ by more than a constant, that lead to the same non-degenerate ground state electronic density. Regardless the importance of this result, which is not trivial, this theorem does not show how to solve the problem of interacting electrons moving in the potential of the nuclei.

The second Hohenberg-Kohn theorem is the DFT variational principle. This theorem states that the minimum in energy is reached only when the electronic density is the ground state electronic density. Basically, a universal functional of the energy in terms of the electronic density ($E[n(\mathbf{r})]$), can be defined for a given external potential. The electronic density that minimizes this functional is the ground state electronic density. In other words, we can assume an electronic density and its related Hamiltonian and wavefunction. Therefore, it is possible to associate this assumed electronic density to its corresponding energy, but the energy will only be minimized when the assumed electronic density is equal to the ground state electronic density.

$$\langle \Psi_{as}|\hat{H}_{as}|\Psi_{as}\rangle = E_{as} \geq E_0, \tag{2.22}$$

where E_0 and E_{as} are the energy of the ground state, and the assumed energy resulting from the assumed electronic density, respectively. The Hohenberg-Kohn theorems allow us to obtain the ground state energy by minimizing the energy functional

$$E[n(\mathbf{r})] = \int n(\mathbf{r})v(\mathbf{r})d\mathbf{r} + F[n(\mathbf{r})], \tag{2.23}$$

but the universal functional $F[n(\mathbf{r})]$ is unknown. This means that, if the universal functional were known, the ground state density and energy would be obtained by minimizing the total energy of the system with respect to variations of the electronic density. Figure 2.1 shows a schematic representation of the Hohenberg-Kohn formalism. The density functional of the energy describes the ground state of a given system, and does not provide any information about exited states.

2.1.3 The Kohn-Sham equation

The Hohenberg-Kohn theorems proves that it is possible to choose any arbitrary electronic density, and only one external potential corresponds to this electronic density. Therefore, the Hamiltonian and all the related properties will be unique as well. Also, the minimum in energy can be obtained by the variational principle. This is, basically, the energy minimization through variations of the electronic density (equation (2.23)).

At this level, DFT remains unapplicable because there is no simplification at all: the Schródinger equation must to be solved for a system of interacting electrons moving in an external potential. The Kohn-Sham ansatz basically replaces one problem with another [22]. Kohn and Sham proposed a mapping
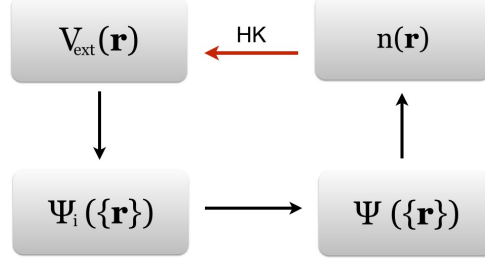
Figure 2.1: Schematic representation of the Hohenberg-Kohn formalism. Black arrows represent the usual solution of Schrodinger equation. The red arrow represents the Hohenberg-Kohn formalism, where the electronic density determines the external potential.

from the real system, where the particles interact with each other, to another with Kohn-Sham particles (particles that do not interact each other) moving through an effective potential. The Hamiltonian of this new system is a linear combination of the one electron Hamiltonian. We start by dividing the universal functional $F[n(\mathbf{r})]$ into three parts:

$$F[n(\mathbf{r})] = K_{ks}[n(\mathbf{r})] + V_H[n(\mathbf{r})] + E_{xc}[n(\mathbf{r})], \tag{2.24}$$

where $K_{ks}[n(\mathbf{r})]$ is the functional of the kinetic energy for the non-interacting Kohn-Sham particles with electronic density $n(\mathbf{r})$; $V_H[n(\mathbf{r})]$ is the classic electrostatic potential between electrons (Hartree potential) and $E_{xc}[n(\mathbf{r})]$ is the so-called exchange-correlation energy, that contains all the missing information lost during the mapping from the real system. This energy does not only take care of all the non-classical part of the potential, but also includes the difference between $K_{ks}[n(\mathbf{r})]$ and the true kinetic energy of the system with interacting particles. With this, it is possible to solve the one-electron Schrödinger equation with the help of Kohn-Sham orbitals ψ_i, and with the restriction that the number of particles in the system is fixed $(n(\mathbf{r}) = \sum_i |\psi_i|^2)$.

$$\left(-\frac{1}{2}\nabla^2 + v(\mathbf{r}) + \int \frac{n(\mathbf{r}')}{|\mathbf{r} - \mathbf{r}'|} d\mathbf{r}' + v_{xc}(\mathbf{r}) \right) \psi_i = \epsilon \psi_i, \tag{2.25}$$

where the exchange-correlation potential is:

$$v_{xc} = \frac{\delta E_{xc}[n(\mathbf{r})]}{\delta n(\mathbf{r})}. \tag{2.26}$$

18

We can now define a total effective potential in which the Kohn-Sham particles are moving. This effective potential is given by the sum of the kinetic energy of non-interacting particles, the external potential due to the nuclei and the exchange-correlation potential:

$$v_{eff} = v(\mathbf{r}) + \int \frac{n(\mathbf{r}')}{|\mathbf{r} - \mathbf{r}'|} d\mathbf{r}' + v_{xc}(\mathbf{r}). \qquad (2.27)$$

Finally, we can write the one-electron Schrödinger equation in the compact form:

$$\left(-\frac{1}{2}\nabla^2 + v_{eff}\right)\psi_i = \epsilon\psi_i. \qquad (2.28)$$

We should note that the effective potential v_{eff} depends only, but in a non-local way, on the electronic density $n(\mathbf{r})$. The Kohn-Sham equation can be solved iteratively. For example, it is possible to construct an effective potential with equation (2.27), and then to obtain the Kohn-Sham orbitals. Based on these new orbitals, it is possible to get a new density by:

$$n(\mathbf{r}) = \sum_i |\psi_i|^2, \qquad (2.29)$$

and repeat the process until convergence has been achieved. The Kohn-Sham ansatz solves the many-body problem completely. In theory, DFT is exact, but in practice approximations have to be made. These approximations are made in the exchange-correlation energy.

2.2 The exchange-correlation energy

The main problem of DFT is that the exchange and correlation (xc) energy functionals are unknown, except for the homogeneous free electron gas. The exchange-correlation energy takes into account the difference between the classical and the quantum mechanical electron-electron repulsion, and the difference between the kinetic energy of the real system, and that of the Kohn-Sham particles system. The exchange energy refers to the energy needed to interchange two electrons with the same spin. Electrons are fermions, therefore, their wavefunctions must be antisymmetric (equation (2.10)). The correlation energy is related to the fact that the electrons interact with each other while the Kohn-Sham particles not. One of the most widely used approximations to the exchange-correlation energy is the so-called Local Density Approximation (LDA). Under this approximation the
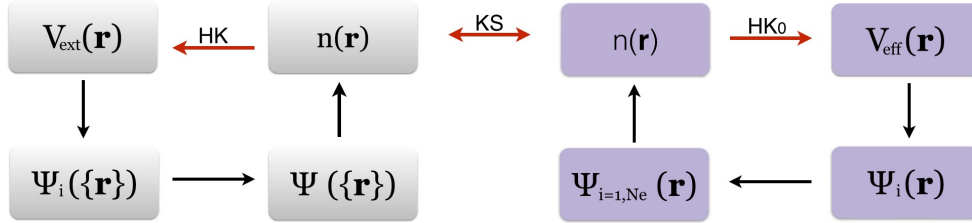
Figure 2.2: Schematic representation of the Kohn-Sham ansatz. The red arrow labeled with HK_0 represent the Hohenberg-Kohn formalism applied to the system of non-interacting particles. The red arrow labeled with KS represents the connection in both directions between the problem with non-interacting particles and the problem of interacting particles.

functional depends locally of the density at the place where the density is evaluated. Then the exchange-correlation energy is assumed to be the same as in the homogeneous electron gas with that density,

$$E_{xc}^{LDA}[n(\mathbf{r})] = \int n(\mathbf{r})\epsilon_{xc}^{hom}[n(\mathbf{r})]d\mathbf{r}. \tag{2.30}$$

Even though LDA is a strong approximation that should be valid only for systems where the density varies slowly, calculations in atoms, molecules and solids show that LDA works well for many systems. In general, calculations with LDA produce a chemical bonding that is stronger than in actual systems. This leads to the underestimation of the lattice parameters for solids and, therefore, the bulk modulus is overestimated. Another drawback of LDA is the systematic underestimation of the electronic bandgap with respect to experiments. This is related to the intrinsic nature of DFT and not to the exchange-correlation energy approximation, given that DFT is a ground state theory, while the electronic gap depends on excited states.

To improve the results obtained with LDA, other approximations have been developed. In the popular generalized gradient approximation, or GGA, the exchange-correlation energy depends not only on the local density but also on its gradient:

$$E_{xc}^{GGA}[n(\mathbf{r})] = \int n(\mathbf{r})\epsilon_{xc}^{hom}[n(\mathbf{r}), |\nabla|]d\mathbf{r}. \tag{2.31}$$

With this, the accuracy of the calculation is usually increased. There have been many approximations developed to reach better accuracy such as revPBE, RPBE, PBE-WC or PBEsol [23], this last one offering a better representation of solids and surfaces. The so-called meta-GGA uses up to the second derivative of the density and/or kinetic energy. The hybrid functionals offers exact exchange from the Hartree-Fock theory. In this thesis we use the PBEsol correction for the GGA approximation since is the one that shows better accuracy with respect to experimental data for pseudo-binary compounds [24].

2.3 Pseudopotentials

Another way to reduce computational cost in DFT calculations is through the use of pseudopotentials. The Kohn-Sham wavefunctions used in equation (2.29) to obtain the electron density are expanded into a convenient basis set. In crystals with periodic boundary conditions, the KS wavefunctions obey the Bloch theorem and are labeled for the wavevector $\mathbf{k}$ and band index n. In practice, this expansion of the basis set with boundary conditions is done with planewaves. The disadvantage of planewaves is that a large number of these is required to describe the atomic wavefunctions close to the nucleus. The wavefunctions of the valence electrons vary rapidly in the region near to the nucleus, therefore, planewaves with high energies are necessary to describe these wavefunctions correctly whether low energy planewaves are sufficient to describe electrons far from the nucleus.

The main goal of the pseudopotential approximation is to replace the strong Coulomb potential of the nucleus by an effective ionic potential acting on the valence electrons only. The pseudo wavefunction have no radial nodes in the core region (see figure 2.3), while the pseudopotential is smoother than the all-electron potential near to the nucleus but identical after a defined parameter denoted as r_c. The two mentioned properties of pseudopotentials make it possible to compute KS wavefunctions with a relative small number of planewaves (the maximal energy limit of the planewaves basis will be called energy cutoff in the following). The Vienna ab-initio simulation package (VASP) [7, 8, 9] adopts the planewaves basis set, and the projector-augmented wave method (PAW) to construct the pseudopotentials [25]. The PAW approach uses pseudopotential operators but keeps all-electron core wavefunctions.
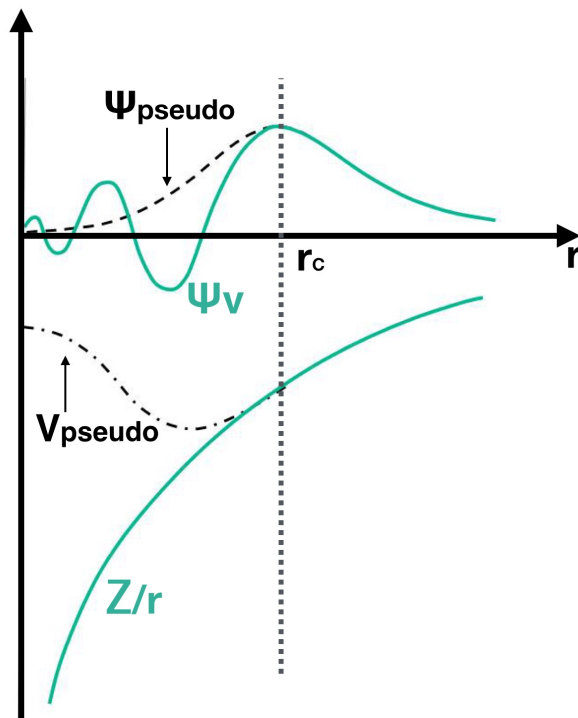
Figure 2.3: Schematic representation of the pseudopotential and the pseudo wavefunction. The real and the pseudopotential match beyond a given cutoff radius r_c. Notice that the pseudo wavefunction is nodeless before r_c and the pseudopotential is much weaker than the real potential in the core region.

Chapter 3

Boltzmann Transport Equation

The objective of this thesis is to calculate thermoelectric properties of tellurium based compounds. DFT has been used to obtain the minimum energy structure and, the ground state energy for each band with index n and a wavevector $\mathbf{k}$ ($E_0(n, \mathbf{k})$). Boltzmann transport theory, as implemented in the BOLTZTRAP code [10], uses $E_0(n, \mathbf{k})$ to determine thermoelectric properties of the compounds. On the other hand, the second- and third-order interatomic force constants are used to calculate the lattice contribution to the thermal conductivity, through Boltzmann transport equations (BTE) for phonons as implemented in the ShengBTE code [11]. BTE provides a method which is accurate and computationally inexpensive to calculate thermoelectric transport coefficients. Hereafter, we explain some generalities of BTE and the mentioned codes.

3.1 Boltzmann transport equation (BTE) for electrons

In general, transport theory aims at describing the flow of carriers due to external fields which lead the system to be out of equilibrium. The Boltzmann transport equation describes the statistical behavior of a thermodynamic system away from thermodynamic equilibrium. We start by supposing that electrons in the conduction bands, and holes in the valence band can be considered as free carriers. The response of these carriers to an applied electric field (or a gradient of temperature) depends on the strength of the field. An electric field (or temperature gradient) induces electrical (or thermal) currents. The flow of the carriers due to these fields is limited by the scattering processes between them and with other (quasi)particles. The exchange

Figure 3.1: Schematic representation the trajectory of a particle with momentum p_x moving in the cartesian axis x. It is assumed that the scattering process is fast and the particle just changes its momentum and not its position.

of momentum and energy due to these interactions gives finite thermal or electrical conductivities.

The Boltzmann theory introduces the so-called transport distribution function to describe an electron system. When the system is in equilibrium this distribution function is given by the Fermi function. Outside of equilibrium, the distribution function depends on the spatial coordinates ($\mathbf{r}$), the particles momuntum ($\mathbf{p}$) and time (t), characterized by $f(\mathbf{r}, \mathbf{p}, t)$. This distribution is the probability to find a particle with at given momentum in a specific posistion at certain time. Therefore, $\int f(\mathbf{r}, \mathbf{p}, t) d\mathbf{r}^3 d\mathbf{p}^3 / (2\pi\hbar)^3 = N$, where N is the number of particles in the system. The distribution function f requires semiclassical treatment, since we must specify the momentum and position for individual particles.

The equation that describes the change of the distribution function with time is the counterpart of the Schrödinger equation which specifies the change of the wavefunction with time [26]. The time evolution of the probability to find a particle with momentum $\mathbf{p}$ and position $\mathbf{r}$ obeys the Boltzmann transport equation. Let us assume that the particle is moving with a two-dimensional trajectory $T[x(t), p_x(t)]$. Now, in the absence of scattering, the probability to find the particle in such trajectory is given by $f_0(x, p_x, t)$, and this probability remains constant with time (see figure 3.1). If we follow the occupied state through the characteristic trajectory of the particle, this state remains occupied in time. We should get the same result if we follow an unoccupied state, where f remains zero with time. With this, we get the

transport equation.

$$\frac{df}{dt} = 0. \tag{3.1}$$

In other words, the probability to find a particle in a state with position $\mathbf{r} + \Delta\mathbf{r}$ and with momentum $\mathbf{p} + \Delta\mathbf{p}$ at time $t + \Delta t$ is equal to the probability to find the same particle in the state $f(\mathbf{r}, \mathbf{p}, t)$:

$$f(\mathbf{r}, \mathbf{p}, t) = f(\mathbf{r} + \Delta\mathbf{r}, \mathbf{p} + \Delta\mathbf{p}, t + \Delta t). \tag{3.2}$$

The equations (3.1) and (3.2) neglect the possibility of scattering. If the particles interact and scatter events occur, we can write in six dimensions (three spatial and three of momentum) that:

$$\frac{\partial f}{\partial t} + \frac{\partial f}{\partial \mathbf{r}}\frac{\partial \mathbf{r}}{\partial t} + \frac{\partial f}{\partial \mathbf{p}}\frac{\partial \mathbf{p}}{\partial t} = \left.\frac{\partial f}{\partial t}\right|_{coll}, \tag{3.3}$$

where the term on the right is the change in distribution function due to collisions. With the use of semiclassical equations:

$$\frac{\partial \mathbf{r}}{\partial t} = \mathbf{v} \tag{3.4}$$

$$\frac{\partial \mathbf{p}}{\partial t} = \mathbf{F}, \tag{3.5}$$

we can get:

$$\frac{\partial f}{\partial t} = -\frac{\partial f}{\partial \mathbf{r}} \cdot \mathbf{v} - \frac{\partial f}{\partial \mathbf{p}} \cdot \mathbf{F} + \left.\frac{\partial f}{\partial t}\right|_{coll}. \tag{3.6}$$

According to equation (3.6), there are three main contributions to the change of the transport distribution function with time. The first term on the right side refers to electrons moving out of that specific region in space with a characteristic velocity equal to $\mathbf{v}$. If the distribution function varies in space, the number of particles entering the region in space will be different from those particles leaving that region. The second term comes from the fact that the particles are moving into different momentum states. Similar to the first term, if the distribution function varies with the momentum, the number of particles transferred into that specific region of momentum will differ from the particles that are leaving such region. Finally, the last term includes the probability that electrons scatter out more rapidly than they scatter in. The collision term makes the Boltzmann transport equation difficult to solve, and without it the solution is unphysical. Nevertheless, it is possible to get the numerical solution through Monte-Carlo simulation. This method allows treating the collision term in great detail. On the other hand, to obtain an analytical solution of the BTE, it is necessary to simplify the collision term drastically [26].

3.1.1 The Relaxation Time Approximation (RTA)

If the distribution function is in equilibrium, there are no scattering events and f is unchanged with time. Now, if the distribution function for a single state/electron is out of equilibrium, we expect that f decays exponentially to its equilibrium state.

$$\left.\frac{\partial f}{\partial t}\right|_{coll} = -\frac{f - f_0}{\tau}, \tag{3.7}$$

where τ is the electron relaxation time. Even though the RTA agrees very well with many experimental data it is still an approximation. Strictly speaking, the relaxation time approximation is justified only when the scattering is homogeneous. If the distribution function is inhomogeneous (different electron density at different points), the equilibrium distribution function must be written in terms of the local density, otherwise we will be introducing scattering events than instantaneously transfer electrons from one position to another. Nevertheless, the RTA leads to a good description of many transport properties.

By the combination of equations (3.7) and (3.6), we get the Boltzmann transport equation with the collision term within the relaxation time approximation.

$$\frac{\partial f}{\partial t} = -\frac{\partial f}{\partial \mathbf{r}} \cdot \mathbf{v} - \frac{\partial f}{\partial \mathbf{p}} \cdot \mathbf{F} - \frac{f - f_0}{\tau}. \tag{3.8}$$

Now, if we take the equation (3.8) and we assume spatial uniformity $\partial f / \partial \mathbf{r} = 0$ and in absence of fields ($\mathbf{F} = 0$) this equation is:

$$\frac{\partial f}{\partial t} = -\frac{\delta f}{\tau}, \tag{3.9}$$

where $\delta f = f - f_0$. The solution of equation (3.9)

$$\delta f(t) = \delta f(0) e^{\frac{-t}{\tau}}. \tag{3.10}$$

This equation means that, if the system is out of equilibrium, it will decay exponentially to equilibrium with a single characteristic time τ. This is a very reasonable assumption and, as we mentioned, it works for many systems. Finally, the equation (3.8) can be rewritten in terms of f_0 and $(f - f_0)$:

$$\frac{\partial f_0}{\partial t} + \frac{\partial (f - f_0)}{\partial t} + \frac{\partial f_0}{\partial \mathbf{r}} \cdot \mathbf{v} + \frac{\partial (f - f_0)}{\partial \mathbf{r}} \cdot \mathbf{v} + \frac{\partial f_0}{\partial \mathbf{p}} \cdot \mathbf{F} + \frac{\partial (f - f_0)}{\partial \mathbf{p}} \cdot \mathbf{F} = \frac{f - f_0}{\tau}. \tag{3.11}$$

To linearize this equation, further approximations are needed:

1. $|f - f_0| << f_0,$

2. the gradient of $f - f_0$ is much smaller than the gradient of f_0,

3. changes in the external fields occurs much slower than τ.

With these considerations, many terms in the equation (3.11) disappear and the linearized Boltmann transport equation is:

$$f = f_0 + \tau \left(\mathbf{v} \cdot \frac{\partial f_0}{\partial \mathbf{r}} + \frac{f_0}{\partial \mathbf{p}} \cdot \mathbf{F} \right). \tag{3.12}$$

The Boltzmann theory is a powerful tool to obtain transport coefficients of real materials. Before going into detail with the microscopic model of the transport properties, we will define some macroscopic properties. For an isotropic solid, the relation between the electrical current $\mathbf{J}$, the electric field $\mathbf{E}$ and a gradient of temperature ΔT is given by:

$$\mathbf{J} = \sigma \mathbf{E} + \zeta \Delta T, \tag{3.13}$$

where σ is the electrical conductivity and $\zeta = S\sigma$ where S is the Seebeck coefficient. Here, S is defined as the difference in voltage produced by a given temperature gradient when the electrical current is zero. Now, for the microscopic model of transport, in general, the electrical current of carriers is defined by:

$$\mathbf{J} = e \sum_{\mathbf{k}} f_{\mathbf{k}} \mathbf{v}_{\mathbf{k}}, \tag{3.14}$$

where e is the charge of the carriers (electrons or holes) and $f_{\mathbf{k}}$ is the population associated to the quantum state $\mathbf{k}$ (here $\mathbf{p} = \hbar \mathbf{k}$). $\mathbf{v}_{\mathbf{k}}$ is the group velocity and is given by:

$$\mathbf{v}_{\mathbf{k}} = \frac{1}{\hbar} \frac{\partial \epsilon}{\partial \mathbf{k}}. \tag{3.15}$$

The population of the $\mathbf{k}$ states is given by the solution of the BTE. The change in the population depends on the diffusion, the electric ($\mathbf{E}$) and the magnetic ($\mathbf{B}$) fields, or on the scattering:

$$\frac{df_{\mathbf{k}}}{dt} = -\mathbf{v}_{\mathbf{k}} \cdot \frac{\partial f_{\mathbf{k}}}{\partial \mathbf{r}} - \frac{e}{\hbar} \left(\mathbf{E} + \frac{1}{c} \mathbf{v}_{\mathbf{k}} \times \mathbf{B} \right) \cdot \frac{\partial f_{\mathbf{k}}}{\partial \mathbf{k}} + \frac{df}{dt} \bigg|_{coll}. \tag{3.16}$$

3.2 The BOLTZTRAP Code

The BOLTZTRAP code allows the calculation of semi-classical transport coefficients through the use of Fourier expansions to solve Boltzmann equations. In the absence of fields, the stationary solution of the Boltzmann equation is

the Fermi distribution function $f_0(\epsilon_\mathbf{k})$. The fact that the population in k and $-k$ is the same makes $\mathbf{J} = 0$. In absence of magnetic field and temperature gradients, it is possible to linearize equation (3.16) within the relaxation time approximation (equation 3.12), and we obtain the following solution for the population:

$$f_\mathbf{k} = f_0(\epsilon_\mathbf{k}) + e\left(-\frac{\partial f_0}{\partial \epsilon}\right)\tau_\mathbf{k}\mathbf{v}_\mathbf{k} \cdot \mathbf{E}. \tag{3.17}$$

Now that we obtained the population of states thanks to BTE within the RTA, we substitute equation (3.17) into (3.14) to get:

$$\mathbf{J} = e\sum_\mathbf{k} f_\mathbf{k}\mathbf{v}_\mathbf{k} = ef_0(E_\mathbf{k})\sum_\mathbf{k} \mathbf{v}_\mathbf{k} + e^2\sum_\mathbf{k}\left(\frac{-\partial f_0}{\partial \epsilon}\right)\mathbf{v}_\mathbf{k}\mathbf{v}_\mathbf{k}\tau_\mathbf{k} \cdot \mathbf{E}. \tag{3.18}$$

From equation (3.13) it is easy to see that in the absence of a gradient of temperature, the macroscopic electrical current is $\mathbf{J} = \sigma \cdot \mathbf{E}$, therefore:

$$\sigma = e^2\sum_\mathbf{k}\left(-\frac{\partial f_0}{\partial \epsilon}\right)\mathbf{v}_\mathbf{k}\mathbf{v}_\mathbf{k}\tau_\mathbf{k} = \sum_\mathbf{k}\left(-\frac{\partial f_0}{\partial \epsilon}\right)\sigma(\mathbf{k}), \tag{3.19}$$

where $\sigma(\mathbf{k}) = e^2\mathbf{v}_\mathbf{k}\mathbf{v}_\mathbf{k}\tau_\mathbf{k}$. In the same way as for the density of states, the energy dependence of the conductivity tensor can be obtained by:

$$\Xi(\epsilon) = \frac{1}{N}\sum_\mathbf{k}\sigma(\mathbf{k})\frac{\delta(\epsilon - \epsilon_\mathbf{k})}{d\epsilon}. \tag{3.20}$$

With this, the transport tensors that depend on the chemical potential (μ) and temperature (T) can be obtained through:

$$\sigma(T;\mu) = \frac{1}{\Omega}\int \Xi(\epsilon)\left[-\frac{\partial f_\mu(T;\epsilon)}{\partial \epsilon}\right]d\epsilon \tag{3.21}$$

$$S(T;\mu) = \frac{1}{\Omega e T\sigma(T;\mu)}\int \Xi(\epsilon)(\epsilon - \mu)\left[-\frac{\partial f_\mu(T;\epsilon)}{\partial \epsilon}\right]d\epsilon, \tag{3.22}$$

where the electrical conductivity still depends on the relaxation time τ, but not the Seebeck coefficient. τ is considered constant (no longer $\mathbf{k}$ dependent) and can be taken out of the integral in equation (3.22). This is known as the constant relaxation time approximation (CRTA). Here the bands are needed to perform the calculations, but the BOLTZTRAP code neglects the effect of temperature in such bands.

The carrier concentration is expressed within the rigid band approximation, which assumes that the bands are independent of the change in doping,

and only shifts the chemical potential into the conduction (or valence) bands. The rigid band approximation is strong, but it often works very well. In fact, there is a report in which the BOLTZTRAP code has been used to compute the effect of Tl doping into PbTe [27]. In this report, it has been proved that the doping of Tl does not change anything in the shape of the bands, and the improvement in the Seebeck coefficient is due to the mentioned shift of the chemical potential. On the other hand, another work showed that for the same compound [28], the BOLTZTRAP code overestimates the values of S when the system is doped either with Na, K or Ag_2Te. However, the authors suggest that this overestimation is related to the CRTA, and not to the rigid band approximation. The same work shows remarkable agreement with experiments for the n-type PbTe within CRTA and rigid band approximation.

3.3   BTE for phonons

The thermal conductivity, noted κ, is a key property for thermoelectric applications. As we mentioned in chapter 1, the Phonon-Glass-Electron-Crystal is an utopic concept that, in principle, gives optimal thermoelectric performance. For this reason, many recent efforts have aimed at decreasing the thermal conductivity to the glass limit. In the case of non-magnetic semiconductors, the principal carriers of heat are the phonons, therefore it is reasonable to assume that the main contribution to the total thermal conductivity in such materials comes from phonons. The properties of phonons, such as frequencies or velocities, can be calculated via interatomic force constants (IFCs). For example, at each $\mathbf{q}$ point, the phonon frequencies are computed using the 2nd-order IFCs, and the group velocity of such phonon is the derivative of the phonon dispersion $\partial\omega/\partial\mathbf{q}$.

Nowadays the calculation of the second-order interatomic force constants is a very straightforward calculation even for complex systems. It is possible to compute IFCs via density functional perturbation theory (DFPT) where the displacement of the atoms is treated as perturbations to the system. Another possibility is the so-called finite displacement method. This method uses real-space supercells where the IFCs are calculated from the forces on atoms subject to finite displacements [29].

The thermal properties of solids can be obtained by the Boltzmann transport equation for phonons, but the full solution of this equation is complicated and computationally demanding. This is mainly because the relaxation

time must be calculated, unlike in the case of electrons where the relaxation time is considered constant. In the electronic case, most of the interesting phenomena involved in transport occur in the vicinity of the gap (around the Fermi level), while for phonons, all the modes contribute to the scattering, therefore increasing the computational cost. We must point out that RTA differs from CRTA since RTA is the approximation used to solve the BTE, and CRTA requires that the relaxation time does not change significantly with the wavevector, so that τ can be considered a constant.

There have been many efforts to compute accurately lattice thermal conductivity (phonon contribution to the total thermal conductivity) by solving BTE, especially within the relaxation time approximation [30]. Even though RTA gives accurate results for bulk systems such as Si [31], Ge [32], diamond [33], MgO [30] and others, the full solution of the Boltzmann transport equation is needed whenever the phonon processes are more complex. The ShengBTE [11] is a parameter-free ab-initio code that allows to compute the lattice thermal conductivity, for bulk solids and nanowires from first principles through the iterative solution of the Boltzmann transport equation for phonons.

So far, we had mentioned just the second-order IFCs which correspond to pure harmonic oscillators. If the solids only have harmonic vibrations, the lattice thermal conductivity will be infinite, giving perfect heat conduction. This means that the phonons in the solid do not interact at all (infinitely large phonon life-times), and they can freely travel through the solid. We know that this is not true in real systems. The intrinsic thermal resistivity in semiconductors and insulators arises from the non-harmonic dependence of the interatomic potential, which causes the interaction between phonons. [34, 31] If the phonon life-times and the lattice thermal conductivity are needed, a correct description of these anharmonic oscillations is necessary. The anharmonic oscillations are characterized by the third-order IFCs.

Similar to what we did in the previous section, we will start from the definition of the macroscopic heat current. The Fourier law gives the rate of heat flow $\mathbf{Q}$ per unit of area normal to a non-zero gradient of temperature ΔT across a solid.

$$\mathbf{Q}_i = -\sum_j \kappa_{ij} \Delta T_j, \tag{3.23}$$

where κ_{ij} is the thermal conductivity tensor. This tensor is calculated in the ShengBTE code by the solution of the linearized Boltzmann equation. In

this equation, the distribution function of phonons is denoted by n (this to avoid confusions with the electronic distribution function f). In the absence of a temperature gradient or any other thermodynamic force, the phonon distribution functions obeys the Bose-Einstein statistic ($n_0(\omega_\lambda)$, where ω is the angular frequency and λ comprises both the phonon branch index and a wavevector). Two processes could change the phonon distribution function from its equilibrium state: diffusion due to the gradient of temperature and the scattering coming from the allowed processes:

$$\frac{dn_\lambda}{dt} = \frac{\partial n_\lambda}{\partial t}\bigg|_{diff} + \frac{\partial n_\lambda}{\partial t}\bigg|_{coll} = 0, \tag{3.24}$$

where

$$\frac{\partial n_\lambda}{\partial t}\bigg|_{diff} = -\Delta T \cdot \mathbf{v}_\lambda \frac{\partial n_\lambda}{\partial T}, \tag{3.25}$$

where $\mathbf{v}_\lambda$ is the group velocity of the phonon mode λ. Now, the collision term in equation (3.24) depends on the specific scattering process. For single crystals, the phonons can be scattered due to phonon-phonon interactions or due to interaction with impurities. To make the calculation more practical, n_λ can be expanded to first order in ∇T. We assume that the norm of ∇T is small. Therefore we can approximate $n_\lambda = n_0(\omega_\lambda) - \mathbf{F}_\lambda \cdot \Delta T \frac{dn_0}{dT}$ where we explicitly define a linear dependence on ∇T. We define $\mathbf{F}_\lambda$ as:

$$\mathbf{F}_\lambda = \tau_\lambda^0(\mathbf{v}_\lambda + \Delta_\lambda). \tag{3.26}$$

Where the only scattering sources allowed are the two- and three-phonon processes, which result in the linearized BTE. In equation (3.26), τ_λ^0 is the relaxation time of λ which is commonly used within the RTA. Δ_λ is in units of velocity and refers to how much the population differs from the RTA. Therefore, if $\Delta_\lambda = 0$ the results correspond to those obtained within relaxation time approximation. Here Δ_λ includes the two-phonon processes and the absorption and emission process of the three-phonon scattering (Fig. 3.2). It also includes the normal and the "umklapp" processes (Fig. 3.3). For more details of the form of Δ_λ see the paper of Wu Li and co-workers [11] and the chapters 4 [35] and 5 [36] of the book "Length-scale dependent phonon interactions".

In the ShengBTE code, the equation (3.26) is solved iteratively starting from the zero-order or RTA where $\Delta_\lambda = 0$. The stopping criterion is when the relative change in the conductivity tensor is less than a configurable parameter with a default value of 10^{-5} [11]. The lattice thermal conductivity
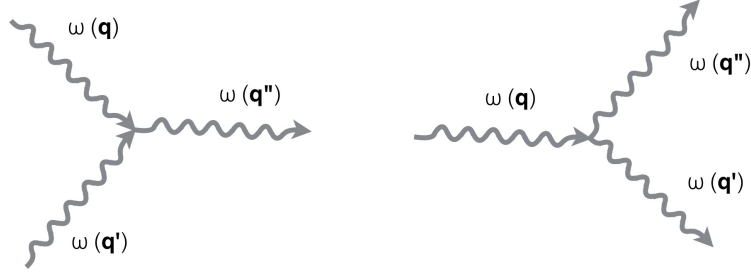
Figure 3.2: Schematic representation of the three phonon scattering. The left panel shows the absorption process in which one phonon ($\mathbf{q}$) scatters by absorbing another mode ($\mathbf{q}'$) which yield a third mode ($\mathbf{q}''$). On the right panel is shown the other scattering process in which a phonon mode ($\mathbf{q}$) decays into two phonon modes ($\mathbf{q}'$) and ($\mathbf{q}''$).

tensor under the mentioned approximations is given by the equation:

$$\kappa_\lambda = \frac{1}{k_B T^2 \Omega N} \sum_\lambda n_0(n_0 + 1)(\hbar\omega_\lambda)^2 \mathbf{v}_\lambda \mathbf{F}_\lambda, \qquad (3.27)$$

where Ω is the volume of the unit cell and k_B is the Boltzmann constant. The determination of the three-phonon scattering is the most time consuming calculation, but it is improved with the inclusion of symmetry where only the $\mathbf{q}$ points inside the irreducible Brillouin zone are needed.

Now that the theory behind the code has been introduced, we explain the workflow of how the lattice thermal conductivity can be obtained using the ShengBTE code. As we just explained, to compute the lattice thermal conductivity the second and third order interatomic force constants are needed. First, we must obtain the second order interatomic force constants. These IFCs allow to get the eigenvalues that lead to the phonon dispersion curves. Then the phonon group velocities and the Bose-Einstein populations can be obtained (see equation (3.27)). The need of real-space supercell approach limits accurate results. Under this approximation the supercell can contain thousands of atoms which is computationally expensive. Nevertheless, it is not an impossible task for systems with moderate number of atoms in the primitive cell. After we get the 2nd-order IFCs, the third order interatomic force constants should be obtained. These 3rd-order IFCs are used to compute the three-phonon scattering matrix elements, which together with the
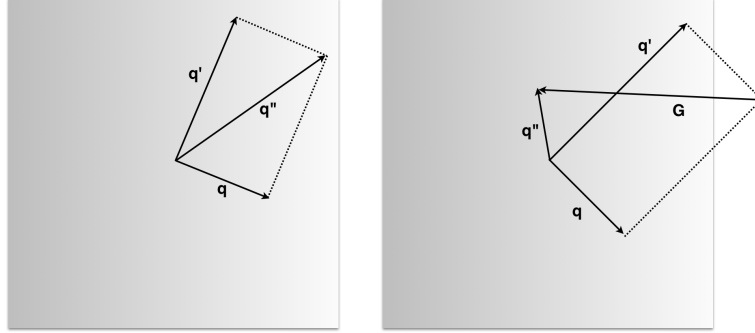
Figure 3.3: Schematic representation of the two types of phonon process. The left panel shows the normal process in which the direction of the energy flow is preserved while the right panel shows the "umklapp" process in which the direction of the energy flow is reversed and the momentum conservation is given by $\mathbf{q} + \mathbf{q}' = \mathbf{q}'' + \mathbf{G}$ where $\mathbf{G}$ is a reciprocal lattice vector.

phonon frequencies and populations, lead to the phonon relaxation times. The real-space supercell approach is also needed. As well as for the 2nd-order IFCs, the third order force constants decay with the distance between atoms. Therefore, the supercell should be large enough for the forces between farthest atoms to diminish to negligible values. In the ShengBTE code, the farthest neighbor can be selected to reduce the computational cost, but this parameter should be treated carefully. In some cases, interactions up to fourth neighbors can be significant [37]. Finally, to compute the lattice thermal conductivity, the reciprocal space has to be discretized into a grid of $\mathbf{q}$ points, and the lattice thermal conductivity is calculated using equation (3.27). Figure 3.4 shows the workflow that we follow to obtain the lattice contribution to the thermal conductivity using the ShengBTE code.
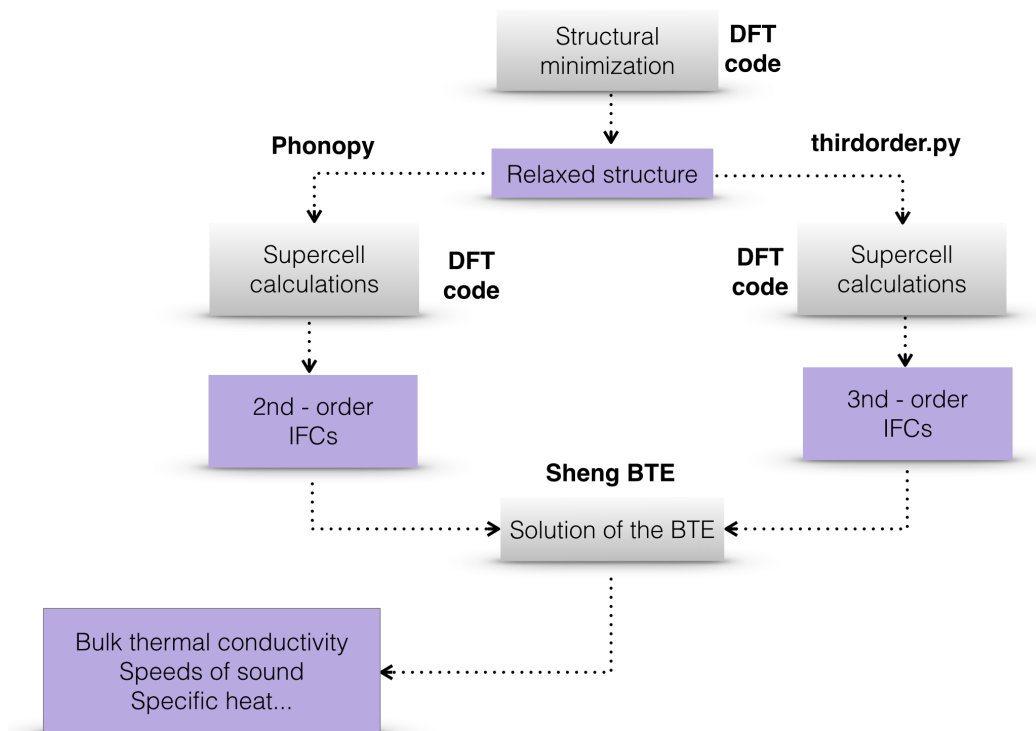
Figure 3.4: Workflow to obtain the lattice thermal conductivity within the real-space supercell approach. Purple boxes denoted results obtained, while gray boxes stand for steps in the calculations. Figure adapted from reference [11]
.

Chapter 4

Bi$_2$Te$_3$ under pressure

Each material possesses a unique combination of properties, and it is our work to find the compound that shows the properties necessary for specific applications. The number of possible thinkable materials is huge, and synthesizing new materials to measure such properties is expensive and unwise. The application of pressure allows the manipulation of a fundamental parameter in solids, the interatomic distance. The properties of the materials are strongly linked to their lattice parameters and, therefore, to the interaction of the involved elements. In this way, it is possible to follow the evolution of a given property through the application of pressure. For example, it has been found that the band structure of semiconductors exhibit a strong dependence with P [38].

From the experimental point of view, appling pressure to materials provides interesting results concerning intrinsic properties of such compounds that could lead to new TE materials with large ZT. The goal of appliying pressure is to improve thermoelectric properties by changing the lattice parameters; afterwards, improved properties under pressure could provide targets that lead the synthesis of new materials. Another possibility consists in inducing such pressure by synthesis procedures [39].

Pressure, as well as temperature, has a strong influence in the DOS of the materials, especially in the vicinity of the energy gap, which is where the most interesting phenomena related to thermoelectricity occur.

One of the advantages of pressure tuning, unlike temperature, is that the changes caused by pressure are often not associated with large changes in entropy [40]. Another advantage of pressure tuning is that it is fast and clean

and does not, in general, introduce disorder or phase separation. Moreover, recent developments in high pressure techniques allow the measure of a wide variety of properties "in situ" during the process of compression, or during the release of pressure. The properties that can be measured are, among others, the electrical conductivity, the Seebeck coefficient, the magnetic and optical properties, or the crystal structure for pressure ranging from ambient up to typically 100 GPa.

For experimentalists, the use of pressure is a great asset, but also for theoreticians. From the theoretical point of view, it is easy to follow changes in electronic, dynamic and transport properties with the increase of pressure. On the other hand, elements such as antimony and arsenic, as well as compounds such as bismuth telluride and antimony telluride seem attractive to apply pressure tuning due to their anisotropic and layered nature. Additionally, Bi_2Te_3 stands as one of the best thermoelectric materials at room temperature as well as Sb_2Te_3 [2].

Hereafter, we show the pressure dependence on the thermoelectric properties of bismuth telluride. Our results are in very good agreement with those obtained by experiments at ambient conditions. Moreover, we found strong evidence that supports previous experimental results, for the existence of an electronic topological transition (ETT) in Bi_2Te_3 when the pressure reaches 2 GPa.

We start this chapter with the computational settings that we use for Bi_2Te_3, and for further calculations in $(GeTe)_x(Sb_2Te_3)_1$.

4.1   Computational details

For all our calculations, we use the Vienna Ab-Initio Simulation Package (VASP) that works in the framework of density functional theory (see chapter 2). We perform full relaxation of the crystal structure and atomic positions, with deviations from the the target pressures not higher than 0.2 GPa, and residual forces between atoms smaller than 2.0×10^{-5} eV/Å. We carefully look at the components of the stress tensor and not only to the values of the trace to assure hydrostatic relaxation. For Bi_2Te_3 under pressure, this step was essential to obtain the evolution of the electronic and thermoelectric properties with the increase of hydrostatic pressure. Continuing with bismuth telluride, we enforced that components of the stress tensor do not differ from the required pressure for more than 0.15 GPa. This requirement

was not fulfilled when we included van der Waals functionals since we got abnormally large c/a values. We discretize the Brillouin zone with a regular grid of $10 \times 10 \times 10$ k-points for the relaxation of the structure as well for the self-consistent field calculation (SCF). Afterwards, we increase this grid up to $20 \times 20 \times 20$ k-points for the non-SCF calculation, this for a better representation of the states in the vicinity of the bandgap. We used 300 eV for the planewave basis expansion, this allowed us a convergence in the energy of 1×10^{-7} eV for all the structures under pressure. In this work, we employed the projector augmented-wave method for the pseudopotentials with the PW91 generalized gradient approximation for the exchange-correlation energy [25]. We include semi-core d-orbitals in Bi within the fully relativistic scheme that allowed us to perform spin-orbit interaction calculations. For the thermoelectric properties, we worked with the BOLTZTRAP code (chapter 3) [10].

Table 4.1 summarizes the settings that we used in our calculations in tellurium based phase-change materials. For all the compositions and stacking configurations, we used PBEsol pseudopotentials within the fully-relativistic scheme and a cutoff energy of 400 eV. We do not include of semicore d-orbitals in these calculations. We performed two types of calculations, with and without spin-orbit interactions (SOC). The computational cost to perform calculations with the inclusion of SOC to obtain second- and third-order interatomic force constants (IFCs) prove to be extremely high and unnecessary. To compare, we perform calculations for phonons with the inclusion of SOC even though this was not required for further calculations of the thermal conductivity. We indeed realized that the heat capacity is independent of the inclusion of SOC. Therefore, we continued with our calculations of phonons and third-order IFCs without the inclusion of spin-orbit interactions. The mentioned second- and third-order IFCs were used to obtain the lattice contribution to the thermal conductivity in these compounds with the use of the ShengBTE code [11]. We take into account interactions up to the fourth neighbor in our calculations of the third-order interatomic force constants. However, the electronic structure depends strongly on the inclusion of SOC. For this reason, we perform calculations with spin-orbit interactions to obtain the Seebeck coefficient.

VASP settings				
Compound	k-grid	NSCF k-grid	2nd order	3rd order
GST124	$6 \times 6 \times 6$	$20 \times 20 \times 20$	$3 \times 3 \times 3$ (2^3)	$2 \times 2 \times 2$ (2^3)
GST225	$8 \times 8 \times 2$	$32 \times 32 \times 08$	$5 \times 5 \times 2$ (Γ)	$4 \times 4 \times 2$ (Γ)
GST326	$4 \times 4 \times 4$	$16 \times 16 \times 16$	$2 \times 2 \times 2$ (2^3)	—

Table 4.1: K-point grid for the SCF and NSCF calculations and the size of the supercell used for the calculation of the 2nd and 3rd-order IFCs. In parenthesis we show the k-grid used in the calculations of the forces for the real-supercell approach.

4.2 Crystal structure and electronic properties under pressure

Bismuth telluride is a well-known narrow-band-gap semiconductor [41, 42, 43, 44]. It has been widely studied over the past 30 years due to its outstanding thermoelectric properties at room temperature [1, 18, 45, 3]. As well as antimony, bismuth and arsenic, bismuth telluride possesses a layered nature with a combination of short and long bond lengths [2]. It has been claimed that the layered nature of Bi_2Te_3 together with the strong relativistic effect arising from the large atomic weight of bismuth [44] gives the remarkable thermoelectric properties [1, 3]. But it was not only the outstanding thermoelectric performance that originated the research on bismuth telluride. It has been found that with the application of pressure, anomalies in the bulk modulus arise together with a nonlinear behavior in the c/a ratio [46, 47]. It has been claimed that these peculiarities are related to an electronic topological transition [46]. Moreover, it has been found experimentally that the a pressure of 1 GPa is sufficient to increase the Seebeck coefficient[48], while the mentioned ETT occurs around 3 GPa. It is well known that most of the semiconductors become increasingly conducting with pressure, which leads to a reduction of S since metals have a smaller Seebeck coefficient than semiconductors or insulators (see chapter 1).

In the following, we study the evolution of the seebeck coefficient as a function of the hydrostatic pressure. We do not only address the changes in thermoelectric properties, but also in the electronic band structure. Our results give strong evidence for the existence of an ETT while the increase of the Seebeck coefficient remains rather limited. We assume that the discrepancy between our results and those obtained experimentally could be related to the experimental conditions, for example, to grain boundaries that can play an important role as a function of pressure.
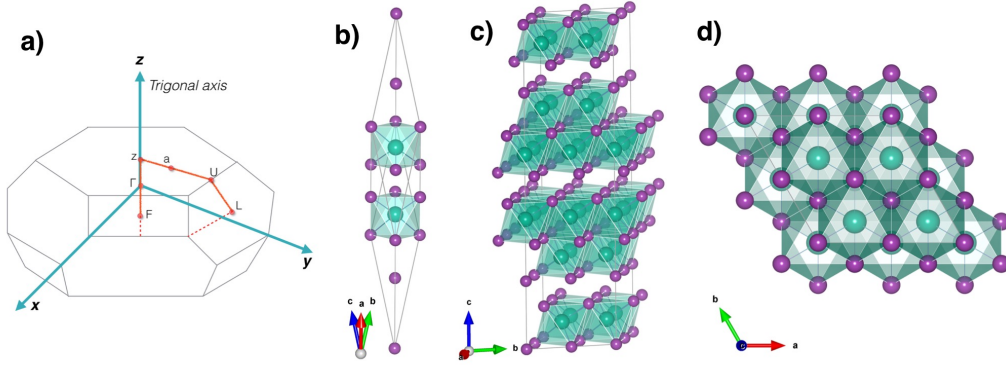
Figure 4.1: a) Brillouin zone of bismuth telluride. Red lines denote high-symmetry lines while red dots mark special points. b) Rhombohedral primitive representation of Bi$_2$Te$_3$. c) Non-primitive hexagonal representation which contains 3 formula units. d) View from the z-plane of the hexagonal representation.

For the relaxation of the cell with the applied pressure, we looked at the components of the stress tensor to assure hydrostatic pressure instead of just looking at the value of the trace. All details regarding to the settings in our calculations as well as convergence criteria can be found here above. As we mentioned, bismuth telluride possesses a layered atomic structure which can be easily identified in the non-primitive hexagonal representation of the space group #166 (R-3m). The primitive structure is rhombohedral with 5 atoms, while the hexagonal representation contains 3 formula units with atomic layers along the c-axis with sequence Te2-Bi-Te1-Bi-Te2- (See figure 4.1). In the non-primitive hexagonal representation, Te1 atoms are located in the (3a) Wyckoff position while Bi and Te2 occupy the (6c) position (Te1 in the (0 0 0) position and Bi and Te2 in the ($\pm$X $\pm$X $\pm$X) position in the rhombohedral representation, where $X_{Te} = \pm 0.21$ and $X_{Bi} = \pm 0.4$). The tellurium atoms in adjacent layers are bonded via long range forces, but, since we do not include such interactions in our calculations and we still get good agreement with respect to experimental data, even under the effect of pressure, we assume that these adjacent layers are partially bonded by covalent interactions. Our results of the lattice parameters at zero pressure agree very well with available experimental data of the system at ambient conditions. We obtain a lattice parameter value of 10.54 Å and a rhombohedral angle equal to 24.48 degrees. These values are 0.67 and 1.26 % larger than those
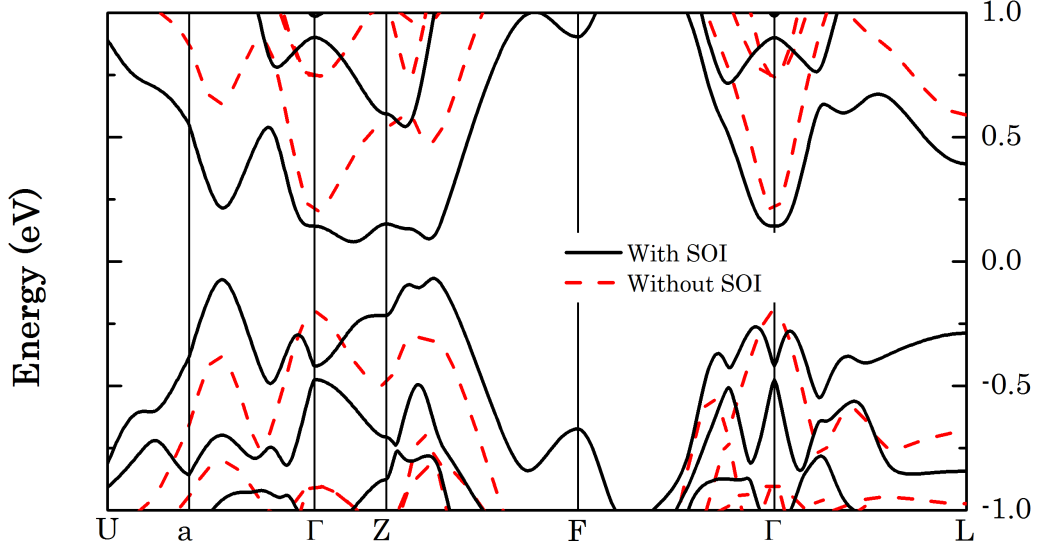
Figure 4.2: Full electronic band structure with (solid black) and without (red dashed) the inclusion of spin-orbit coupling.

reported experimentally [49]. For the internal fractional coordinates of the atoms, we obtained values as accurate as 1% compared with experiments (X$_{Te}$ = ±0.212 and X$_{Bi}$ = ±0.4 [50]). We expect the overestimation of the lattice parameters since we work with GGA exchange-correlation, and it is well known that GGA gives elongated crystal cells for this kind of layered structures.

Up to here, all the results shown have been calculated with the inclusion of spin-orbit interaction. In his work, Larson showed that the inclusion of relativistic effects, such as spin-orbit coupling, affects drastically the electronic properties of Bi$_2$Te$_3$ due to the large atomic mass of Bi [44]. Without the introduction of SOC, the bandgap is direct and is located incorrectly at the Γ point with a value of 388 meV. When SOC is taken into account, the gap becomes indirect with the bottom of the conduction band along the Z-F high symmetry line, while the top of the valence band is on the a-Γ line where "a" is not a high symmetry point (see figure 4.1). We obtain an energy gap of 76 meV, which agrees very well with the experimental value of Park et $al.$ (83meV, [51]), but differs from the value at room temperature (130 meV in Ref. [52]). In Ref. [51] the experimental lattice parameters are used and only the internal coordinates are relaxed, while we perform a full relaxation of the structure. Our calculations show that even at 5 GPa, not a single band crosses the Fermi level, therefore, even if pressure reduces the electronic gap,
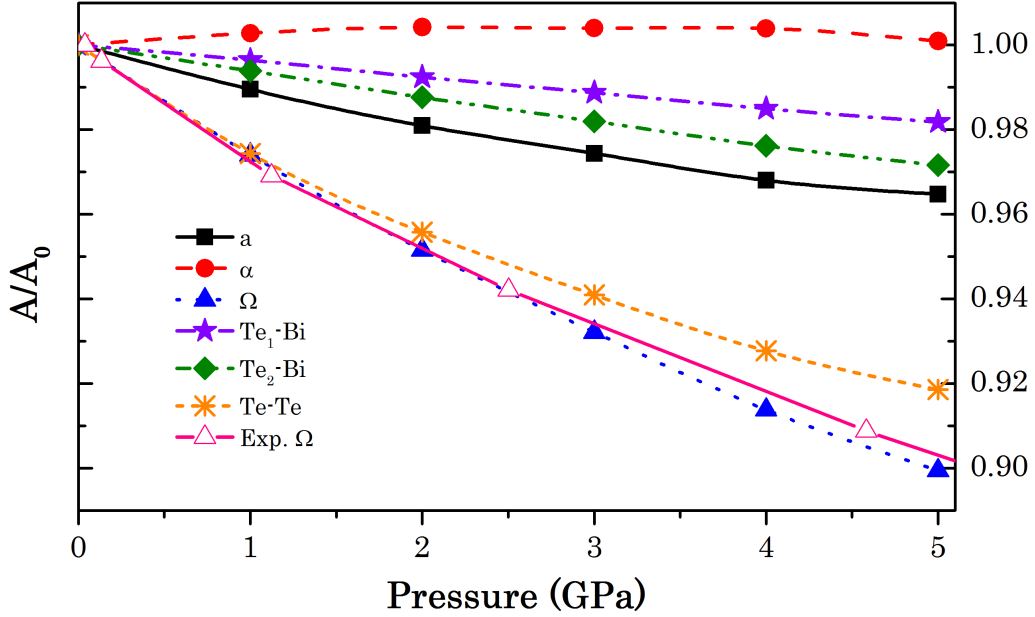
Figure 4.3: Normalized changes in the lattice parameter (a), lattice angle (α), primitive cell volume (Ω) and atomic bond length for Bi_2Te_3. Experimental volume was extracted from Ref.[46]

the system remains semimetallic. We obtain a pressure coefficient of -15 meV/GPa. This gives us non-zero gap at 5 GPa which agrees with experiments performed by Vilaplana *et al.* [53]. From resistivity measurements, Li *et al.* obtained a pressure coefficient of -19.73 meV/GPa [54] while Vilaplana reports a pressure coefficient of -6.4 meV/GPa for measurements of the optical gap. We compare our results related to the structural behavior of Bi_2Te_3 under the effects of hydrostatic pressure with those reported in the literature. Figure 4.3 shows our results of the evolution of the ratio A/A_0 (where A stands for the lattice parameter, the rhombohedral angle, the volume of the crystal, or the first interatomic distance and A_0 represents the same parameter at zero pressure). As expected, the Te-Te bond length decreases more rapidly than the Bi-Te bond length with the increase of pressure. In the xy plane, the structure tends to rearrange due to the enhanced proximity of the adjacent Te-Te layers which induces the increase of the rhombohedral angle. The decrease of the lattice volume with pressure agrees very well with experimental data. It is worth to mention that the Te-Te bond ratio decreases at a similar rate as the volume ratio. Based on the change of the energy under pressure, we extract the bulk modulus at zero pressure. Our theoretical bulk modulus agrees with -13.4% of the experimental value: the computed bulk modulus is 28.1 GPa while the experimental value is 32.5 GPa [46].
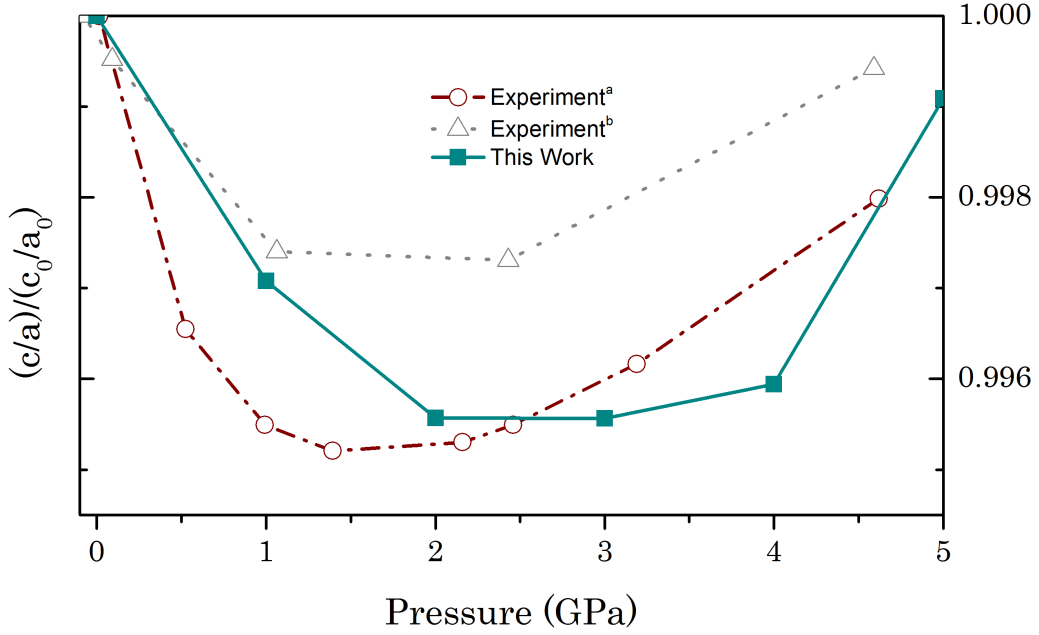
Figure 4.4: Normalized changes in the c/a ratio for the hexagonal representation of Bi$_2$Te$_3$. Experimental data were extracted from Refs. [47, 46] (empty circles and empty triangles, respectively)

For computational purposes, it is easier to work with Bi$_2$Te$_3$ in its primitive representation, nevertheless to compare with available experimental data, we plot the "c/a" ratio of the non-primitive hexagonal representation as a function of pressure. In experiment as well as in our theoretical calculations, both a and c parameters decrease. However the c/a ratio reaches a minimum at 1.5 GPa experimentally and around 2 GPa in our calculations. Polian *et al.* attributed this change in the pressure evolution of the c/a ratio together with the abrupt change in the Eulerian strains with respect to Birch-Murnaghan's equation of states (BM-EOS) to the onset of an electronic topological transition [46]. According to these authors, in the absence of transition, the dependence of the Eulerian strain with respect to BM-EOS is linear. In Bi$_2$Te$_3$, this linear dependence disappears around 3 GPa. Moreover, in Ref. [46], this abnormal behavior is only present in-plane an not out-of-plane.

In figure 4.5 we plot the electronic band structure of bismuth telluride under pressure. We chose the top of the valence band as reference (zero) energy in order to easily identify which bands evolve with P. Our calculations
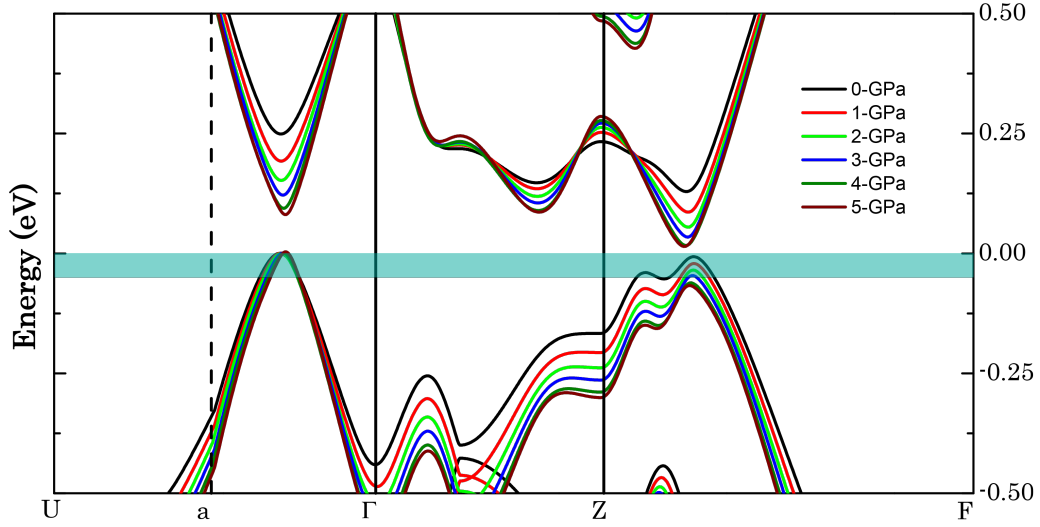
Figure 4.5: Electronic band structure of Bi$_2$Te$_3$ under pressure in steps of 1 GPa. The valence band maximum is taken as the reference energy, and the horizontal lines represent the limits of the electronic states contributing to the Fermi surfaces plotted in Fig. 4.6 (doping case 0 GPa).

show important changes in the electronic structure of bismuth telluride under pressure. The electronic bands change in a non-isotropic way, which deeply affects the topology of the electronic structure. At zero pressure, bismuth telluride exhibits two quasi-degenerate valence band maxima, one in the a-Γ line, and the other in the Z-F high symmetry line. The quasi-degeneracy is broken with the applied pressure because the peak in the Z-F line shifts to lower energies. This implies a real change in the electronic topology of the system which suggests the existence of the electronic topological transition.

To further investigate this phenomenon, we plot the Fermi surface of bismuth telluride for a given carrier concentration as a function of pressure. The result is shown in figure 4.6 and confirms that, at low values of carrier concentration, the electronic structure changes. The Fermi surface was obtained at zero temperature. We impose the hole carried concentration reported in experiments ($p = 1.8 \times 10^{18}$ cm^{-3}). As we mentioned before, the valence band has two quasi-degenerate, only 7 meV energy difference, maxima at zero pressure. This difference in energy increases to 21.5 meV at 1 GPa. This pronounced change in energy between the two maxima causes the disappearance of electronic states from the chosen energy window (the pockets that disappear at 1 GPa are encompassed by a red circle in figure 4.6). Up to now it is not clear if this reduction of available states will improve the
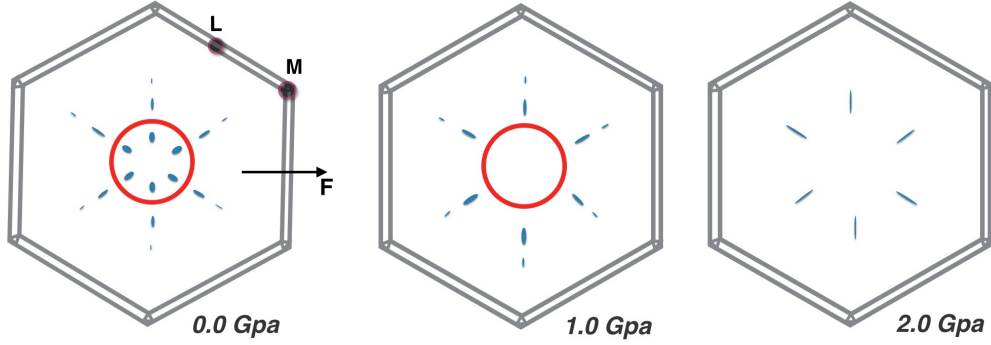
Figure 4.6: View of the (1 1 1) direction plane of the Brillouin zone. Small pockets represent available electronic states inside of the valence band. At 1 GPa, the top of the valence band leaves the selected energy window (see figure 4.5). Red circles encompass the electronic states that vanish with the ETT. The characteristic pockets at 1 GPa have merged at 2 GPa. The evolution of the Fermi surface above 2 GPa is not observable for the given energy window.

Seebeck coefficient because the system increases its metallic character which, in principle, should reduce the thermoelectric performance.

4.2.1 Thermoelectric properties at zero pressure

Henceforward, we show results concerning the thermoelectric properties of bismuth telluride. To start, we compare our results at zero pressure with those available in the literature. After a full relaxation of the crystal, we use the obtained electronic bands and the related density of states to calculate transport properties using the BOLTZTRAP code. The symmetry of the system, as we mentioned, gives anisotropic values of the transport properties. Hereafter we refer to the x-direction (symmetric with y-direction) as in-plane and to the z-direction as out-of-plane. The electronic DOS neglects this anisotropy and, in order to visualize it, we plot the so-called transport distribution function (TDF, see equation (3.20)) as a function of the chemical potential. Even though the two plots seem similar, small changes in the TDF result in large differences in the transport properties. In addition, the anisotropy of the system plays a crucial role with the increase of pressure as
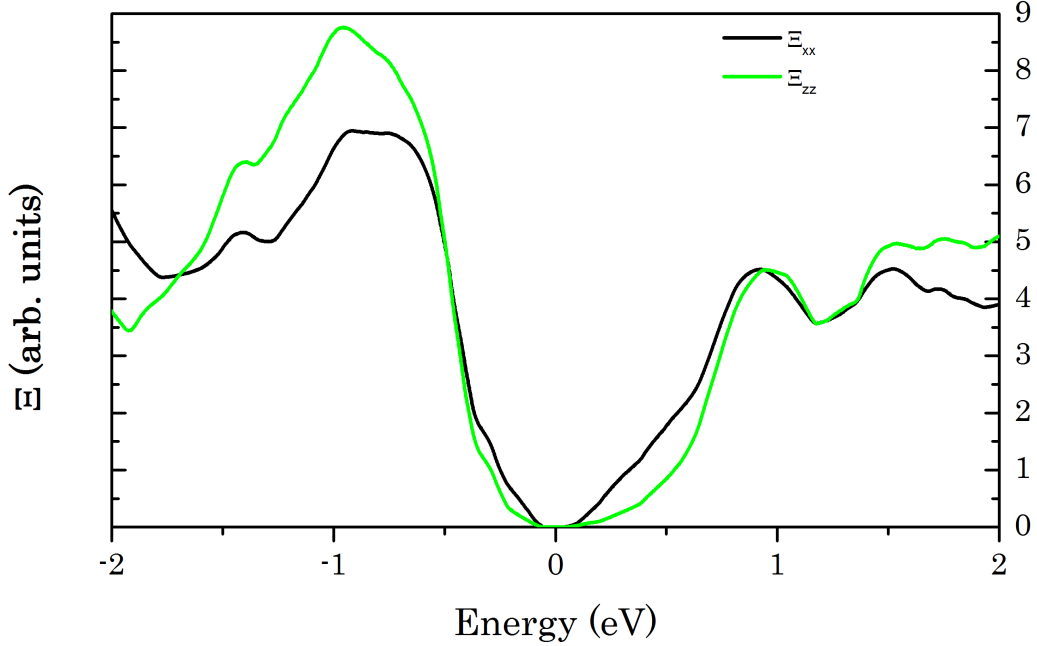
Figure 4.7: Transport distribution function for in-plane (xx) and out-of-plane (zz) of Bi$_2$Te$_3$ at zero pressure for different values of energy. Positive energies correspond to electrons and negative, to holes.

we will show hereafter.

Generally, the Seebeck coefficient depends strongly on the doping level [16]. In our case, the Seebeck coefficient ranges between ± 200 μV/K for doping levels ranging between $\pm 1 \times 10^{20} cm^{-3}$ at 300K. We imposed the carrier concentration to be equal to that reported in Ref. [51]. We compared our results of the temperature dependence of the Seebeck coefficient with those reported in the experiments. Since transport properties are related to states in the vicinity of the gap, we also include results of the Seebeck coefficient at experimental bandgap. As we mentioned, our DFT calculations underestimate the electronic gap. We thus use the scissors operator to increase the bandgap to experimental values. The scissors operator artificially opens the gap by a rigid shift of the conduction band to higher energies. Figure 4.8 shows that our results using data straight from DFT are in better agreement with experimental data than those obtained by the rigid shift of the electronic bands. At low temperature, the scissor correction is not needed and at high temperatures the gap is actually shrinking by thermal effects. This figure also shows the anisotropic nature of the Seebeck coefficient in Bi$_2$Te$_3$. Our calculations allow the independent study of the evolution of in-plane and

45
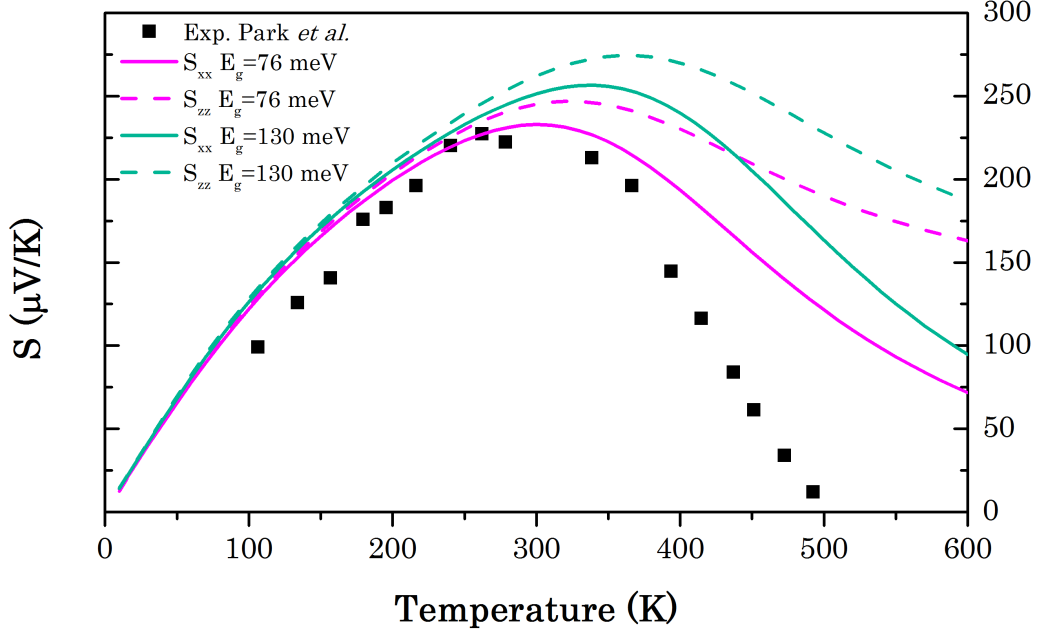
Figure 4.8: Temperature dependence of the in-plane and out-of-plane Seebeck coefficient for the original energy gap obtained by DFT and for a gap artificially increased using scissors operator for a doping level of p = 1.3×10^{19} cm^{-3}. Black squares are experimental data extracted from Ref. [51].

out-of-plane transport properties. These values turn out to be different above 250K. There is a correspondence between the chemical potential and the carrier concentration: in Bi$_2$Te$_3$, it is necessary to remove 2.3×10^{-3} electrons per primitive cell to reach a carrier concentration equal to 1.3×10^{19}cm^{-3}. The level in energy at which the total number of electrons is equal to 47.9977 (since our system contains 48 electrons) is equal to -80 meV. At the chosen carrier concentration, the change in the slope between in-plane and out-of-plane TDF is almost negligible. The effect of temperature is to move the chemical potential to a level where the differences in the TDF are considerable. This is also the reason why results with standard DFT and those obtained with the scissors operator are similar at low T. The operator keeps the bands unchanged and shifts the conduction band to higher energies which pushes the maximum of the Seebeck coefficient to higher temperatures. Now that we have checked that our results match nicely with the experimental data at room conditions, we continue by of applying hydrostatic pressure to the system and record the changes in the Seebeck coefficient.

4.2.2 Thermoelectric properties under pressure

In figure 4.9, we collect our results concerning to thermoelectric properties with pressure at 300K. Figure 4.9 shows in-plane (xx upper row) and out-of-plane (zz lower row) transport distribution function with respect to the chemical potential (a). On the other hand, the electrical conductivity (b) and the Seebeck coefficient (c) are plotted as a function of the carrier concentration. As we mentioned, the BOLTZTRAP code gives the electronic conductivity divided by the electronic relaxation time. We extract this relaxation time from experimental values of σ (69.93 × 10^3 Siemens/m) [49]. We divide the experimental electronic conductivity at room conditions by our value of σ/τ. The obtained relaxation time is equal to 1.0×10^{-14}s. As expected, the electrical conductivity increases with doping. However, the dependence of σ with the carrier concentration could differ from the observed linear dependence, since there is no proof that the electronic relaxation time varies linearly with doping. Nevertheless, our results show that the carriers move easier in-plane than they do out-of-plane. Since the layers of atoms are stacked in the z-direction, this result is reasonable as carriers should be able to move less freely across layers than inside them.

Now, concerning to the Seebeck coefficient, we have no evidence of any improvement of this property with pressure, at least not for hole doping (negative values of carrier concentration). However, we find the same behavior for S in- and out-of-plane, but it differs if the system is doped with holes or electron. When the system contains an excess of holes, the maximum of S constantly decreases with pressure independently of the direction, and this maximum shifts to higher concentrations. The constant reduction of the Seebeck coefficient agrees with the obtained results of metallization of bismuth telluride with pressure. Nevertheless, we explore the behavior under pressure at room temperature of the Seebeck coefficient, and we compare our results with those obtained experimentally. First, we compute S at 300K as a function of pressure using the experimental carrier concentration p = 1.2×10^{19}cm^{-3} [55]. In a recent experimental work, Ovsyannikov *et al.* do not report the carrier concentration, but the value of the Seebeck coefficient suggests a similar order of magnitude [48]. To compare with this last work, we used the carrier concentration that matches better with our results of S and those obtained experimentally at zero pressure. We assume that the experiment was performed at room temperature. The resulting carrier concentration is p = 1.8×10^{18}cm^{-3} which represents one order of magnitude of difference with the experimental carrier concentration obtained by Ovsyannikov and by Park. As it can be seen in figure 4.10, our results agree very
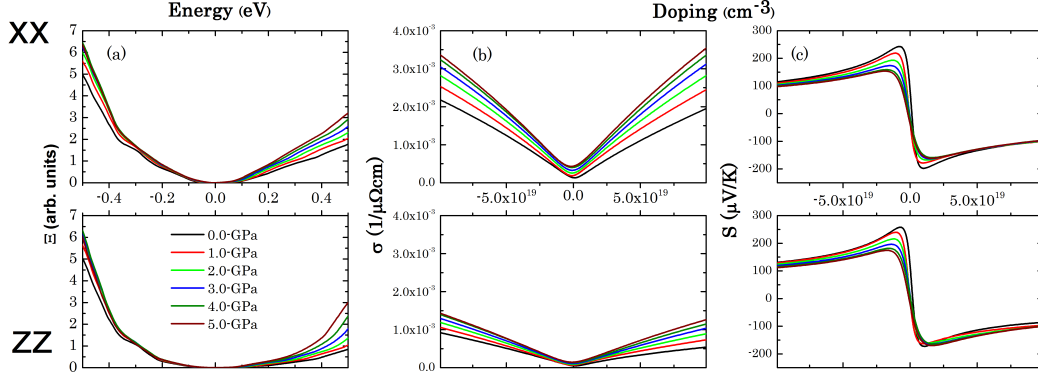
Figure 4.9: (a) the transport distribution function as function of the chemical potential, (b) the electronic conductivity computed with the BOLTZTRAP code and multiplied by the relaxation time $1.0 \times 10^{-14}s$ and (c) the seebeck coefficient. All the properties were obtained at 300K, (b) and (c) are plotted with respect to the carrier concentration where negative values denote p-type and positive values denote n-type. Top row represent in-plane results while bottom row represent out-of-plane.

well with the experimental reference. We expected a mismatch between our results and those with low carrier concentration, since the low doping means that the states involved are closer to the Fermi level, and our DFT calculations underestimate the bandgap. Even though the trend in the evolution of the Seebeck coefficient is correct, we do not observe the improvement of S at 1 GPa found by Ovsyannikov [55]. More interestingly, a shoulder appears at low carrier concentration. To explain this change in the trend, we will refer to our results about the electronic topological transition. At zero pressure, there are a certain number of available electronic states that form distinct pockets in reciprocal space (See figure 4.6). Upon pressure increase, some of those states vanish from the chosen energy window (the red circle encompasses the states in fig. 4.6 disappear). This causes the abrupt drop in the Seebeck coefficient at 1 GPa. When pressure reaches 2 GPa, the characteristic pockets merge and this produces the small improvement with respect to the value at 1 GPa. Above 2 GPa, the Fermi surface does not evolve further in the given energy window, and the metallization of the system produces a constant decay of the Seebeck coefficient. We should remark that in the work of Polian the effect of the ETT is only observed in-plane, whereas in our calculations both in-plane and out-of-plane transport properties are affected by the ETT. Moreover, our work shows that with the increase of the doping level the ETT disappears.
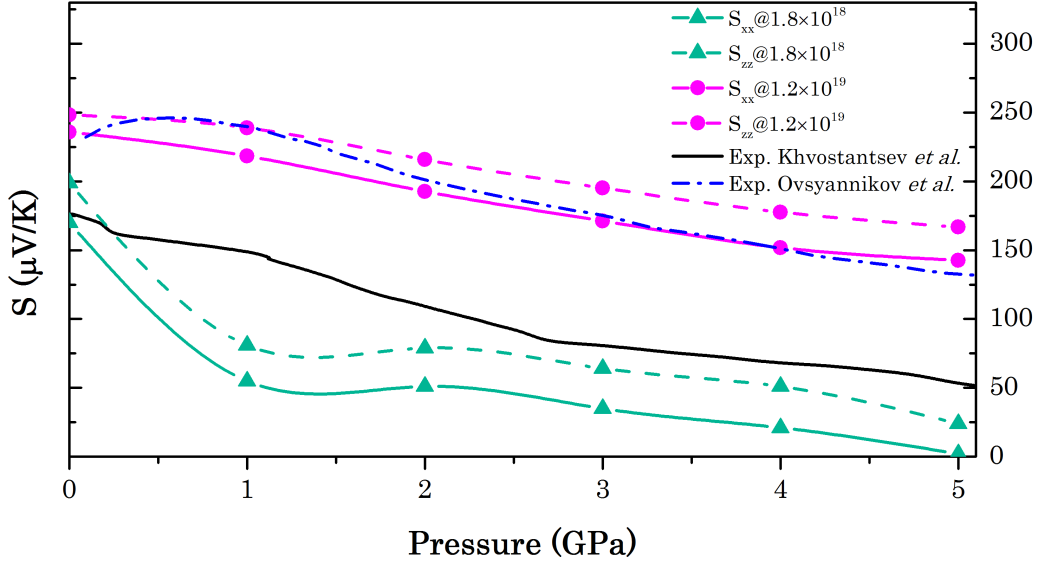
Figure 4.10: Pressure dependence of the in-plane (solid) and out-of-plane (dashed) Seebeck coefficient a 300K. Experimental data was extracted from references [55, 48].

4.3   Conclusions

In this chapter, we presented our ab-initio calculations of structural, electronic and thermoelectric properties of Bi$_2$Te$_3$ under pressure. We found that the increase of pressure induces metallicity in the system, however, the compound remains semiconductor even at 5 GPa in agreement with experimental data. The evolution of the Seebeck coefficient with pressure agrees with what has been reported experimentally. Nevertheless, the peak found in experiments at 1 GPa is not reproduced. When the system is doped with electrons, the Seebeck coefficient slightly improves with pressure, similarly to what was found for Sb$_2$Te$_3$ [56]. The similarities between our results and those obtained for antimony telluride suggest two things. First, the anisotropic evolution of the electronic bands that we describe here should be present in Sb$_2$Te$_3$. Second, the Seebeck coefficient in bismuth telluride should be enhanced by non-hydrostatic pressure. The behavior of the electronic topology in Sb$_2$Te$_3$ could be of high interest. This compound exhibits three quasi-degenerate maxima at the top of the valence band, instead of the two peaks that we report here for bismuth telluride.

We also found strong evidence of the ETT in bismuth telluride with pressure. We were able to reproduce the abnormal behavior of the c/a ratio re-

ported in experiments, which was claimed to be the experimental evidence for the mentioned ETT. We supported this conclusion by plotting the Fermi surface in which we showed that the applied pressure induces anisotropic changes in the electronic topology of Bi$_2$Te$_3$ at 2 GPa. We attributed this ETT to the non-linear band structure effects that occur when hydrostatic pressure is applied to an intrinsically anisotropic semiconductor such as Bi$_2$Te$_3$.

Chapter 5

Ternary compounds; $(\text{GeTe})_x(\text{Sb}_2\text{Te}_3)_1$

Phase Change Materials (PCMs) are considered for new generation of non-volatile memories due to their rapid and reversible transition between crystalline and amorphous phases [57]. These kinds of materials have been extensively studied due to their significant difference in the optical and transport properties between amorphous and (meta-) stable phases [58, 59]. PCMs exhibit unique properties that eventually could lead to further technological developments besides their application as data storage memory devices. For example, it is reasonable to consider PCMs as possible thermoelectric materials since they are based on tellurides [60] which is also the case for the most popular thermoelectric materials (see chapter 4). Also, phase change materials have relatively low thermal conductivities together with high and adjustable electronic conductivities.

In this chapter, we present our results concerning to crystal structure, electronic, dynamic and thermoelectric properties of three different quasi-binary compounds formed by GeTe and Sb_2Te_3. Table 4.1 summarizes the settings that we use for each of the studied compounds to perform the DFT calculation in the VASP code. For all our calculations related to pseudo-binary compounds, we approximate the exchange-correlation energy with the generalized gradient approximation within the Perdew-Burke-Ernzerhof scheme revised for solids (PBEsol). We use the projector augmented-wave (PAW) pseudopotentials which allows us to include spin-orbit interaction in the calculations. In these pseudopotentials, we do not include semi-core d-orbitals for the three elements involved. Lee and Jhi performed calculations with and without the inclusion of Te d-orbitals for the stable and meta-sable

crystalline structures in GST225 [61]. When the d-orbitals are included as part of the pseudopotential, the lattice parameters and the interatomic bond length increase by an average of 4 %. This behavior has been observed in other materials such as III-V and II-VI compounds [62, 63]. The authors found that even though the lattice parameters increase slightly with the inclusion of d-orbitals, characteristic features such as the splitting in the Ge-Te bond length in the Petrov configuration and the absence of it in the KH structure for GST225 are independent of the inclusion of the semi-core orbital. In agreement with the work of Lee and Jhi and in order to reduce the computational cost, we decided not to include the Te d-orbitals in any of our calculations.

5.1 $(\text{GeTe})_1$ $(\text{Sb}_2\text{Te}_3)_1$ (GST124)

The pseudo-binary compound $(\text{GeTe})_1(\text{Sb}_2\text{Te}_3)_1$ (GST124) is a well-known phase change material. GST124 possesses two (meta-)stable configurations. The meta-stable structure is a rock-salt-like cubic phase while the stable structure is rhombohedral. According to Matsunaga and Yamada [64], the transition between the meta-stable rock-salt structure and the stable rhombohedral structure in GST124 is due to vacancy diffusion. In this work, we focus on the stable configuration, which is rhombohedral. Even though it is well known that the stable configuration of GST124 belongs space group #166 (R-3m), there is a debate about the specific arrangement of the atoms in this configuration. Matsunaga and Yamada suggested, based on their x-ray diffraction measurements, that the stacking of the atoms in the non-primitive hexagonal representation is similar to that in PbBi_2Se_4. In that structure, tellurium atoms occupy the 6(c) sites while germanium and antimony atoms randomly occupy the 3(a) site with ratio 1:1 and the remaining 6(c) position with a ratio 1:3. This means that the layer corresponding to the 3(a) Wyckoff position contains the same number of Ge and Sb atoms while the layer labeled as 6(c) contains 3 atoms of Sb for one Ge atom [64]. On the other hand, Agaev *et al.* proposed a different atomic arrangement. They suggested that the crystal structure of GST124 contains not only Te-Te adjacent layers, but also Sb-Sb bonds. The stacking configuration proposed in reference [65] for GST124 is: Ge-Te-Te-Sb-Sb-Te-Te-. The work carried by Matsunaga and Yamada also shows that the meta-stable rock-salt structure survives up to 500 K. Once the stable crystal structure has been achieved, it remains in the rhombohedral configuration for temperatures ranging from 90 K up to the melting point (973 K).

Lattice parameters			Exp.[64]		Exp.[66]	
a		13.69	14.11		13.75	
α		17.84	17.41		17.61	
Atomic positions						
	This work		**Experimental data [64]**			
Site	**Atom**	**u**	**u**	**Atom**	**g**	
3(a)	Ge	0	0	Ge/Sb	0.493/0.507	
6(c)	Te	0.133	0.133	Te	1	
6(c)	Te	0.292	0.290	Te	1	
6(c)	Sb	0.424	0.427	Ge/Sb	0.253/0.747	
Bond lengths			**Atomic angles**			
Ge-Te		2.959	Ge-Te-Ge		55.11	
Sb-Te		2.99 - 3.16	Sb-Te-Sb		54.83	
Te-Te		3.669				

Table 5.1: Parameters of the crystal structure of GST124. Lattice parameters and bond lenghts are in Å while angles are in degrees. The atomic position (u) referes to the position (u, u, u) in the primitive rhombohedral structure. The atoms in the positions 6(c) have a symmetric site at (1-u, 1-u, 1-u). The experimental parameter "g" is the percent of occupancy at such site.

Another early work carried by Kooi and De Hosson [66] argued that the atomic ordering proposed by Agaev for GST124 is erroneous as well as the stacking configuration proposed by Petrov *et al.* for GST225 [67]. They reported that the real crystal structure of GST124 has a stacking sequence with only Te-Te adjacent layers, these layers being surrounded by Sb atoms which gives the following stacking configuration: Ge-Te-Sb-Te-Te-Sb-Te- [66]. This last proposal is the most widely accepted since it contains the pseudo-binary structure where one chemical formula of Sb_2Te_3 is stacked upon one chemical formula of GeTe. More recently Da Silva and co-workers showed that the stacking configuration proposed by Kooi and De Hosson is the one with the lowest energy [68].

5.1.1 Electronic and dynamical properties

In this work, we perform calculations on the primitive rhombohedral cell which contains seven atoms with the stacking configuration proposed by Kooi and De Hosson [66]. We find that under this configuration the system is semiconductor. Our relaxed structure agrees very well with the avail-
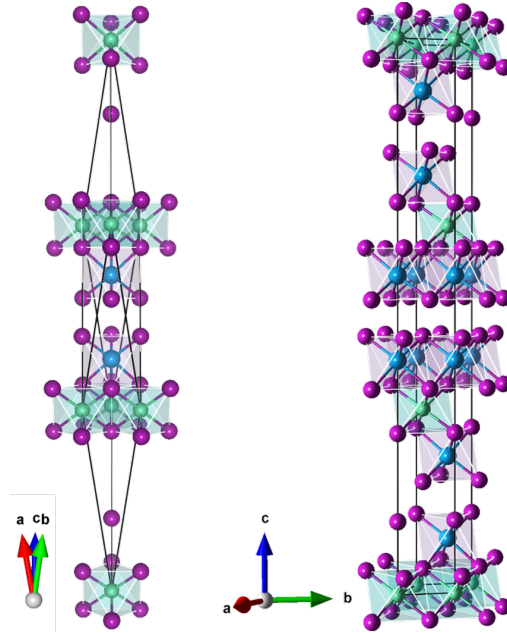
Figure 5.1: Left) Primitive rhombohedral representation of GST124. Right) Non-primitive hexagonal representation which contains 3 formula units. Green, blue and purple balls represent Ge, Sb and Te atoms, respectivelly.

able experimental data. Our results concerning the thermoelectric properties of GST124 overestimates the values of the Seebeck coefficient found in the literature, but within a small margin, while the lattice contribution to the thermal conductivity agrees well with available data.

The primitive rhombohedral and the conventional hexagonal representations of the stable structure of GST124 are shown in the figure 5.1. The atoms are stacked along the c-axis in the hexagonal cell. Our obtained rhombohedral lattice parameter is 13.6873 Å while the rhombohedral angle is 17.83 degrees. These values are in good agreement with the experimental data reported by Kooi and De Hosson (13.885 Å and 17.6 degrees, respectively) [66]. Our calculation underestimates the crystal cell length by -1.42 % while the lattice angle is overestimated by 1.3%. We measure the atomic bond lengths and we compare them with those in the literature for GST225 [69] since, as far as we know, this data is not available for GST124. The Te-Te interlayer distance reported for GST225 is 2.13 % larger than our value (here 3.67 Å for 3.75 Å experimentally). The Ge-Te bond length obtained is 2.96 Å, which is in the range of values that encompass experimental data for GST225 (between 2.89 and 3.19 Å). Finally, the large spread in the Sb-Te
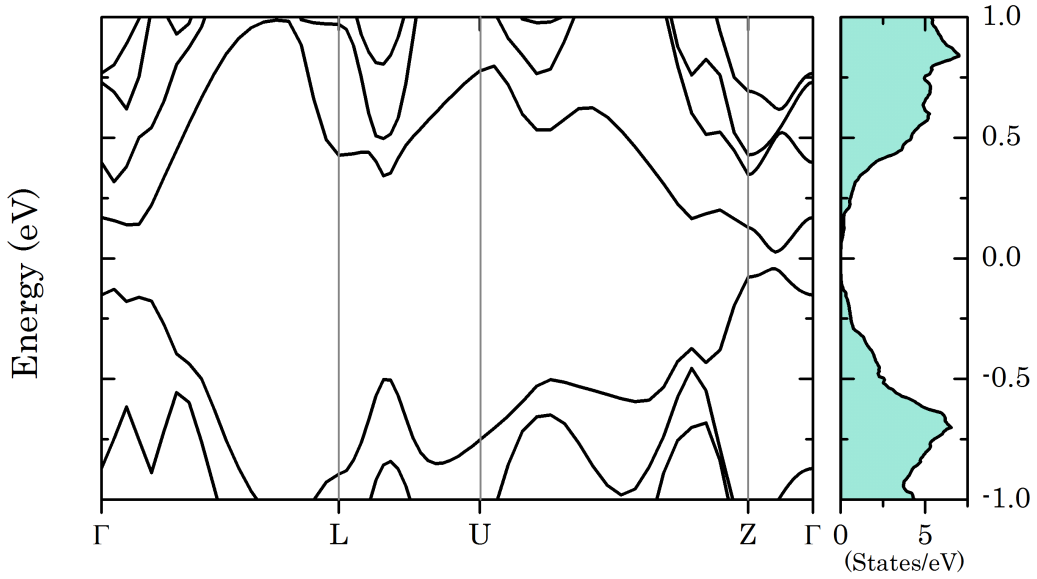
Figure 5.2: The calculated electronic band structure and the corresponding electronic density of states for GST124. The high symmetry points are similar to those showed in the figure 4.1.

bond length reported experimentally is observed in our results. We obtain two lengths for the atomic bonds with a difference of 0.17 Å (2.99 to 3.16 Å), while experimentally the spread is 0.3 Å with lengths from 2.89 to 3.19 Å.

Figure 5.2 shows the electronic bands through high symmetry points and the related density of states. The space group of GST124 is the same as for Bi_2Te_3, therefore, the Brillouin zone is that of figure 4.1. The computed electronic band gap is 0.225 eV, which is almost the half of the experimental value reported by Park *et al.* (0.55 eV) [70]. According to our results, this band gap is direct and is positioned on the high symmetry line that connects the center of the Brillouin zone with the Z high symmetry point located at the top of the BZ (see figure 4.1). References [71] and [72] agree that the system is metallic, with an increase of the electrical resistivity with the enhancement of temperature. Our results concerning the electronic properties of GST124 reveal that the crystal structure has semiconductor character. This leads to the assumption that GST124 in the stable configuration as well as GST225, is a degenerate semiconductor. Here we refer as degenerate semiconductor a semiconductor with a well-defined electronic band gap but with metallic-like transport properties.
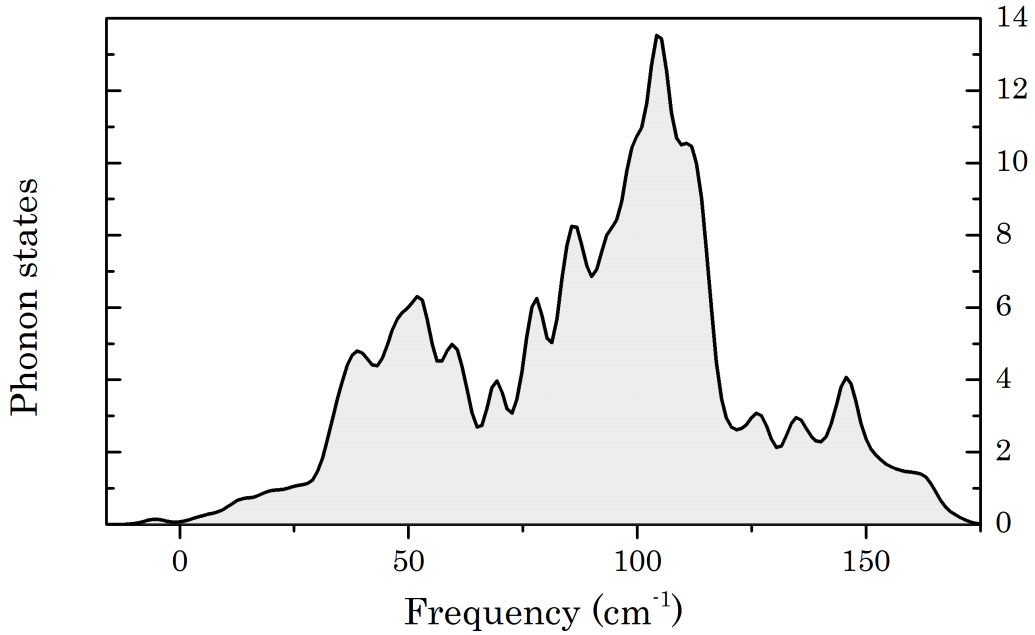
Figure 5.3: Phonon density of states for the stable configuration of GST124 obtained with a $3 \times 3 \times 3$ supercell using finite displacement method.

It is well known that DFT systematically underestimates the band gap. Nevertheless, as we show in the previous chapter for Bi_2Te_3, this does not affect significantly the Seebeck coefficient. On the other hand, the different curvatures between the valence and the conduction bands make that, at low values of carrier concentration and high temperature, the Seebeck coefficient could show the opposite sign depending of the nature of the carriers, i.e. positive values of S when electrons are the majority carriers. This behavior has been found by Thonhauser in Sb_2Te_3 under pressure [73, 74]. Nevertheless, this effect is only present when the system is doped with small values of electrons (10^{18} cm^{-3}) as we will show hereafter.

Regarding the dynamical stability of the system, we compute the second order IFCs with a regular grid of q-points of $3 \times 3 \times 3$. With those IFCs, we use the PHONOPY code [29] to plot the phonon density of states (figure 5.3). The small negative frequency in the figure arises from imperfection of the atoms relaxation (although the maximal residual force is less than 1.2×10^{-5} eV/Å). This phonon density of states is similar to that obtained for GST225 in the Kooi and De Hosson (KH) configuration, where the phonon states increase almost linearly up to 33 cm^{-1} and the maximum is reached around 100 cm^{-1}.

5.1.2   Thermoelectric properties

After we assure the dynamic stability of the structure, we proceed to compute the thermoelectric properties of GST124. In the literature, it has been found that GST124 could be doped with both types of carriers. For this reason, we plot the doping dependence of the Seebeck coefficient at 3 different temperatures (see figure 5.4). There are experimental reports that claim that the carrier concentration for the stable configuration of GST124 is around 2×10^{20} cm^{-3}. In a recent work, Siegrist and co-workers explain the changes in phase as a function of the annealing temperature [75]. They measure the electrical resistivity of GST124 where, from the amorphous phase to the stable crystalline phase, the electrical resistivity decays by 3 orders of magnitude. The authors show that the annealing temperature at which the stable configuration is reached is around 530 K. Based on these results, Zhang *et al.* show that at 530 K a metal-to-insulator transition occurs due to the diffusion of the intrinsic vacancies [76]. On the other hand, Shelimova and co-workers in their extensive work on layered compounds, agree that the carrier concentration on the stable crystal structure of GST124 is around 10^{20} cm^{-3}. Neither of the mentioned experimental papers explicitly refers to the type of carriers in the system (electrons or holes), but the Seebeck coefficient measurements in reference [71] indicate that the majority carriers are holes since the Seebeck coefficient is positive. As we have previously mentioned, metals have small Seebeck coefficients. Our results show that, in the range of carrier concentration reported in the mentioned experimental papers, the Seebeck coefficient is indeed small.

We plot the changes of the Seebeck coefficient with respect to doping not only for p-type of carriers, but also for n-type, even though in our knowledge, there is not experimental data that proves that GST124 can be doped with electrons. However, the theoretical paper of Sun *et al.* where the energy formation of different types of vacancies has been studied, suggests that GST124, contrary to GST225, can be doped with electrons [77]. Our results reveal that in the case when the system is a p-type semiconductor, an optimization of the Seebeck coefficient with the carrier density is needed. The value of S at room temperature can be at least five times larger if the carrier concentration is reduced from 2×10^{20} cm^{-3} to 5×10^{19} cm^{-3}. Nevertheless, it is better to keep a high value of hole doping if the objective is a thermoelectric material with the maximum thermoelectric performance at temperatures higher than room temperature.

There is not much improvement when the type of carriers is changed from
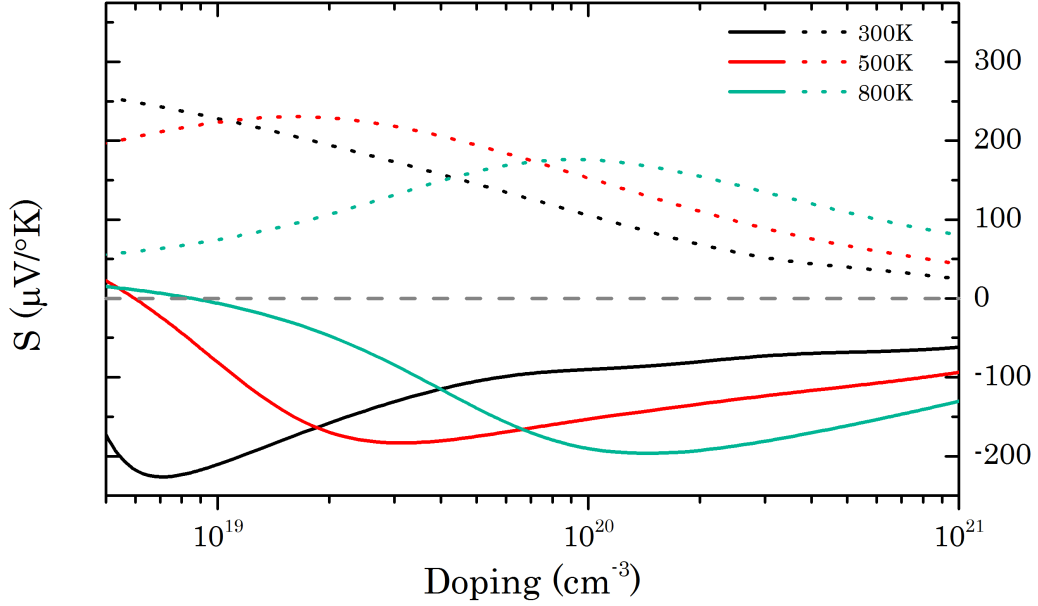
Figure 5.4: Doping dependence of the trace of Seebeck coefficient at three different temperatures. We explore the behavior when the system is doped with electrons (solid lines) and with holes (dashed lines).

holes to electrons. Our results also show that for low carrier concentration and high temperature, the Seebeck coefficient is positive even though the system has been doped with electrons. As we mention, this is due to the difference in the effective mass between the carriers in the top of the valence bands, and those in the bottom of the conduction band.

Based on the experimental reports of the carrier concentration, we fix the doping to plot the temperature dependence of the Seebeck coefficient, and we compare it with the available experimental data. Figure 5.5 shows our results for the in-plane (solid line) and out-of-plane (dashed line) Seebeck coefficient and its dependence with temperature together with experimental data [71, 78]. Our results overestimate experimental values. Nevertheless, we reproduce the overall trend with the increasing temperature. Also, our calculations do not show any maximum of the Seebeck coefficient even at 750 K in agreement with the experimental data. This could be important since the system could work as a thermoelectric generator, where the maximum thermoelectric performance is required at higher temperatures. The maximum value of S found experimentally is around 100 μV/K at 750 K. This value is almost the half of the peak reported for Bi_2Te_3 at 300 K. Again, the advantage is that the maximum is at 750 K instead of room temperature. We
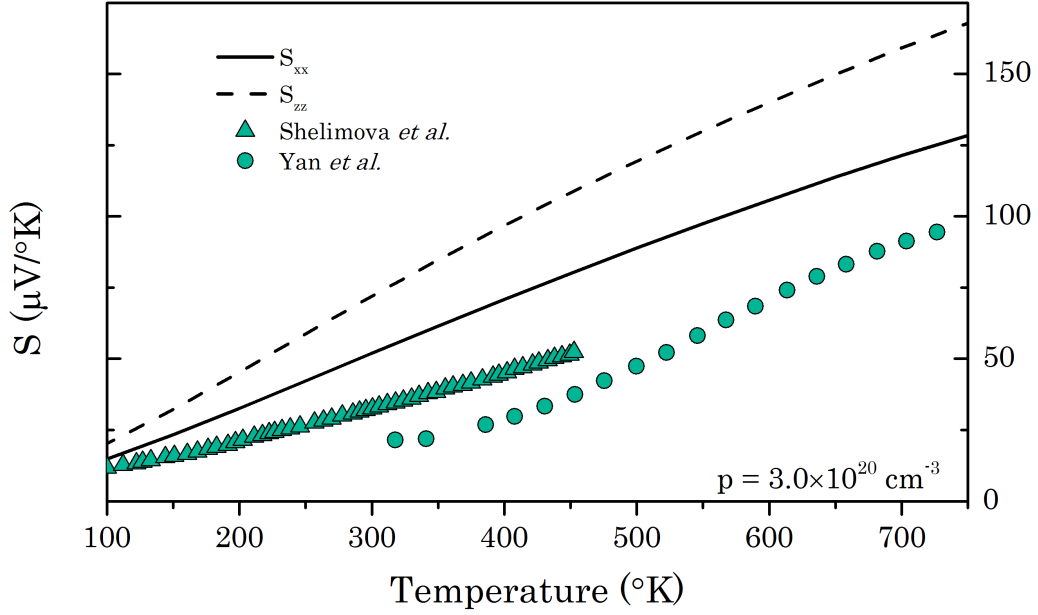
Figure 5.5: Temperature dependence of the in-plane (solid line) and out-of-plane (dashed line) Seebeck coefficient at fixed carrier concentration. The experimental data were extracted from Refs. [71, 78].

assume that the overestimation of our results could be due to experimental procedures, and the possibility to find different phases in the same sample [75]. One can note that the two experiments differ significantly in the 300 K - 450 K temperature range.

After obtaining the temperature dependence of the Seebeck coefficient, we proceed to computing another important thermoelectric property, which is the thermal conductivity. More precisely, we calculate the lattice contribution to the thermal conductivity. The agreement with the experiments in reference [79] is remarkable. Our average theoretical lattice thermal conductivity is only 30 % larger than that obtained experimentally using the Wiedemann-Franz law. The overestimation of the theoretical value was expected, since in the experiment, there could be many different minor scattering sources, i.e. impurities, defects, residual isotopic disorder, among others. Moreover, the limitations of DFT to predict lattice parameters and forces are well known [11]. Nevertheless, the obtained theoretical values are in very good agreement with experimental data.

Regarding the type of phonon scattering process, we find that the iterative solution for the BTE is 14 % larger than the relaxation-time approximation.
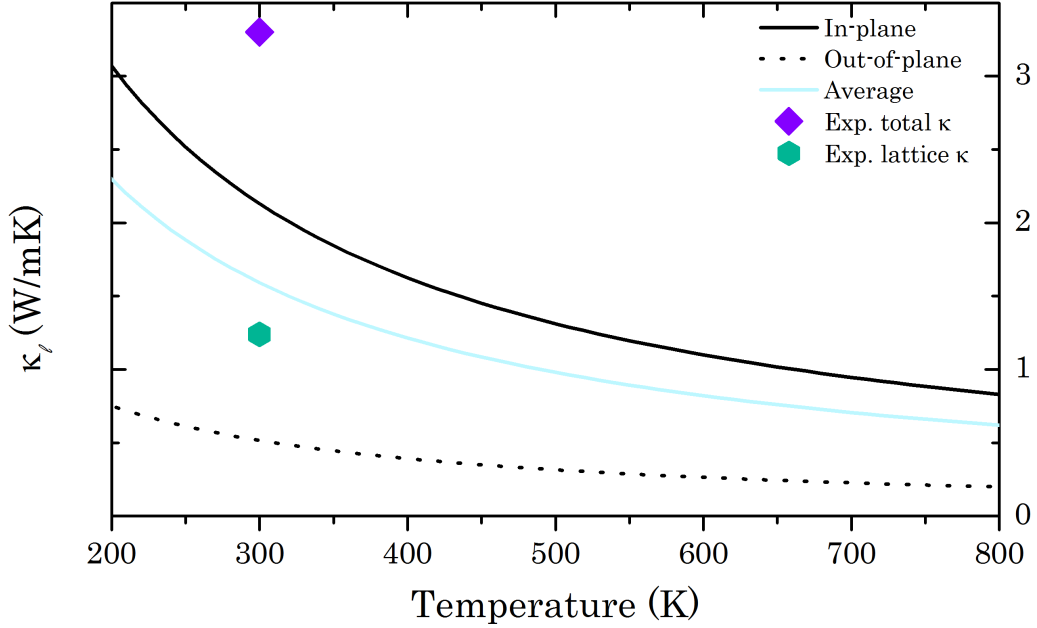
Figure 5.6: Temperature dependence of the components of the lattice contribution to the total thermal conductivity as well as the average of the trace of the thermal conductivity tensor and the experimental data. Experimental points were extracted from the work of Konstantinov *et al.* [79]. The lattice contribution to the thermal conductivity reported in experiments was obtained using the Wiedemann-Franz law.

This value is small but not negligible. Li *et al.* [11] report that for pure Si, the converged value of κ_l is just 4 % larger than the value obtained within RTA. This means that, even though in GST124 the phonon scattering is governed by Umklapp process, the contributions due to normal processes are significant. Our calculations allow us to explore individually the components of the tensor of the thermal conductivity. In this sense, we find that the normal processes are more significant in the in-plane component of the lattice thermal conductivity, since the relaxation time approximation gives 86 % of the converged value. While the Umklapp processes dominate almost completely in the out-of-plane component of the thermal conductivity.

5.2 The case of $(GeTe)_2(Sb_2Te_3)_1$: GST225

Among all the phase change materials, $Ge_2Sb_2Te_5$ (GST225) is the most promising PCM for non-volatile memory devices in terms of speed and stability [80]. As for GST124, GST225 exhibits two different phases at room

temperature. The meta-stable phase is cubic (rock-salt like) and the stable one is trigonal. The mentioned data storage process involves the reversible transition between amorphous and meta-stable crystalline phases. On the other hand, recent studies reveal that the stable trigonal structure of GST225 shows a topological-insulator behavior [57, 81].

5.2.1 Electronic and Dynamical Properties

The stable trigonal structure of GST225 belongs to space group #164 (P-3m1) with nine atoms per primitive cell. Layers of atoms are stacked along the c-axis. The stacking configuration of atomic layers remains unsettle. In an early work, Petrov and co-workers proposed the stacking sequence Te-Sb-Te-Ge-Te-Te-Ge-Te-Sb- [67]. Hereafter, we will refer this stacking configuration as Petrov. More recently (2002), Kooi and De Hosson proposed another stacking sequence which interchanges the Ge and Sb atoms in the Petrov configuration [66]. In that, the Te-Te adjacent layers are surrounded by antimony atoms instead of by germanium atoms (KH configuration). Together with these two proposed stacking configurations, recently, another has been proposed named as inverted-Petrov (i-Petrov) which consists of an interchange of adjacent Te and Ge atoms in the Petrov structure. This gives the following stacking configuration: Te-Sb-Te-Te-Ge-Ge-Te-Te-Sb-. The last stacking configuration includes Te-Te adjacent layers, as well as one Ge-Ge bond. We compute, by ab-initio means, the stability of these different stacking sequences, as well as their electronic and dynamical properties, together with the Seebeck coefficient and the lattice thermal conductivity, and compare our results with the available experimental data. We show that the KH configuration has the minimum energy; nevertheless this stacking sequence exhibits a mismatch for specific structural properties with respect to experimental data. Moreover, we find dynamic stability for the three proposed stacking configurations, and we demonstrate that just by changing the arrangement of the atoms in the structure, the material goes from semiconductor to metal. We also discuss previous theoretical results that claim that GST225 in the inverted-Petrov configuration exhibits Dirac-cone like band structure[2].

We perform full relaxation of the three proposed stacking configurations with and without spin-orbit interaction. We observe that the non-inclusion of SOC induces a small pressure in the system (close to 2.5 kbar) which means

---

[2]The Dirac-cones are responsible for many interesting properties in graphene, such as the high electron mobility and conductivity, since electrons behave as massless fermions whose transport can be treated as ballistic (perfect transmission).

	Stacking			
	KH	**Petrov**	**i-Petrov**	
Δ**E (meV/atom)**	0	15.92	19.13	
	Lattice parameters (Å)			**Ref. [69]**
a	4.23	4.2	4.16	4.22
c	16.88	17.14	17.59	17.24
	Bond length (Å)			
Ge-Te	2.95-2.97	2.81-3.17	2.8	2.89-3.19
Sb-Te	2.99-3.16	3.00-3.14	2.98-3.13	2.89-3.19
Te-Te	3.65	3.65	3.64	3.75
Ge-Ge			2.95	

Table 5.2: Lattice parameters and atomic bond lengths for the three proposed stacking configurations in GST225.

			Atomic positions GST225							
			KH		**Petrov**		**i-Petrov**		**Ref. [69]**	
Site	**x**	**y**	**z**	**Atom**	**z**	**Atom**	**z**	**Atom**	**z**	**Atom**
1(a)	0	0	0	Te1	0	Te1	0	Te1	0	Te1
2(d)	2/3	1/3	0.101	Ge	0.117	Sb	0.114	Sb	0.106	Ge/Sb
2(d)	1/3	2/3	0.199	Te2	0.219	Te2	0.214	Te2	0.207	Te2
2(d)	0	0	0.317	Sb	0.338	Ge	0.370	Te3	0.327	Sb/Ge
2(d)	2/3	1/3	0.420	Te3	0.421	Te3	0.451	Ge	0.417	Te3

Table 5.3: Atomic positions for the three proposed stacking configurations of GST225
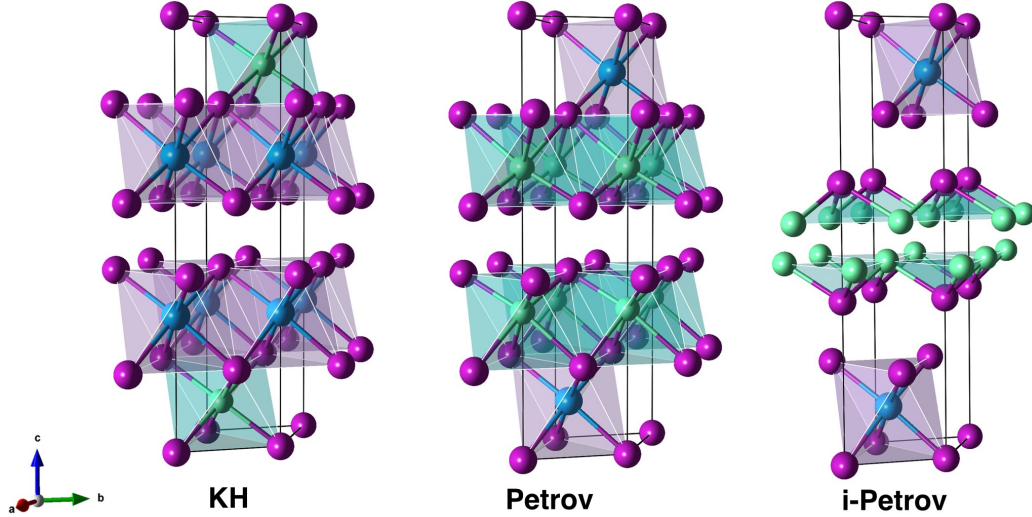
Figure 5.7: Primitive rhombohedral representation of GST225 for the Kooi and De Hosson (**left**), the Petrov (**center**) and the inverted-Petrov (**right**) stacking configurations. The color of the balls are the same as in figure 5.1.

that with SOC the cell expands. The expansion of the cell is not larger than 0.1 % in each direction (For the KH configuration the expansion was 0.046 % and 0.052 % for the a and c parameter, respectively). Nevertheless, the electronic topology changes significantly when the SOC is included. Figure 5.8 shows the electronic band structure with and without spin-orbit coupling for the KH stacking sequence. We observe that the SOC reduces the gap and change it from indirect to direct. In summary, the inclusion of spin-orbit coupling in this particular case does not affect much the lattice parameters, however, it strongly affects the electronic band structure.

Hereafter, we will refer to the results with spin-orbit interaction. We summarize in table 5.2 our results regarding structural properties of each of the three stacking configurations of GST225. We find that the three structures are very close in energy so that any of them could be present at room temperature. The theoretical lattice parameters of all three configurations agree very well with the available experimental data. The stacking sequence proposed by Kooi and De Hosson has the lowest energy; therefore this structure is the most stable. However, discrepancies between theoretical and experimental data arise when we look at the Ge-Te bond length. Experimentally it has been found a spread in this bond length of about 0.3 Å. This distortion
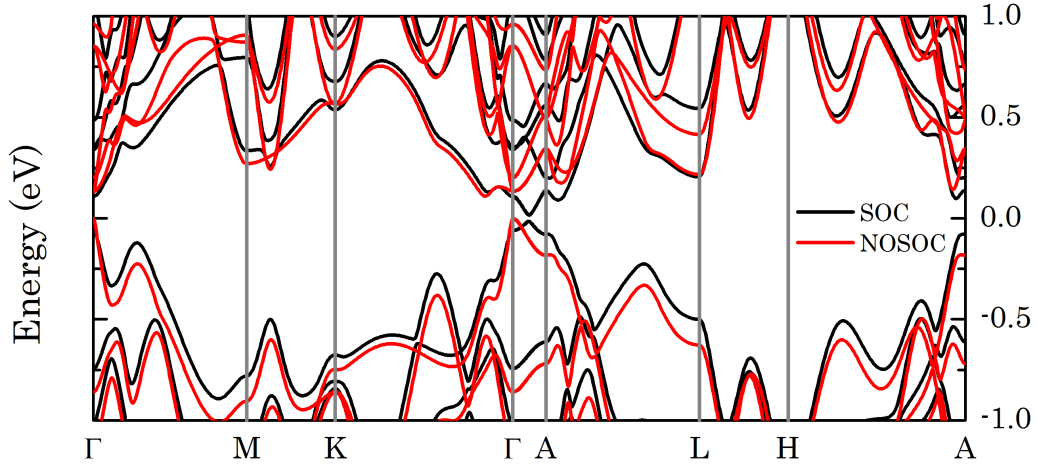
Figure 5.8: Electronic band structure of GST225 in the KH stacking sequence with (black) and without (red) the inclusion of spin-orbit coupling.

of the Ge-Te bond length is also present in the stable structure at room temperature of GeTe. This binary compound has a distorted rock-salt structure. The mentioned distortion occurs along the [1 1 1] direction in the rock-salt representation. The deformation of the cubic cell induces the formation of distorted octahedras in which the Te atoms are surrounded by three Ge atoms at a shorter distance (2.85 Å), and others three germanium atoms at a longer distance (3.15 Å). At the transition temperature of 716 K the rock-salt angle reaches the value of 60 degrees which corresponds to the perfect rock-salt structure [82, 83]. The distortion of the rock-salt structure is known as the Peierls distortion. The half filling of the p-orbitals in the system originates an opening in the bandgap, and also favors the creation of short and long bonds in three orthogonal directions [84]. This difference in the bond length is almost completely absent in the KH configuration, while the Petrov sequence indeed shows a difference of 0.38 Å in the Ge-Te bond length. Due to the nature of the stacking configuration named as inverted-Petrov, the structure does not show any spread at all. The atomic bond lengths were obtained by ab-initio means by Lee and Jhi with similar results to those that we show here (Ge-Te$_{KH}$ = 2.95 − 2.97 Å, Sb-Te$_{KH}$ = 2.93 − 3.07; Ge-Te$_{Petrov}$ = 2.78 − 3.13 Å, Sb-Te$_{Petrov}$ = 2.95 − 3.08 [61]). The authors relate these changes in the atomic bonds to the proximity of the Te-Te adjacent bilayer. In the Petrov configuration the Ge atoms are linked to tellurium atoms that belong to the above mentioned Te-Te bilayer. Therefore, it can be assumed that the interaction between the Ge atoms and those "pseudo-vacancies" situated between Te atoms in the mentioned layers is stronger than the interaction between

these "vacancies" and the Sb atoms in the KH configuration. This gives us a hint that the stacking configuration proposed by Petrov and co-workers could be the one present in the experiments. Other bond lengths such as Sb-Te and Te-Te agree with available experimental data. We do not take into account long-range interactions, nevertheless the Te-Te bond length is also in line with experimental data.

Figure 5.9 shows the electronic band structures of the three different stacking configurations. We find that two of the three different configurations show the metallic behavior, while the KH configuration is semiconductor. Experiments show that the stable structure of GST225 has a bandgap of about 0.5 eV while our theoretical gap is about 0.2 eV. On the other hand, the temperature dependence of the electrical conductivity suggests that GST225 is a metal. This is because the electronic conductivity decreases with the increase of temperature, which is the characteristic behavior of a metallic compound. Therefore, GST225 is a degenerate semiconductor. In their experimental work, Lee and co-workers [85] prove that the stable structure of GST225 has a high carrier concentration at low temperatures (5 K). The observed carrier density of 2.7×10^{20} cm^{-3} (close to the 0K), together with the measure of an optical band gap of 0.5 eV lead them to determine that the Fermi level in this compound must lies inside the valence band. They define this behavior as characteristic of a degenerate semiconductor.

From our band structure, we observe discrepancies with similar theoretical reports. There are in the literature three different papers that show results with respect to the electronic structure of GST225 in the KH stacking configuration. These three works used GGA approximation; two of the calculations were performed with PBE (Tominaga [86] and Sa [87]) while the last one does not specify the scheme type used in their pseudopotentials (Kim [57]). We also used the GGA approximation but with the PBEsol scheme. References [86], [87] and [57] show only the electronic structure in two different high symmetry lines while we explore almost all the first Brillouin zone. Due to the selection of the paths in which the electronic structure was observed, the three previous studies agree that the electronic gap of the KH configuration is direct and lies in the Γ point. We also find that the electronic gap is direct, but on the Γ-A high symmetry line. As we mentioned, the KH stacking sequence has a band gap of around 0.2 eV while in reference [86] the electronic band gap is slightly smaller.

Now with regard to the Petrov configuration, there are also differences between our work and those in the literature. However, as well as for the KH

structure, we think that it is just related to the choice of the xc functional which produces a shift of the electronic bands. Here, contrary to the three mentioned works, the structure is metallic with bands crossing the Fermi level at different points in the irreducible Brillouin zone.

The larger discrepancy between our work and those reported in the literature is concerning to the i-Petrov configuration. References [86] and [87] report the electronic structure of the i-Petrov stacking sequence with some differences between them. Sa and co-workers [87] report a direct band gap of 0.01 eV located at the Γ point, which differs from the work of Tominaga *et al.* [86] that claim the existence of a Dirac-cone like band structure. Both studies use PBE xc and they overestimate the c-parameter by 8.5 (Tominaga *et al.*) and 11% (Sa *et al.*) with respect to the reported experimental data. We show in our previous work that pressures as small as 2 GPa can induce electronic topological transition in anisotropic semiconductors such as Bi$_2$Te$_3$ [88]. We realize that the use of PBEsol corrects the large overestimation of the c-parameter in the i-Petrov stacking configuration since we obtain an accuracy of 2 % with respect to experimental data (see table 5.2). Our results show that the i-Petrov structure is metallic with the top of the valence band located in the A-L high symmetry line while the bottom of the conduction line is at the L point. The electronic band structure that we obtain using PBEsol with the crystal structure and atomic positions obtained from the relaxation using standard PBE were the same than those that we obtain with plain PBE, and similar to those reported in the literature [87, 86]. The strain induced when the exchange-correlation is changed from PBE to PBEsol is almost isotropic with a negative pressure of -22.2 kbar in-plane and -21.9 kbar out-of-plane. This negative pressure provokes a reduction of -0.05 Å and -1.53 Å for the length of the a and c parameters, respectively. With these calculations, we assure that the change in the electronic topology of the system is independent of the pseudopotential, and is related to the induced strain to the cell due to the choice of the exchange-correlation functional. The repulsion of the electronic bands with compressive strain has been reported in the work of Sa [87]. Even though they applied compression up to 4 % of the c-parameter length, the change in the electronic topology with the applied pressure is noticeable even at values as small as 2 % of the c-parameter length. Therefore, we believe that the Dirac-cone like band structure shown by Tominaga *et al.* relates to an electronic state present at some specific strain of the crystal cell. However, we recommend a full mapping of the first BZ since it is possible the bands crosses the Fermi level at points that differs from the the Γ point.
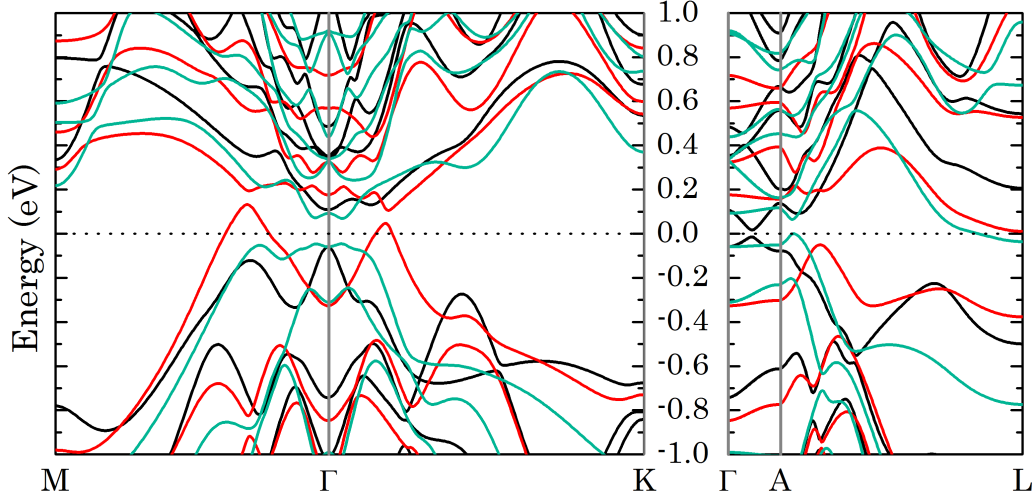
Figure 5.9: Electronic band structure along high symmetry lines for the proposed stacking configurations. Black, red and green curves denote the Kooi and De Hosson, the Petrov and the inverted-Petrov stacking configurations respectively.

The band structure provides information about the performance of the Seebeck coefficient. We expect larger values of S for the KH structure due to its semiconductor nature. This does not mean that this structure has better thermoelectric performance overall. Up to now we only have an insight of the electronic transport properties and we lack the dynamic contributions. We also need to compute the Seebeck coefficient as a function of the carrier concentration to ensure that KH structure indeed possesses the highest thermoelectric efficiency.

We mention that the agreement in the splitting of the Ge-Te bond length in Petrov configuration suggests that this could be the structure that it is present in the experiments. Sosso *et al.* have shown that indeed the KH structure is the one with the lowest energy [89]. They also show the absence of the Peierls distortion in the Ge-Te bond in this structure. They performed their calculations with PBE xc and computed the phonon frequencies at the Γ point for each of the two mentioned stacking configurations. The authors found an instability in the KH structure. They claimed that this negative frequency at the center of the Brillouin zone is so small (-9 cm^{-1}) that it could stabilize at room temperature [89]. Figure 5.10 displays the phonon density of states (PDOS) for the proposed stacking configurations[3]. We

---

[3]The phonon band structure for each of the three configurations is shown in the appendix
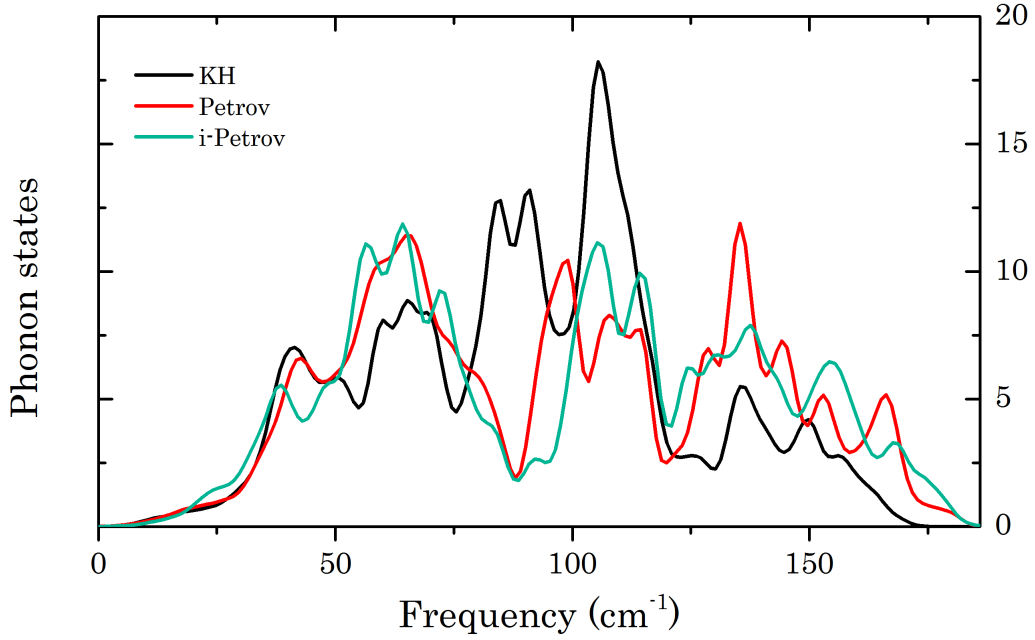
Figure 5.10: Phonon density of states for the three stacking configurations.

find that the three structures are dynamically stable (without a single negative frequency). We assume that the discrepancy between our results and those obtained by Sosso and *et al.* comes from the choice of the exchange-correlation functional; we chose to use PBEsol which improves the agreement on the lattice parameters with respect to experimental data. This result indicates the strong correlation between the lattice parameters and the phonon frequencies on GST225. While the inclusion of SOC changes the lattice parameters about 0.05 %, the use of PBEsol instead of PBE improves the usual overestimation produced by GGA as much as 2.4 %. The drop in the PDOS for the Petrov and i-Petrov stacking configurations is related to a quasi-bipartite phonon dispersion in these structures. The phonon band structure (see figure in the appendix) has two groups of frequency bands. The lower group has twelve branches while the other group contains the remained fifteen. This kind of bipartite vibrational structure has been reported for the quasi-laminar compound SnSe in the Pnma structure [90].

After we calculate and highlight differences in the electronic, dynamic and structural properties of the stacking configurations, we now move on to the thermoelectric properties.
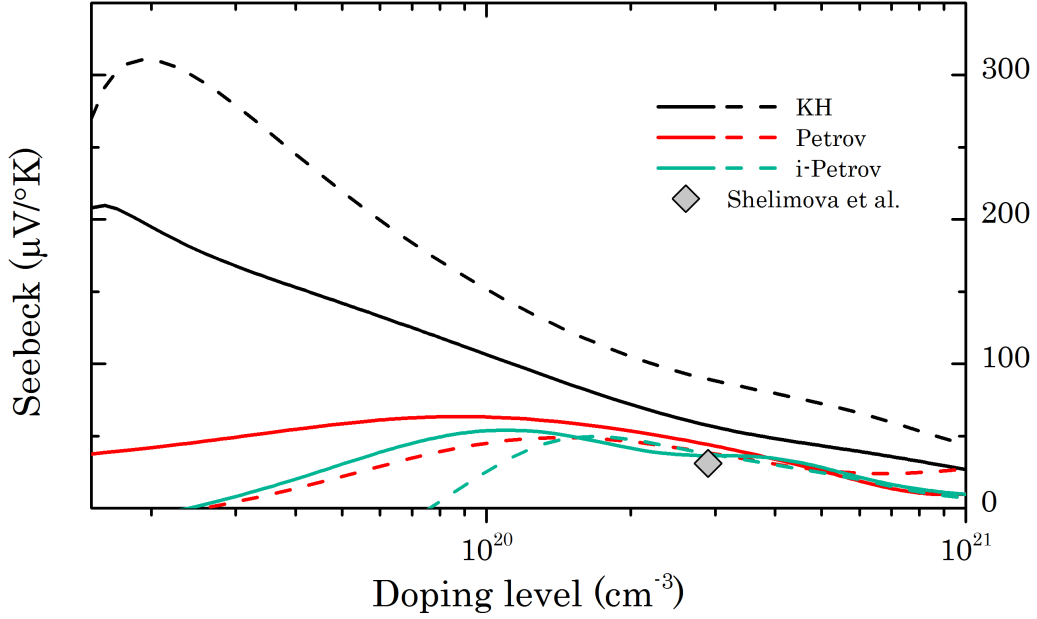
Figure 5.11: Carrier concentration dependence of the Seebeck coefficient at 300K. Solid and dashed lines denote in-plane and out-of-plane S. Experimental data was extracted from Ref. [71]

5.2.2 The Seebeck coefficient and Lattice Thermal Conductivity

The Seebeck coefficient is a property strongly related to the electronic topology of the system. Since the three configurations have different electronic structures we expect substantial differences in S. Two configurations show metallic behavior with bands crossing the Fermi level at different points in the Brillouin zone. The metallic nature certainly will lead to small relative values of the Seebeck coefficient. Furthermore, the dependence of the Seebeck coefficient with the electronic structure is linked to the carrier concentration. A recent theoretical work carried by Sun *et al.* shows that the lowest defect formation energy in GST225 is for the vacancy of Ge atoms (0.350 eV), which leads to a high concentration of vacancies that makes GST225 a permanent p-type semiconductor [77]. We perform calculations on the Seebeck coefficient as a function of the carrier concentration at 300 K for each stacking configuration. We only consider positive carriers in accordance to the work carried by Sun.

Figure 5.11 shows our results related to the Seebeck coefficient and its dependence with the carrier concentration. The strong link between S and
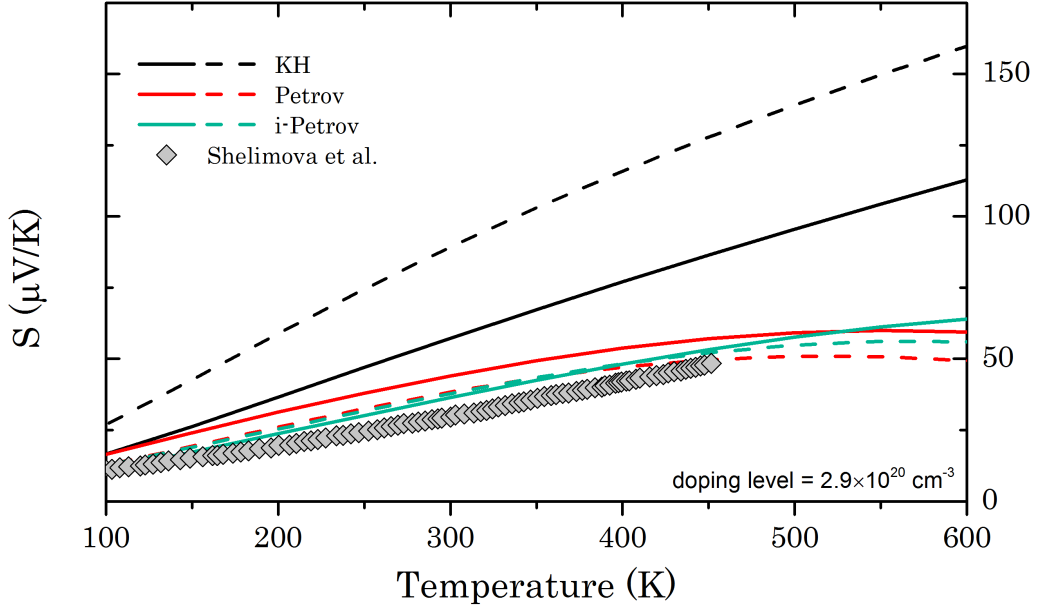
Figure 5.12: Temperature dependence of the in-plane (solid) and out-of-plane (dashed) Seebeck coefficient at experimental carrier concentration for the three proposed stacking configurations. Experimental data was extracted from Ref. [71].

the doping level is demostrated in the KH stacking sequence (semiconductor) where the values of the Seebeck coefficient vary from 300 μV/K at 2×10^{19} cm^{-3} down to nearly 25 μV/K at 1×10^{21} cm^{-3}. These values agree with characteristic values in semiconductors such as PbTe, Sb_2Te_3 and Bi_2Te_3 [27, 56, 10]. The other two structures with metallic electronic topology, as expected, exhibit considerably smaller values than those obtained for the KH configuration. However, both stacking configurations, Petrov and i-Petrov, are compatible with the available experimental data, with the value of KH being slightly larger than the experimental results. The figure also shows that the Seebeck coefficient could be optimized with respect to the carrier density. In the case of the KH structure the optimal value of doping is around 2×10^{19} cm^{-3}. With regard to the metallic-like structures the optimal carrier concentration is near to 1×10^{20} cm^{-3}. The optimal values of the carrier density could eventually, double the value of the Seebeck coefficient. Nevertheless, the experimental electronic gap suggests that GST225 could be suitable for a high temperature thermoelectric application. For this reason, we explore the temperature dependence of the Seebeck coefficient at fixed doping. We impose a carrier density equal to the experimental one reported by Shelimova (2.9×10^{20} cm^{-3}) [71].

Figure 5.12 shows the excellent agreement between our theoretical results and the data reported by Shelimova. The structures named as Petrov and i-Petrov are those with the better agreement with respect to experimental data. The structure with semiconductor behavior clearly overestimates the experimental results. Nevertheless, our results agree with experiments since the value of the Seebeck coefficient increases continuously with temperature. This confirms the hypothesis that GST225 would exhibit good thermoelectric performance above room temperature.

At high temperatures, the stability of the compound could be an issue since phase transitions could be present. Friedrich *et al.* [91] showed the rock-salt-like GST225 structure evolves from cubic to rhombohedral around 583 K together with an abrupt drop in the electrical resistivity. The work of Lyeo and *et al.* [92] mentions that once that the sample has been heated up to 673 K, and then cooled back to room temperature; the thermal conductivity remains almost unchanged. This behavior suggests that once the rhombohedral phase is achieved this phase remains intact after cooling. Moreover, reference [71] shows the temperature dependence of the electrical resistivity from 100 up to 800 K and there is no indication of phase transition. For all these reasons, we are confident that the experimental results show transport properties of the stable configuration of GST225.

Finally, we compute the lattice contribution to the thermal conductivity. Even though our calculations are not taking into account the electronic contribution to the thermal conductivity, the agreement with available experimental data is reasonable. Our results show that the KH structure has the lowest thermal conductivity. The same analysis that we did for GST124 applies for GST225. We realize that the contribution to κ_l that comes from normal processes is smaller than in GST124 ($KH_{xx} = 5.3\%$; $KH_{zz} = 0.7\%$ at 300 K). Our calculation does not only allow us to assess the contribution that comes from either normal or Umklapp processes, but it is also possible to observe the importance of each individual phonon branch to the lattice thermal conductivity. Calculations of κ usually avoid optical phonons due their small group velocities with frequencies that reside too high with respect to acoustic branches [93]. However, there are systems where the optical phonons provide important scattering channels to acoustic branches, like in diamond where 80% of the scattering processes involve acoustic and optical phonons [93]. Therefore, we explore the change in thermal conductivity when only the branches with frequencies below 90 cm^{-1} are taken into account for the Petrov and i-Petrov stacking configurations at 300 K (see figure 5.10). Our results show that these modes are responsible for the 74.6 % of the total

lattice contribution to the in-plane thermal conductivity, while out-of-plane these bands provide the 97.7 % of the total value in the i-Petrov configuration. Similarly, in the Petrov sequence the contribution of these bands reaches 81 % and 97.5 % of the total value of the lattice thermal conductivity for the in-plane and out-of-plane, respectively. The KH stacking configuration has an overall smaller lattice thermal conductivity and this structure lacks the phonon gap. On the other hand, the optical phonons in the KH sequence have lower frequencies than those in the other two configurations and, according with Carrete and co-workers [90], the large number of optical modes together with their low-frequency yields lower thermal conductivities. For the three configurations, the in-plane lattice thermal conductivity is higher than the out-of-plane counterpart. This is the expected behavior since the coupling (bonding) of atomic layers in the c-direction is weak. Also, the large value of the c-parameter, and the consequent reduction of the first BZ in this reciprocal direction leads to the reduction of κ_l due to purely geometrical considerations [90].
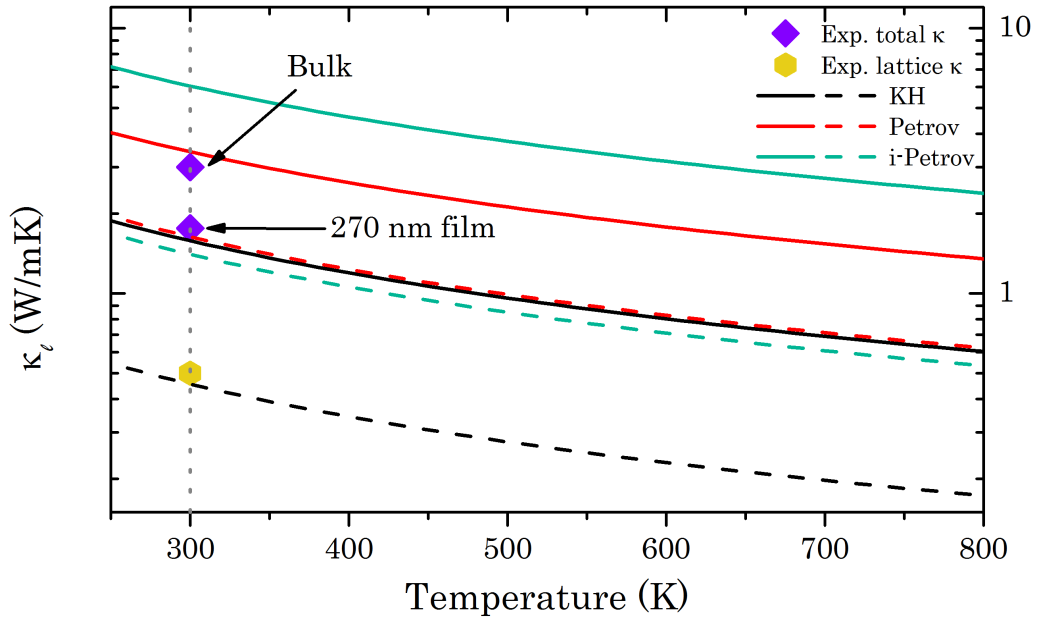

Figure 5.13: Lattice contribution to the total thermal conductivity for the three proposed stacking configurations. Solid and dashed lines represent in-plane and out-of-plane contributions, respectively. Experimental data was extracted from references [71] for bulk and [92] for film.

5.3 Electronic, Dynamic and thermoelectric properties of $(GeTe)_3(Sb_2Te_3)_1$

We further investigate the change of the thermoelectric properties of pseudo-binaries compounds by increasing the amount of GeTe in the system. We start with just one formula unit of GeTe, and we get remarkable agreement with experimental data concerning the lattice contribution to the thermal conductivity. Nevertheless, we clearly overestimate the Seebeck coefficient. When we studied the system with two formula units of GeTe (GST225), we investigate three different stacking configurations and realized that all of them were possible. Our results on GST225 reveal that the better agreement that we found in the Seebeck coefficient is for the stacking configuration with the metallic behavior, while the structure with semiconductor electronic configuration overestimates the experimental values of S. This fact leads us to think that another stacking sequence for GST124 could be stable while having a metallic character. This could yield a better agreement with experimental data even though, as well as for GST225, the stacking sequence with the lowest energy is the one with semiconductor behavior. In what follows, we present our work for a system with three GeTe formula units for one Sb_2Te_3 unit. In an early stage of our work, we realized that the generally accepted stacking configuration of GST326 was dynamically unstable. Therefore, we have changed the stacking sequence, and we found the arrangement of the atomic layers that yield the dynamic stability of the system. For this reason, we present our results for two different stacking sequences. The one with the lowest energy is the unstable one and the stacking sequence is as follows: Te-Ge-Te-Ge-Te-Sb-Te-Te-Sb-Te-Ge- (named as KH-326). This arrangement of the atomic layers was proposed by Kooi and De Hosson. Nevertheless, we find that the stacking configuration that leads to the dynamic stability of the system is given by Te-Ge-Te-Sb-Te-Ge-Te-Te-Ge-Te-Sb- (named as Petrov-326). Even though Baisheng and co-workers [94] show that the structure with the lowest energy is the one named as KH-326, the differences in energy between the KH and Petrov structures is only -7 meV/atom. This energy difference is even smaller than what we found in GST225 between KH and Petrov stacking configurations.

Similarly to what we did for GST124, we use the primitive cell which is rhombohedral with 11 atoms per cell. The small values of the forces between atoms that we obtained during the relaxation of the cell, together with the use of PBEsol xc gives us the confidence that the negative frequency that we have found is not related to an insufficient relaxation, or with a bad behavior
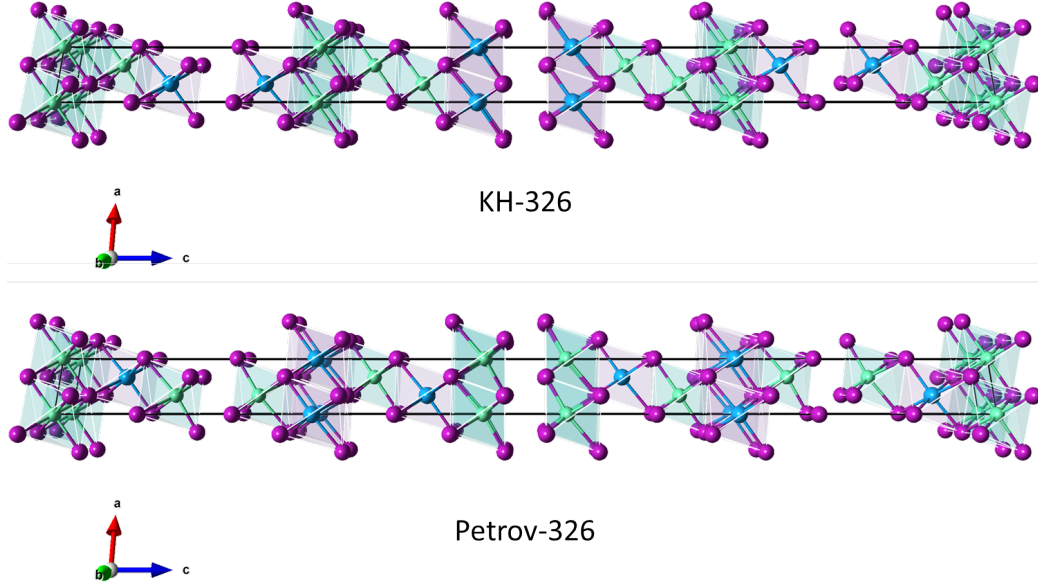
Figure 5.14: Non-primitive Hexagonal representantion of the KH-326 (**Top**) and the Petrov-326 (**Bottom**) stacking configurations.

of the PBEsol functional. The fact that our calculated lattice parameters and lattice angle agree with the available experimental data, reinforce our hypothesis that GST326 in the KH stacking configuration is dynamically unstable. We find that the lattice parameters are within as 2 % of the experimental data reported by Karpinsky and co-workers [95]. We summarize the lattice lengths, lattice angle and atomic positions in the tables 5.4 and 5.5.

The differences between the two proposed configurations are analogous to those in GST225 in the KH and Petrov stacking sequences. The electronic properties are similar also to what we get for GST225. When the Ge atoms are surrounding the Te-Te adjacent layers the system is metallic. On the other hand, when the Te-Te bond is surrounded by Sb atoms, the electronic character changes to semiconductor (figure 5.8). According to what we have obtained for GST225, we expect that the stacking configuration with semiconductor-like electronic structure will lead to a larger value of the Seebeck coefficient. According to the work of Rosenthal *et al.* [97], the range of values of the Seebeck coefficient for GST326 should be the same as those obtained for GST225.

	Stacking					
	KH-326	**Petrov-326**	**KH [94]**	**Petrov [94]**	**Ref.[95]**	**Ref.[96]**
E	-4.274	-4.267	-3.793	-3.781		
	Lattice parameters					
a	4.225	4.222	4.287	4.264	4.214	4.213
c	61.100	61.175	63.123	64.391	62.24	62.309
	Bond length					
Te-Te	3.754	3.632	4.058	4.008		
Sb-Te	2.97 - 3.18	2.98 - 3.16	3.12 - 3.29	3.02 - 3.20		
Ge-Te	2.93 - 2.99	2.80 - 3.20	2.99 - 3.03	2.82 - 3.32		

Table 5.4: Lattice parameters and atomic bond lengths for GST326. Energies are in eV while the lattice parameters and bond lengths are in Å.

	Atomic positions						
	KH-326		**Petrov-326**		**Ref.[96]**		
Site	**Z**	**Atom**	**Z**	**Atom**	**Z**	**Atom**	**g**
3(a)	0.000	Ge	0.000	Ge	0.000	Ge/Sb	0.77/0.23
6(c)	0.082	Te	0.088	Te	0.085	Te	1.00
6(c)	0.190	Te	0.187	Te	0.189	Te	1.00
6(c)	0.278	Ge	0.273	Sb	0.274	Ge/Sb	0.75/0.25
6(c)	0.361	Te	0.361	Te	0.361	Te	1.00
6(c)	0.449	Sb	0.455	Ge	0.451	Ge/Sb	0.36/0.64

Table 5.5: Atomic positions and occupancy factor (g) for the two proposed stacking configurations of GST326.
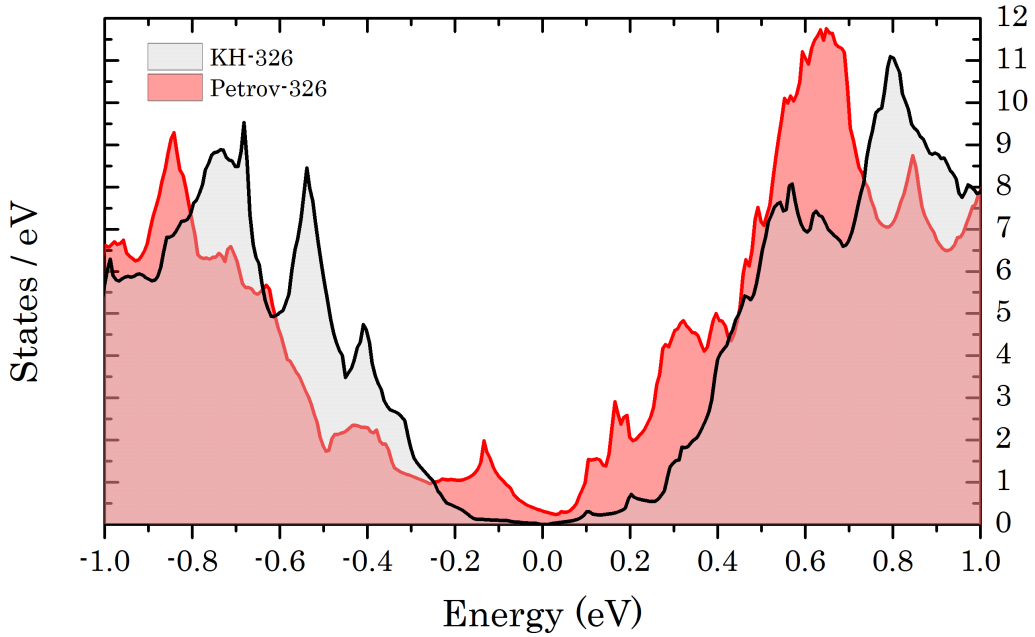
Figure 5.15: Electronic density of states of the two proposed stacking configurations.

As we mentioned, the main difference between our work and the one carried previously using DFT is that we perform phonon calculations, and realized that the stacking configuration denoted here as KH has negative modes at the Γ and A points (including the high symmetry line that goes between them). As far as we know, this is the first study of phonons in GST326, therefore, we lack comparison points.

Figure 5.16 show the phonon band structure of the two stacking configurations. It can be noticed that the negative value obtained is not as small as the one found in the work of Sosso *et al.* for the KH stacking configuration of GST225 [89]. Here the negative frequency reaches -40 cm^{-1} which clearly means that the system is unstable under this configuration. We find that this phonon mode is degenerate, and corresponds to the movement of the Ge and Sb atoms in phase along the x (or y) axis while all the Te atoms move out-of-phase in the same direction (lower panel in figure 5.16). This result is not what we expect since the instability is not arising from the movement of the atoms along the direction of the stacking of the layers. We expected that the negative frequency was originated by the Ge and Sb atoms trying to interchange positions, since our result in the Petrov-326 sequence reveal
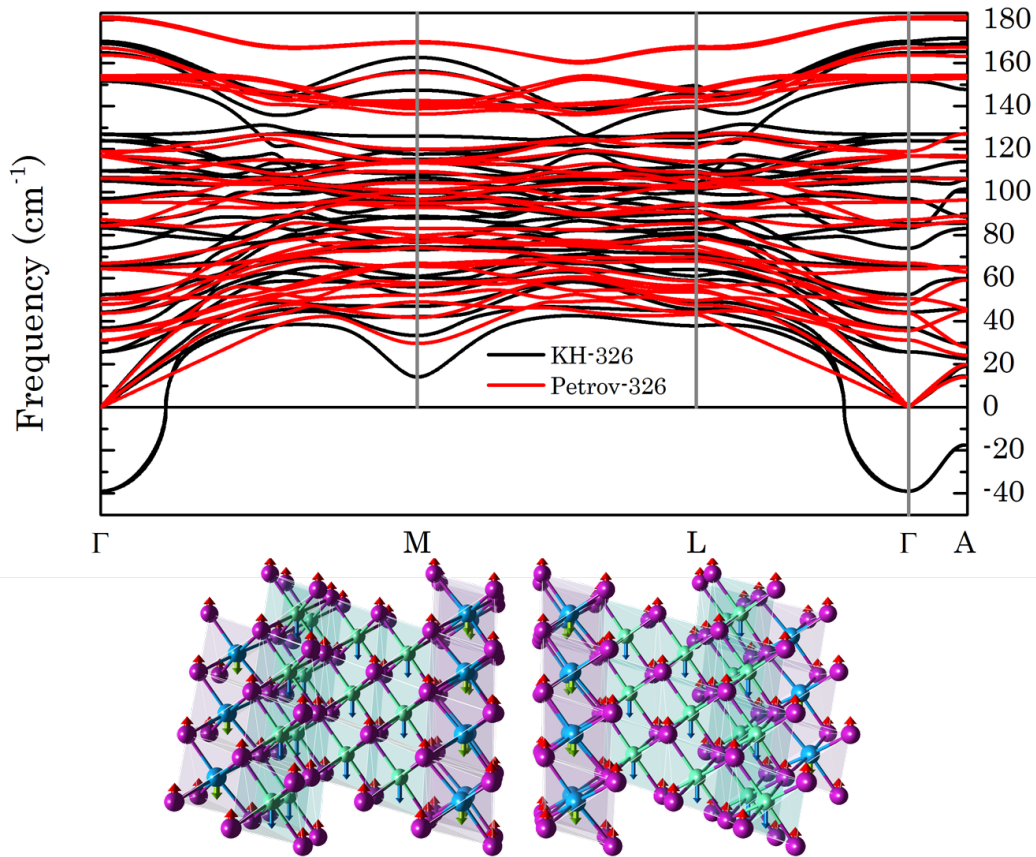
Figure 5.16: Phonon band structure for the two stacking sequences. The KH-326 configuration is clearly unstable. The lower panel shows the KH-326 structure with arrows that denote the movement of the atom that produces the negative frequencies.

that this configuration is stable, but this was not the case.

Despite that we demonstrate that the KH-326 is unstable, we will show in what follows our results concerning to the Seebeck coefficient for both stacking configurations, and compare with the available experimental data. We would like to remark that the comparison with experiments is more difficult for this compound than for the others. Since the crystal structure is larger and the intrinsic vacancies (those between the Te-Te adjacent layers) are more numerous, the compound becomes more susceptible to the growing method and the annealing temperature. For example, Sittner *et al.* measured the changes of the Seebeck coefficient with the temperature for the meta-stable structure of GST326 treated at two different annealing tempera-

tures [98]. They found that a difference of 50 degrees Celsius in the annealing temperature leads to 33 % difference in the value of the Seebeck coefficient. They argue that this behavior is due to the rearrangement of the intrinsic vacancies in GST326. With regard to the thermal conductivity, we were unable to compute it due to the large primitive cell, the high number of atoms in it and computational restrictions.

We start by plotting the doping dependence of the Seebeck coefficient at 300, 500 and 800 K. Since in the experiments the carrier concentration was not measured, we decide to adjust our carrier concentration to the one that makes the Seebeck coefficient agree with the experimental values. However, as can be seen in the figure 5.17, the difference between the two stacking configurations is huge. The values of the Seebeck coefficient for the Petrov-326 configuration are almost one third of those obtained for the KH-326. As we explained for GST225, the semiconductor character of the KH configuration leads to large values of S, but in the present case the differences in the Seebeck coefficient for the two configurations are much larger. We also find that for the KH-326 sequence, the peak in the Seebeck coefficient tends to oscillate (S=175 μV/K at 300 K; S=250 μV/K at 500 K; S=225 μV/K at 800 K), which differs from what we found in GST124 where the peak in the Seebeck coefficient shifts to higher carrier concentration and also decreases its value. We only plot the Seebeck coefficient for p-type of doping. We assume that the behavior of GST326 will be closer to GST225 where only p-type carriers are allowed.

Since the GST124 and GST225 have a carrier concentration around 3×10^{20} cm^{-3}, we decide to plot the temperature dependence of the Seebeck coefficient with the carrier concentration fixed at this value. Our results are shown in figure 5.18, and compared with the Seebeck coefficient measured by Rosenthal *et al.* [97]. The agreement with the experiment is, again, remarkable. However, the authors report this value of Seebeck coefficient for structures that were quenched from their cubic phase. We would like to remark that in this experimental paper there are no measures related to the carrier concentration. If we compare our result with the experimental work carried by Sittner and co-workers the agreement vanished [98]. The authors assure that the measures in their work are made on samples that have the stable crystal structure of GST326. But as we have already mentioned, it is really difficult to compare with them since the annealing temperature leads to abrupt changes in the Seebeck coefficient.
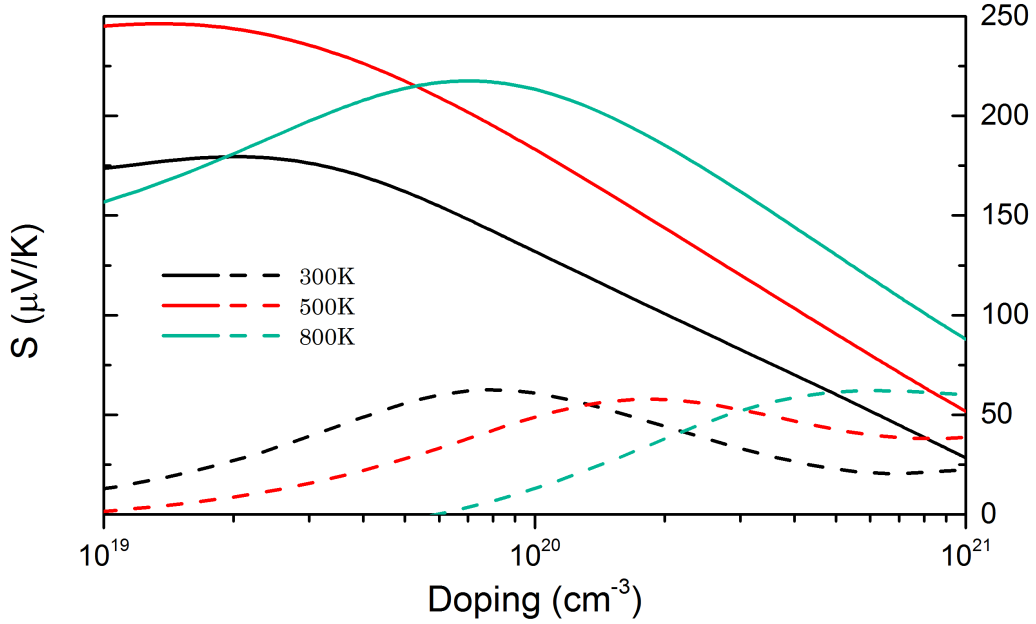
Figure 5.17: Carrier concentration dependence of the Seebeck coefficient for GST326. Solid and dashed lines denote values for the KH-326 and Petrov-326 stacking arrangement, respectively.

5.4 Conclusions

We explored the electronic, dynamic and thermoelectric properties of the pseudo-binary compounds $(GeTe)_x/(Sb_2Te_3)_1$ (x=1, 2, 3). For GST124, our study reveals that this semiconductor is dynamically stable under this configuration. Our values systematically overestimate the experimental results related to the temperature dependence of the Seebeck coefficient, however, we reproduce the overall trend. We also found that an optimization of S with the carrier concentration could lead to the increase of the thermoelectric performance. When the doping decreases from the experimental value of 3.0×10^{20} cm^{-3} down to 1.0×10^{20} cm^{-3}, the Seebeck coefficient duplicates its value at 300 K and, at 500 K, S is improved by 30 %. We also showed that there is no improvement in the Seebeck coefficient when the majority of carriers change from holes to electrons. On the other hand, the overestimation of the values of S with temperature together with our further results on the other pseudobinary compounds suggest that, it should be a stacking configuration with metallic character that will reduce the Seebeck coefficient very close to experimental values.

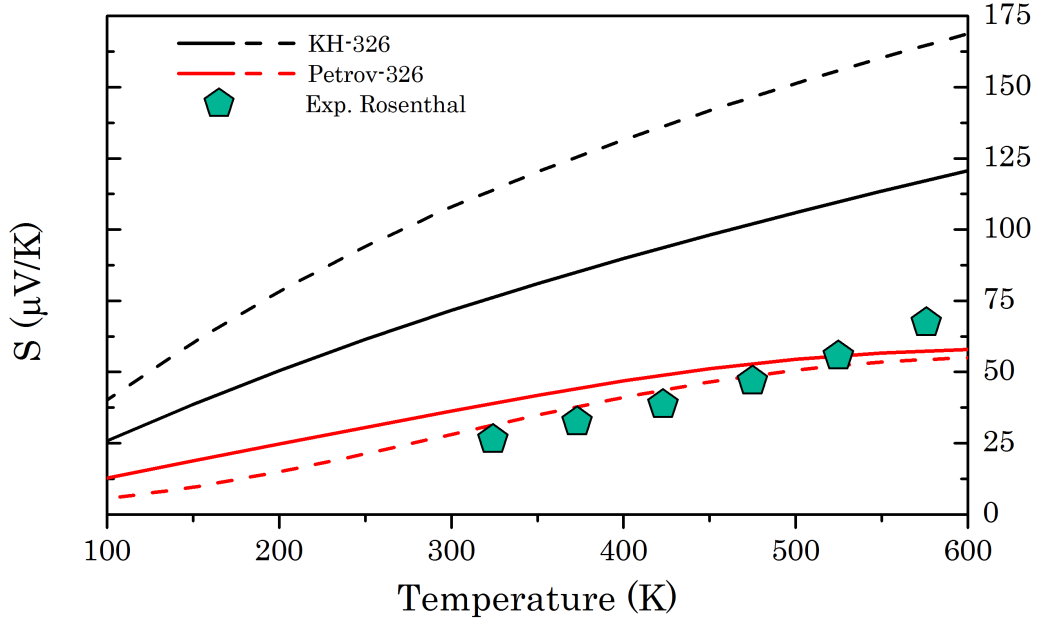Figure 5.18: Temperature dependence of the in-plane (solid lines) and out-of-plane (dashed lines) Seebeck coefficient for stacking configurations of GST326. The experimental data was extracted from the reference [97].

Regarding to the thermal conductivity, we showed that our results have a very good agreement with those in the literature at 300 K. The decrease of the lattice contribution to the thermal conductivity, together with the increase of the Seebeck coefficient suggests that the maximum thermoelectric performance (ZT) in this compound should be around 600 K. Our theoretical maximum is ZT=0.83 at 600 K (S=116.43 μV/K; k=0.82 W/mK; $\rho = 12 \times 10^{-6}\Omega$m [71]). However, our theoretical lattice contribution to the thermal conductivity is lower than the one obtained from experiments by the Wiedemann-Franz law (k=1.22). Also, our value for the Seebeck coefficient overestimates the experimental value (S=70 μV/K [78]) therefore, our theoretical thermoelectric figure of merit is much larger than the one that can be extracted from experimental results (ZT=0.20). However, we believe that it is worth to look at the optimization of S with the carrier concentration which could lead to values of ZT around 0.5.

Our results for GST225 exemplify the challenges faced for theoretical studies on phase-change materials. We explored three different stacking configurations of the pseudo-binary compound with x=2, and found that the sequence denoted as KH (Te-Ge-Te-Sb-Te-Te-Sb-Te-Ge-) is the one with the

lowest energy and is a semiconductor which agrees with previous theoretical results. We also reported the dynamic stability of the compound through our calculations of phonon modes. Our results on the thermoelectric properties of these materials show that the KH configuration has the best thermoelectric performance of the three proposed stacking sequences. The Seebeck coefficient, as well as for GST124, is overestimated with respect to the experimental data. As we mentioned, we assume that this is due to the semiconductor nature of this particular structure. An optimization of the Seebeck coefficient with respect to the carrier concentration is also needed for GST225. Even though, carrier densities as small as 2×10^{19} cm^{-3} could be hard to reach, S could double its value going from 3.0×10^{20} cm^{-3} to 1.0×10^{20} cm^{-3}. This structure also exhibits the lowest lattice thermal conductivity of the three configurations with values of κ that are in remarkable agreement with the experimental data.

The other two stacking configurations, named as Petrov (Te-Sb-Te-Ge-Te-Te-Ge-Te-Sb-) and inverted-Petrov (Te-Sb-Te-Te-Ge-Ge-Te-Te-Sb-), are metallic. Both structures show dynamic stability and their energy difference with respect to the KH configuration is not larger than 20 meV/atom. This small energy difference suggests that at room temperature the three proposed stacking configurations could coexist in the same sample. Our results for the i-Petrov structure exalt the importance of the volume of the crystal for the electronic topology. We performed calculations with PBEsol exchange-correlation with the aim to correct the systematic overestimation of the lattice parameters carried by standard PBE. We showed that the theoretical Dirac-cone in the band structure that has been recently reported by Tominaga and co-workers only exists under specific conditions of strain in the inverted-Petrov structure. With regard to the thermoelectric properties of the Petrov and i-Petrov structures, we achieved very good agreement with the experimental data for the temperature dependence of the Seebeck coefficient. Moreover, we showed that at the experimental carrier concentration, the in-plane and out-of-plane Seebeck coefficient for both configurations are quasi-degenerate, contrary to what we found in the KH stacking sequence. For the three proposed configurations, the out-of-plane lattice thermal conductivity is considerably smaller than the in-plane counterpart. This is the expected behavior due that the stacks of covalent layers are only loosely bonded along the c-axis, moreover, the reduction of the c* reciprocal length leads to the decrease of the thermal conductivity due to pure geometrical considerations.

On the other hand, the Petrov and i-Petrov structures have higher values

of κ than those in the KH configuration, even though both showed an abrupt drop in the phonon density of states around 80 cm^{-1}. This drop is a consequence of the quasi-bipartite phonon dispersion which is similar to what it was found in the Pnma structure of SnSe. As well as in SnSe, the lower set of phonon modes consists of twelve bands. However, the lack of a phonon gap suggests that the branches cross at some point in the BZ. We showed that this lower set of bands are responsible for at least 74 % of the total lattice thermal conductivity in-plane, while this percentage reaches 97 % for the out-of-plane contribution. Finally, our results show that the thermoelectric figure of merit reaches 1.35 at 600 K for the KH stacking sequence, again this is a purely theoretical value (except for the electrical resistivity that was extracted from the work of Shelimova and co-workers and is same than for GST124) where the Seebeck coefficient (128.45 μV/K) and the thermal conductivity (0.613 W/mK) are overestimated and underestimated, respectively. The structure with the ZT closer to the experimental value is the Petrov one with a figure of merit of 0.11 which represent the half of the value that can be extracted from experimental works (there are no experimental reports of the Seebeck coefficient at 600 K, therefore we extrapolate to a value of 75 μV/K). The i-Petrov stacking sequence has the poorest thermoelectric performance with ZT=0.08, this low value being due to the large thermal conductivity that we found even at 600 K ($\kappa = 2.33$ W/mK).

Finally, we explored the electronic properties and the Seebeck coefficient of GST326 (x=3). We realized that the most accepted stacking sequence of this pseudo-binary compound is unstable. Therefore, we performed the calculations on two different stacking configurations. The one with the negative modes at the Γ point is the so-called KH-326 (Te-Ge-Te-Ge-Te-Sb-Te-Te-Sb-Te-Ge-). The energy in this configuration is 7 meV smaller than the Petrov-326 configuration (Te-Ge-Te-Sb-Te-Ge-Te-Te-Ge-Te-Sb-). Similarly to what we found in GST225, the KH-326, and the Petrov-326 configuration have semiconductor and metallic character, respectively. With regard to the Seebeck coefficient and its dependence with doping, we found that, as well as in the previous cases, the value of S could increase with the reduction of the carrier concentration. However, we expect that the reduction of the doping will lead to a shift of the maximum Seebeck coefficient at lower temperatures in the Petrov-326 stacking sequence. In general, the trend in the temperature dependence of the Seebeck coefficient is the same as in GST225. The semiconductor structure clearly overestimates the experimental data, while the metallic structure agrees very well with it.

We suggest that phase-change materials such as those that we studied in

this thesis could be good thermoelectric options, especially if it is possible to optimize the Seebeck coefficient with the carrier concentration. The changes in the electrical resistivity reported experimentally, should be another stimulus to further study the thermoelectric possibilities of these materials. We also believe that the increase in the GeTe concentration will reduce the thermal conductivity. Another possibility to improve the thermoelectric performance of phase-change materials could be the induction of disorder expecting that the thermal conductivity decreases significantly while the electrical conductivity and the Seebeck coefficient remain almost unchanged with respect to their values of the ordered stable structure. We also suggest further studies with regard to the stable structure of GST326. The negative frequencies that we found in this study give us a hint about the possible stable structure. The fact that these modes are in the Γ point tells us that the symmetry of the structure is broken.

Conclusions

In this thesis, we explored the thermoelectric performance of tellurium based layered compounds as a function of pressure and composition. We have used density functional theory and Boltzmann transport equations to compute electronic, dynamic and transport properties of the materials.

We began by studying the best bulk room temperature thermoelectric material, bismuth telluride (Bi_2Te_3). This compound is the prototype tellurium-based layered compound for thermoelectric applications. We investigated the evolution of the electronic structure with the modification of the bond length by the application of pressure. We found that pressure can, indeed, tune the Seebeck coefficient and, even though we do not achieve the improvement showed in some experiments, we reproduced the overall trend of S with pressure at 300 K. On the other hand, our results support experimental evidence of the existence of an electronic topological transition around 2 GPa. We explained that this ETT is a consequence of non-linear effects on the band structure that occurs when hydrostatic pressure is applied to an intrinsic anisotropic semiconductor.

Then we studied other semiconductor layered tellurium structures with high and tunable electrical conductivity and with high possibility of disorder ($(GeTe)_x(Sb_2Te_3)_1$, with x = 1, 2 and 3). We have started with total energy calculations for different stacking sequences since, for some compositions, the arrangement of atoms in the stable crystalline structure is still a motive of debate. We found that the energy differences between stacking configurations are small, which suggest that possibly all are present in the experiments. For the specific case of x=3, we showed that the most accepted arrangement (which is the one with the lowest energy) is unstable. Therefore, we proposed another stacking sequence that shows dynamic stability. Regarding to the electronic properties, our results have revealed that some structures are semiconductors (with gaps around 0.2 eV) while others are metallic. For x=2 (GST225), we evidenced that the Dirac-cone like band structure reported by

Conclusions

Tominaga *et al.* is only present at certain conditions of strain and was never found when the crystal lengths were close to experimental values.

With respect to the thermoelectric properties of $(GeTe)_x(Sb_2Te_3)_1$ compounds, we showed that all the semiconductor structures have larger values of the Seebeck coefficient than those reported in experiments. We argue that this could be due to the possible mixture of different stacking configurations in experiments. For all the studied compounds, semiconductor or metallic, the out-of-plane thermal conductivity is smaller than the in-plane counterpart. The explanation is that, along the stacking of the atomic layers, atoms are weakly bonded and according to Carrete *et al.*, the reduction of the reciprocal space in such direction yields low values of κ due to geometrical considerations.

Even though, according to our estimations, $(GeTe)_x(Sb_2Te_3)_1$ compounds have poor thermoelectric performance (ZT around 0.2), the optimization of the Seebeck coefficient with doping could, eventually, double the current thermoelectric figure of merit (ZT close of 0.5). Moreover, the optimal thermoelectric performance is found at high temperatures (600 K or beyond), which could make them suitable for energy conversion in combustion engines (however in practice there could be chemical issues).

To summarize, we studied some fundamental relations between structure and thermoelectric properties in layered tellurium compounds by playing either with pressure or composition. We suggested that improvement in the Seebeck coefficient (and therefore in ZT) is feasible, but at present, insufficient for the studied compounds except at high temperatures (GST225).

During the time of this work, we used state-of-art techniques and methodologies for computing properties of materials that are relevant for thermoelectric applications. We realized that there are limitations that restrict a full theoretical study of the figure of merit. There is a necessity for further developments to calculate the electronic conductivity and the electronic contribution to the thermal conductivity. Also, the calculation of κ_l for systems with large number of atoms in their primitive cell, such as skutterudites or clathrates, is out of reach with current computational methods due to the high computational cost.

For further studies, we propose an extensive investigation of the evolution of electronic and thermoelectric properties of $(GeTe)_x(Sb_2Te_3)_1$ compounds under effects of pressure, either hydrostatic or constrain along the out-of-

Conclusions

plane axis. Indeed, we showed for Bi_2Te_3 how modifying the interlayer separation lead to interesting changes in the electronic topology and eventually to an improvement of the Seebeck coefficient. We also suggest theoretical and experimental studies where Ge i substituted, maybe only partially by Pb in the $(GeTe)_x(Sb_2Te_3)_1$ structures. It is well known that PbTe lacks of the distortion present in GeTe, and is a better thermoelectric material. We also recommend the change of Sb for Bi, as this increases the difference in mass between constituted elements which could lead higher thermal scattering. Finally, the disorder in $(GeTe)_x(Sb_2Te_3)_1$ could also increase thermal scattering with the inconvenience that the electrical conductivity is smaller than in the stable structure. Also, there is a limitation in temperature, since at high T the system will evolve towards more order and lose the advantages.

Appendix A

In this appendix we show figures that support results in the thesis.
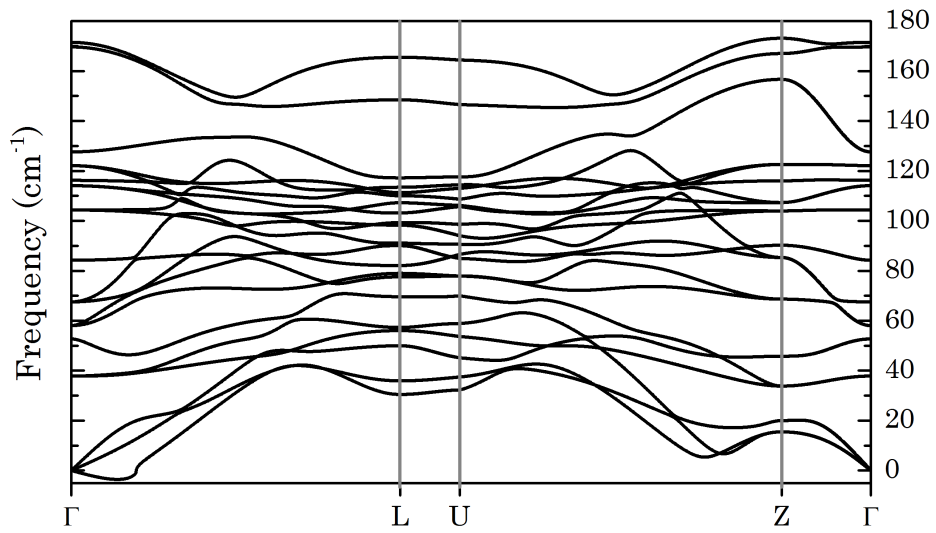
Figure A.1: Phonon bands in high symmetry paths for GST124. The small negative frequency (-3.4 cm^{-1}) comes from imperfection of the atoms relaxation.
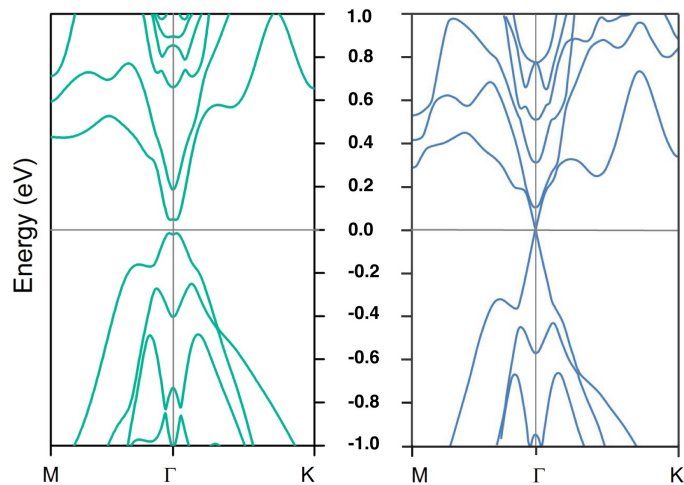
Figure A.2: Comparison of the electronic band structures obtained in this work within PBE xc (left panel) and the one reported by Tominaga *et al.* (right panel).

(a)

(b)

(c)
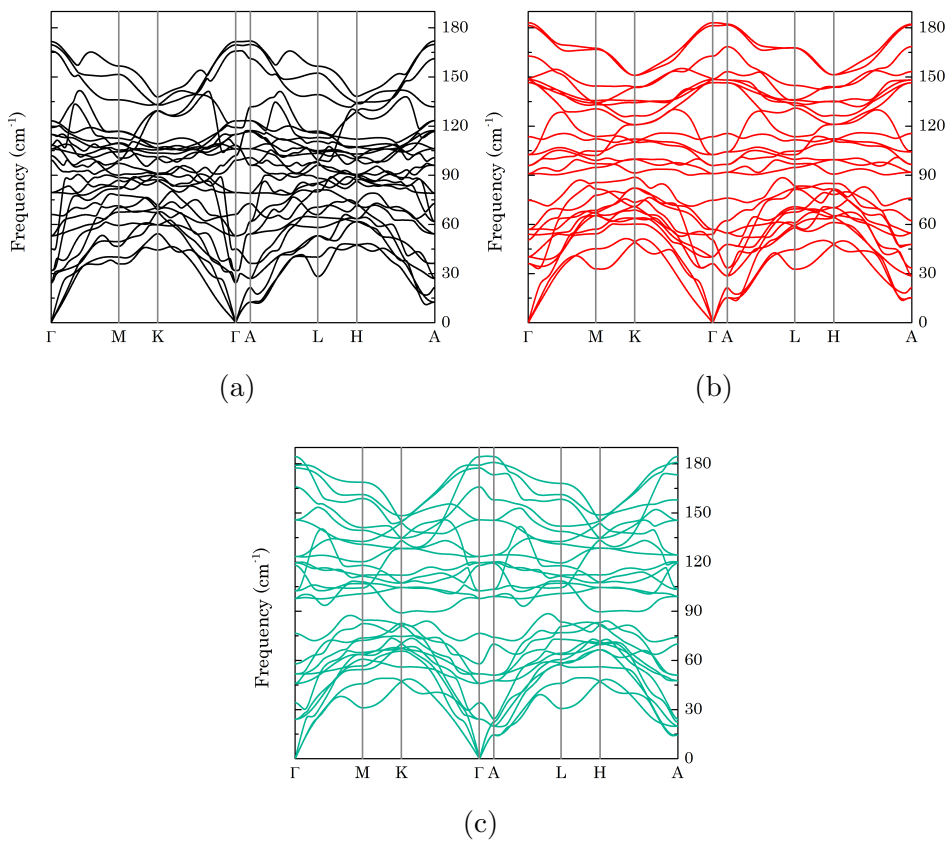
Figure A.3: Phonon band structure for GST225 in the three proposed stacking configurations. (a) Kooi and De Hosson, (b) Petrov and (c) inverted-Petrov.

Figure A.4: Heat capacity for the KH configuration of GST225. Black solid line denote the results with the inclusion of SOC, and a supercell of $2 \times 2 \times 2$. Red dashed line denote results without the inclusion of SOC and with a supercell of $5 \times 5 \times 2$.

Appendix B

List of scientific contributions

Publications in international journals

1. *Effect of hydrostatic pressure on the thermoelectric properties of Bi_2Te_3*
   Wilfredo Ibarra-Hernádez, Matthieu J. Verstraete and Jean-Yves Raty.
   PHYSICAL REVIEW B **90**, 245204 (2014)

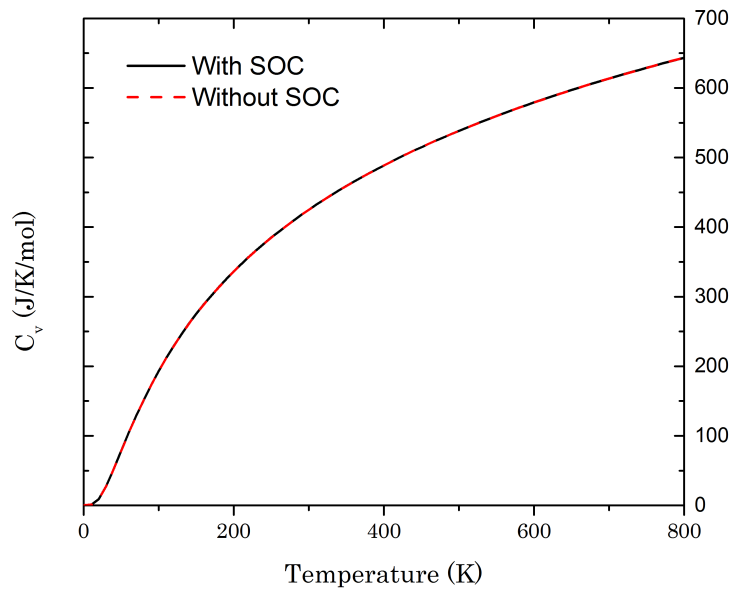2. *Effect of the change in composition on electronic, dynamic and thermoelectric properties of phase-change materials*
   Wilfredo Ibarra-Hernádez and Jean-Yves Raty.
   In progress

Oral presentations

1. *Ab Initio DFT study of electronic and thermoelectric properties of crystalline $Ge_2Sb_2Te_5$*
   Wilfredo Ibarra-Hernádez, Matthieu J. Verstraete and Jean-Yves Raty.
   PhD Day, University of Liège, Belgium, March 2015.

2. *Ab Initio DFT study of electronic and thermoelectric properties of crystalline $Ge_2Sb_2Te_5$*
   Wilfredo Ibarra-Hernádez and Jean-Yves Raty.
   March meeting APS, San Antonio, USA, March 2015

3. *Electronic properties and dynamic stability of two sequences of the crystalline $Ge_2Sb_2Te_5$*
   Wilfredo Ibarra-Hernádez, Matthieu J. Verstraete and Jean-Yves Raty.
   PhD Day, University of Liège, Belgium, April 2014.

4. *Effect of pressure on thermoelectric properties of Bi_2Te_3*
   Wilfredo Ibarra-Hernádez, Matthieu J. Verstraete and Jean-Yves Raty.
   10th ETSF Young Researcher's Meeting, Budapest, Hungary, May 2013.

5. *Effect of hydrostatic pressure on thermoelectric properties of Bi_2Te_3*
   Wilfredo Ibarra-Hernádez, Matthieu J. Verstraete and Jean-Yves Raty.
   PhD Day, University of Liège, Belgium, March 2013.

6. *An ab-initio study of GeTe based thermoelectric materials*
   Wilfredo Ibarra-Hernádez and Jean-Yves Raty.
   PhD Day, University of Liège, Belgium, March 2012.

Poster presentations

1. Thermoelectric properties of two stacking sequences of crystalline GST - 225
   Wilfredo Ibarra-Hernádez and Jean-Yves Raty.
   International Conference on Thermoelectrics, Nashville, USA, July 2014.

2. *Changes in thermoelectric properties of Bi_2Te_3 as a function of hydrostatic pressure.*
   Wilfredo Ibarra-Hernádez, Matthieu J. Verstraete and Jean-Yves Raty.
   FRONTIERS OF CONDENSED MATTER: NANOSCIENCES AND ENERGY, Les Houches, France, September 2013.

3. *An ab-initio study of thermoelectrical properties of GeTe and X2Te3 (X=Bi, Sb)*
   Wilfredo Ibarra-Hernádez and Jean-Yves Raty.
   17th ETSF Workshop on Electronic Excitations Advanced Green function methods, Coimbra, Portugal, October 2012.

Bibliography

[1] H. Julian Goldsmid. *Electronic refrigeration*. Pion Limited,, 1986.

[2] H. Julian Goldsmid. Chapter 1 introduction. In Terry M. Sbitt, editor, *Recent Trends in Thermoelectric Materials Research I*, volume 69 of *Semiconductors and Semimetals*, pages 1 – 24. Elsevier, 2001.

[3] Terry M. Tritt and M. A. Subramanian. Thermoelectric materials, phenomena, and applications: A bird's eye view. *MRS Bulletin*, 31:188–198, 3 2006.

[4] Jihui Yang and Thierry Caillat. Thermoelectric materials for space and automotive power generation. *MRS Bulletin*, 31:224–229, 3 2006.

[5] G. Jeffrey Snyder and Eric S. Toberer. Complex thermoelectric materials. *Nature Materials*, 7:105–114, February 2008.

[6] M. Wuttig and N. Yamada. Phase-change materials for rewriteable data storage. *Nature Materials*, 6:824–832, Nov 2007.

[7] G. Kresse and J. Hafner. *Ab initio* molecular dynamics for liquid metals. *Phys. Rev. B*, 47:558–561, Jan 1993.

[8] G. Kresse and J. Hafner. *Ab initio* molecular-dynamics simulation of the liquid-metal˘amorphous-semiconductor transition in germanium. *Phys. Rev. B*, 49:14251–14269, May 1994.

[9] G. Kresse and J. Furthmüller. Efficient iterative schemes for *ab initio* total-energy calculations using a plane-wave basis set. *Phys. Rev. B*, 54:11169–11186, Oct 1996.

Bibliography

[10] G. K. H. Madsen and D. J. Singh. BoltzTraP. A code for calculating band-structure dependent quantities. *Computer Physics Communications*, 175:67–71, July 2006.

[11] Wu Li, Jesús Carrete, Nebil A. Katcho, and Natalio Mingo. ShengBTE: a solver of the Boltzmann transport equation for phonons. *Comp. Phys. Commun.*, 185:17471758, 2014.

[12] bp Company. bp statical review of world energy 2014, 2014.

[13] H. Julian Goldsmid. *Introduction to Thermoelectricity*. Springer-Verlag Berlin Heidelberg, 2010.

[14] David Emin. Chapter 5 effects of charge carriers interactions on seebeck coefficients. In David Michael Rowe, editor, *Thermoelectrics Handbook Macro to Nano*, pages 5–1 – 5–7. CRC Press, 2005.

[15] Francis J. DiSalvo. Thermoelectric cooling and power generation. *Science*, 285(5428):703–706, 1999.

[16] David J. Singh. Chapter 5 theoretical and computational approaches for identifying and optimizing novel thermoelectric materials. In Terry M. Tritt, editor, *Recent Trends in Thermoelectric Materials Research II*, volume 70 of *Semiconductors and Semimetals*, pages 125 – 177. Elsevier, 2001.

[17] Jin-cheng Zheng. Recent advances on thermoelectric materials. *Frontiers of Physics in China*, 3(3):269–279, 2008.

[18] Terry M. Tritt. Thermoelectric phenomena, materials, and applications. *Annual Review of Materials Research*, 41(1):433–448, 2011.

[19] Richard M. Martin. *Electronic structure : basic theory and practical methods*. Cambridge University Press, Cambridge, New York, 2004. Description de l'diteur http://www.loc.gov/catdir/description/cam032/2003044028.html.

[20] P. Hohenberg and W. Kohn. Inhomogeneous electron gas. *Phys. Rev.*, 136:B864–B871, Nov 1964.

[21] Takao Tsuneda. *Density Functional Theory in Quantum Chemistry*. Springer Japan, 2014.

[22] W. Kohn and L. J. Sham. Self-consistent equations including exchange and correlation effects. *Phys. Rev.*, 140:A1133–A1138, Nov 1965.

Bibliography

[23] M. De La Pierre, R. Orlando, L. Maschio, K. Doll, P. Ugliengo, and R. Dovesi. Performance of six functionals (lda, pbe, pbesol, b3lyp, pbe0, and wc1lyp) in the simulation of vibrational and dielectric properties of crystalline compounds. the case of forsterite mg2sio4. *Journal of Computational Chemistry*, 32(9):1775–1784, 2011.

[24] John P. Perdew, Adrienn Ruzsinszky, Gábor I. Csonka, Oleg A. Vydrov, Gustavo E. Scuseria, Lucian A. Constantin, Xiaolan Zhou, and Kieron Burke. Restoring the density-gradient expansion for exchange in solids and surfaces. *Phys. Rev. Lett.*, 100:136406, Apr 2008.

[25] John P. Perdew, J. A. Chevary, S. H. Vosko, Koblar A. Jackson, Mark R. Pederson, D. J. Singh, and Carlos Fiolhais. Atoms, molecules, solids, and surfaces: Applications of the generalized gradient approximation for exchange and correlation. *Phys. Rev. B*, 46:6671–6687, Sep 1992.

[26] Walter A Harrison. *Solid State Theory.* Dover, New York, 1980.

[27] David J. Singh. Doping-dependent thermopower of pbte from boltzmann transport calculations. *Phys. Rev. B*, 81:195217, May 2010.

[28] Yi Wang, Xin Chen, Tian Cui, Yingli Niu, Yanchao Wang, Mei Wang, Yanming Ma, and Guangtian Zou. Enhanced thermoelectric performance of pbte within the orthorhombic *pnma* phase. *Phys. Rev. B*, 76:155127, Oct 2007.

[29] A Togo, F Oba, and I Tanaka. First-principles calculations of the ferroelastic transition between rutile-type and cacl2-type sio2 at high pressures. *Phys. rev. B*, 78:134106, Oct 2008.

[30] Xiaoli Tang and Jianjun Dong. Lattice thermal conductivity of mgo at conditions of earths interior. *Proceedings of the National Academy of Sciences*, 107(10):4539–4543, 2010.

[31] D. A. Broido, M. Malorny, G. Birner, Natalio Mingo, and D. A. Stewart. Intrinsic lattice thermal conductivity of semiconductors from first principles. *Applied Physics Letters*, 91(23):–, 2007.

[32] A. Ward and D. A. Broido. Intrinsic phonon relaxation times from first-principles studies of the thermal conductivities of si and ge. *Phys. Rev. B*, 81:085205, Feb 2010.

[33] Giorgia Fugallo, Michele Lazzeri, Lorenzo Paulatto, and Francesco Mauri. *Ab initio* variational approach for evaluating lattice thermal conductivity. *Phys. Rev. B*, 88:045430, Jul 2013.

Bibliography

[34] John Michael Ziman. *Electrons and Phonons: The Theory of Transport Phenomena in Solids*. Oxford University Press, Oxford, seven edition, 2001.

[35] Jivtesh Garg, Nicola Bonini, and Nicola Marzari. Chapter 4 first-principles determination of phonon lifetimes, mean free paths, and thermal conductivities in crystalline materials: Pure silicon and germanium. In Gyaneshwar P. Srivastava Subhash L. Shind, editor, *LENGTH-SCALE DEPENDENT PHONON INTERACTIONS*, volume 128 of *Topics in applied physics*, pages 115 – 136. Springer, 2014.

[36] N. Mingo, D. A. Stewart, D. A. Broido, L. Lindsay, and W. Li. Chapter 5 ab initio thermal transport. In Gyaneshwar P. Srivastava Subhash L. Shind, editor, *LENGTH-SCALE DEPENDENT PHONON INTERACTIONS*, volume 128 of *Topics in applied physics*, pages 137 – 173. Springer, 2014.

[37] Sangyeop Lee, Keivan Esfarjani, Tengfei Luo, Jiawei Zhou, Zhiting Tian, and Gang Chen. Resonant bonding leads to low lattice thermal conductivity. *nature communications*, 5:3525, Apr 2014.

[38] J. F. Meng, D. A. Polvani, C. D. W. Jones, F. J. DiSalvo, Y. Fei, and J. V. Badding. Pressure tuning in the chemical search for improved thermoelectric materials: ndxce3-xpt3sb4. *Chemistry of Materials*, 12(1):197–201, 2000.

[39] D. A. Polvani, J. F. Meng, N. V. Chandra Shekar, J. Sharp, and J. V. Badding. Large improvement in thermoelectric properties in pressure-tuned p-type sb1.5bi0.5te3. *Chemistry of Materials*, 13(6):2068–2071, 2001.

[40] J. V. Badding, J. F. Meng, and D. A. Polvani. Pressure tuning in the search for new and improved solid state materials. *Chemistry of Materials*, 10(10):2889–2894, 1998.

[41] P. Larson, S. D. Mahanti, and M. G. Kanatzidis. Electronic structure and transport of bi_2te_3 and $babite_3$. *Phys. Rev. B*, 61:8162–8171, Mar 2000.

[42] S. J. Youn and A. J. Freeman. First-principles electronic structure and its relation to thermoelectric properties of bi_2te_3. *Phys. Rev. B*, 63:085112, Feb 2001.

Bibliography

[43] S K Mishra, S Satpathy, and O Jepsen. Electronic structure and thermoelectric properties of bismuth telluride and bismuth selenide. *Journal of Physics: Condensed Matter*, 9(2):461, 1997.

[44] P. Larson. Effect of $p_{1/2}$ corrections in the electronic structure of bi$_2$te$_3$ compounds. *Phys. Rev. B*, 68:155121, Oct 2003.

[45] David M. Rowe. *CRC handbook of thermoelectrics*. CRC Press, 1995.

[46] Alain Polian, Michel Gauthier, Sergio Michielon Souza, Daniela Menegon Trichês, João Cardoso de Lima, and Tarciso Antonio Grandi. Two-dimensional pressure-induced electronic topological transition in bi$_2$te$_3$. *Phys. Rev. B*, 83:113106, Mar 2011.

[47] A. Nakayama, M. Einaga, Y. Tanabe, S. Nakano, F. Ishikawa, and Y. Yamada. Structural phase transition in bi2te3 under high pressure. *High Pressure Research*, 29(2):245–249, 2009.

[48] S.V. Ovsyannikov, Yu.A. Grigoreva, G.V. Vorontsov, L.N. Lukyanova, V.A. Kutasov, and V.V. Shchennikov. Thermoelectric properties of p-bi2 x sbx te3 solid solutions under pressure. *Physics of the Solid State*, 54(2):261–266, 2012.

[49] Prof. Dr. Otfried Madelung. *Semiconductors: Data Handbook*. Springer-Verlag, Berlin Heidelberg, third edition, 2004.

[50] Seizo Nakajima. The crystal structure of bi2te3xsex. *Journal of Physics and Chemistry of Solids*, 24(3):479 – 485, 1963.

[51] Min Sik Park, Jung-Hwan Song, Julia E. Medvedeva, Miyoung Kim, In Gee Kim, and Arthur J. Freeman. Electronic structure and volume effect on thermoelectric transport in p-type bi and sb tellurides. *Phys. Rev. B*, 81:155211, Apr 2010.

[52] I G Austin. The optical properties of bismuth telluride. *Proceedings of the Physical Society*, 72(4):545, 1958.

[53] R. Vilaplana, O. Gomis, F. J. Manjón, A. Segura, E. Pérez-González, P. Rodríguez-Hernández, A. Muñoz, J. González, V. Marín-Borrás, V. Muñoz Sanjosé, C. Drasar, and V. Kucek. High-pressure vibrational and optical study of bi$_2$te$_3$. *Phys. Rev. B*, 84:104112, Sep 2011.

[54] CheYu Li, A. L. Ruoff, and C. W. Spencer. Effect of pressure on the energy gap of bi2te3. *Journal of Applied Physics*, 32(9):1733–1735, 1961.

Bibliography

[55] L. G. Khvostantsev, A. I. Orlov, N. Kh. Abrikosov, T. E. Svechnikova, and S. N. Chizhevskaya. Thermoelectric properties and phase transitions in bi2te3 under hydrostatic pressure up to 9 gpa and temperature up to 300 c. *physica status solidi (a)*, 71(1):49–53, 1982.

[56] T. Thonhauser, T. J. Scheidemantel, J. O. Sofo, J. V. Badding, and G. D. Mahan. Thermoelectric properties of sb_2te_3 under pressure and uniaxial stress. *Phys. Rev. B*, 68:085201, Aug 2003.

[57] Jeongwoo Kim, Jinwoong Kim, and Seung-Hoon Jhi. Prediction of topological insulating behavior in crystalline ge-sb-te. *Phys. Rev. B*, 82:201312, Nov 2010.

[58] Feng Xiong, Albert D. Liao, David Estrada, and Eric Pop. Low-power switching of phase-change materials with carbon nanotube electrodes. *Science*, 332(6029):568–570, 2011.

[59] Feng Rao, Zhitang Song, Yan Cheng, Mengjiao Xia, Kun Ren, Liangcai Wu, Bo Liu, and Songlin Feng. Investigation of changes in band gap and density of localized states on phase transition for ge2sb2te5 and si3.5sb2te3 materials. *Acta Materialia*, 60(1):323 – 328, 2012.

[60] Schneider Matthias N., Rosenthal Tobias, Stiewe Chrsitian, and Oeckler Oliver. From phase-change materials to thermoelectrics? *Zeitschrift Fur Kristallographie*, 225:463, 2010. 11.

[61] Geunsik Lee and Seung-Hoon Jhi. *Ab initio* studies of structural and electronic properties of the crystalline $ge_2sb_2te_5$. *Phys. Rev. B*, 77:153201, Apr 2008.

[62] Vincenzo Fiorentini, Michael Methfessel, and Matthias Scheffler. Electronic and structural properties of gan by the full-potential linear muffin-tin orbitals method: The role of the d electrons. *Phys. Rev. B*, 47:13353–13362, May 1993.

[63] S.-H. Jhi and J. Ihm. Study of the electronic structure and the role of gallium 3d electrons in gallium nitride. *physica status solidi (b)*, 191(2):387–394, 1995.

[64] Toshiyuki Matsunaga and Noboru Yamada. Structural investigation of $gesb_2te_4$: a high-speed phase-change material. *Phys. Rev. B*, 69:104111, Mar 2004.

Bibliography

[65] Agaev K A and Semiletov S A. *Soviet Physics - Crystallography*, 10:86, 1965.

[66] B. J. Kooi and J. Th. M. De Hosson. Electron diffraction and high-resolution transmission electron microscopy of the high temperature crystal structures of gexsb2te3+x(x=1,2,3) phase change material. *Journal of Applied Physics*, 92(7), 2002.

[67] Imanov R M Petrov I I and Pinsker Z G. *Soviet Physics - Crystallography*, 13:339, 1968.

[68] Juarez L. F. Da Silva, Aron Walsh, and Hosun Lee. Insights into the structure of the stable and metastable $(GeTe)_m(Sb_2Te_3)_n$ compounds. *Phys. Rev. B*, 78:224111, Dec 2008.

[69] Toshiyuki Matsunaga, Noboru Yamada, and Yoshiki Kubota. Structures of stable and metastable $Ge_2Sb_2Te_5$, an intermetallic compound in GeTe–Sb_2Te_3 pseudobinary systems. *Acta Crystallographica Section B*, 60(6):685–691, Dec 2004.

[70] Jun-Woo Park, Seung Hwan Eom, Hosun Lee, Juarez L. F. Da Silva, Youn-Seon Kang, Tae-Yon Lee, and Yoon Ho Khang. Optical properties of pseudobinary gete, $ge_2sb_2te_5$, $gesb_2te_4$, $gesb_4te_7$, and sb_2te_3 from ellipsometry and density functional theory. *Phys. Rev. B*, 80:115209, Sep 2009.

[71] L.E. Shelimova, O.G. Karpinskii, P.P. Konstantinov, M.A. Kretova, E.S. Avilov, and V.S. Zemskov. Composition and properties of layered compounds in the getesb2te3system. *Inorganic Materials*, 37(4):342–348, 2001.

[72] T. Siegrist, P. Jost, H. Volker, M. Woda, P. Merkelbach, C. Schlockermann, and M. Wuttig. Disorder-induced localization in crystalline phase-change materials. *Nat Mater*, 10(3):202–208, Mar 2011.

[73] T. Thonhauser, T. J. Scheidemantel, J. O. Sofo, J. V. Badding, and G. D. Mahan. Thermoelectric properties of sb_2te_3 under pressure and uniaxial stress. *Phys. Rev. B*, 68:085201, Aug 2003.

[74] T. Thonhauser. Influence of negative pressure on thermoelectric properties of sb2te3. *Solid State Communications*, 129(4):249 – 253, 2004.

[75] T. Siegrist, P. Jost, H. Volker, M. Woda, P. Merkelbach, C. Schlockermann, and M. Wuttig. Disorder-induced localization in crystalline phase-change materials. *Nature Materials*, 10:202, 208, 2011.

Bibliography

[76] W. Zhang, A. Thiess, P. Zalden, R. Zeller, P. H. Dederichs, J-Y. Raty, M. Wuttig, S. Blgel, and R. Mazzarello. Role of vacancies in metalinsulator transitions of crystalline phase-change materials. *Nature Materials*, 11:952–956, November 2012.

[77] Zhimei Sun, Yuanchun Pan, Jian Zhou, Baisheng Sa, and Rajeev Ahuja. Origin of p-type conductivity in layered $n$gete$\cdot m$sb$_2$te$_3$ chalcogenide semiconductors. *Phys. Rev. B*, 83:113201, Mar 2011.

[78] F. Yan, T.J. Zhu, X.B. Zhao, and S.R. Dong. Microstructures and thermoelectric properties of gesbte based layered compounds. *Applied Physics A*, 88(2):425–428, 2007.

[79] P.P. Konstantinov, L.E. Shelimova, E.S. Avilov, M.A. Kretova, and V.S. Zemskov. Thermoelectric properties of ngete msb2te3layered compounds. *Inorganic Materials*, 37(7):662–668, 2001.

[80] Zhimei Sun, Jian Zhou, and Rajeev Ahuja. Structure of phase change materials for data storage. *Phys. Rev. Lett.*, 96:055507, Feb 2006.

[81] Baisheng Sa, Jian Zhou, Zhitang Song, Zhimei Sun, and Rajeev Ahuja. Pressure-induced topological insulating behavior in the ternary chalcogenide ge$_2$sb$_2$te$_5$. *Phys. Rev. B*, 84:085130, Aug 2011.

[82] Akifumi Onodera, Ichiro Sakamoto, Yasuhiko Fujii, Nobuo Moˆri, and Shunji Sugai. Structural and electrical properties of gese and gete at high pressure. *Phys. Rev. B*, 56:7935–7941, Oct 1997.

[83] J. Goldak, C. S. Barrett, D. Innes, and W. Youdelis. Structure of alpha gete. *The Journal of Chemical Physics*, 44(9), 1966.

[84] J. Y. Raty, V. Godlevsky, Ph. Ghosez, C. Bichara, J. P. Gaspard, and James R. Chelikowsky. Evidence of a reentrant peierls distortion in liquid gete. *Phys. Rev. Lett.*, 85:1950–1953, Aug 2000.

[85] Bong-Sub Lee, John R. Abelson, Stephen G. Bishop, Dae-Hwan Kang, Byung-ki Cheong, and Ki-Bum Kim. Investigation of the optical and electronic properties of ge2sb2te5 phase change material in its amorphous, cubic, and hexagonal phases. *Journal of Applied Physics*, 97(9):–, 2005.

[86] J. Tominaga, A. V. Kolobov, P. Fons, T. Nakano, and S. Murakami. Ferroelectric order control of the dirac-semimetal phase in gete-sb2te3 superlattices. *Advanced Materials Interfaces*, 1(1):n/a–n/a, 2014.

Bibliography

[87] Baisheng Sa, Jian Zhou, Zhimei Sun, Junji Tominaga, and Rajeev Ahuja. Topological insulating in GeTe/sb$_2$te$_3$ phase-change superlattice. *Phys. Rev. Lett.*, 109:096802, Aug 2012.

[88] Wilfredo Ibarra-Hernández, Matthieu J. Verstraete, and Jean-Yves Raty. Effect of hydrostatic pressure on the thermoelectric properties of **bi$_2$te$_3$**. *Phys. Rev. B*, 90:245204, Dec 2014.

[89] G C Sosso, S Caravati, C Gatti, S Assoni, and M Bernasconi. Vibrational properties of hexagonal ge 2 sb 2 te 5 from first principles. *Journal of Physics: Condensed Matter*, 21(24):245401, 2009.

[90] Jess Carrete, Natalio Mingo, and Stefano Curtarolo. Low thermal conductivity and triaxial phononic anisotropy of snse. *Applied Physics Letters*, 105(10):–, 2014.

[91] I. Friedrich, V. Weidenhof, W. Njoroge, P. Franz, and M. Wuttig. Structural transformations of ge2sb2te5 films studied by electrical resistance measurements. *Journal of Applied Physics*, 87(9), 2000.

[92] Ho-Ki Lyeo, David G. Cahill, Bong-Sub Lee, John R. Abelson, Min-Ho Kwon, Ki-Bum Kim, Stephen G. Bishop, and Byung-ki Cheong. Thermal conductivity of phase-change material ge2sb2te5. *Applied Physics Letters*, 89(15):–, 2006.

[93] N. Mingo, D.A. Stewart, D.A. Broido, L. Lindsay, and W. Li. Ab initio thermal transport. In Subhash L. Shind and Gyaneshwar P. Srivastava, editors, *Length-Scale Dependent Phonon Interactions*, volume 128 of *Topics in Applied Physics*, pages 137–173. Springer New York, 2014.

[94] Baisheng Sa, Naihua Miao, Jian Zhou, Zhimei Sun, and Rajeev Ahuja. Ab initio study of the structure and chemical bonding of stable ge3sb2te6. *Phys. Chem. Chem. Phys.*, 12:1585–1588, 2010.

[95] O.G. Karpinsky, L.E. Shelimova, M.A. Kretova, and J.-P. Fleurial. An x-ray study of the mixed-layered compounds of (gete)n (sb2te3)m homologous series. *Journal of Alloys and Compounds*, 268(12):112 – 117, 1998.

[96] Toshiyuki Matsunaga, Rie Kojima, Noboru Yamada, Kouichi Kifune, Yoshiki Kubota, and Masaki Takata. Structural investigation of ge3sb2te6, an intermetallic compound in the getesb2te3 homologous series. *Applied Physics Letters*, 90(16):–, 2007.

Bibliography

[97] Tobias Rosenthal, Matthias N. Schneider, Christian Stiewe, Markus Dblinger, and Oliver Oeckler. Real structure and thermoelectric properties of gete-rich germanium antimony tellurides. *Chemistry of Materials*, 23(19):4349–4356, 2011.

[98] Ernst-Roland Sittner, Karl Simon Siegert, Peter Jost, Carl Schlockermann, Felix Rolf Lutz Lange, and Matthias Wuttig. (gete)x(sb2te3)1x phase-change thin films as potential thermoelectric materials. *physica status solidi (a)*, 210(1):147–152, 2013.